Quinone reductase 2 *reads* H3 serotonylation to support neuronal maturation

Min Chen[1#], Celi Yang[2#], Xin Li[3-4#], Lingchun Kong[1], Benjamin H. Weekley[1], Xiaoran Wei[1], Jennifer C O'Chan[1], David A. Vinson[1], Bulent Cetin[1], Aarthi Ramakrishnan[1], Li Shen[1], Rongsheng Zeng[3], Zheng Liu[4], Juner Zhang[5], Kaylee M. Cappuccio[5], Joshua R. Sokol[5], Erdene Baljinnyam[6], Ruiqi Hu[1,6-7], Kobi Rosenblum[8], Henrik Molina[9], Qingfei Zheng[10-11], Yael David[12-15], Samuele G. Marro[1,6-7], Tom W. Muir[5], Xiang David Li[4,16*], Haitao Li[2*], and Ian Maze[1,17-18*]

[1]Nash Family Department of Neuroscience, Friedman Brain Institute, Icahn School of Medicine at Mount Sinai, New York, New York 10029, USA
Min Chen, Lingchun Kong, Benjamin H. Weekley, Xiaoran Wei, Jennifer C O'Chan, David A. Vinson, Bulent Cetin, Aarthi Ramakrishnan, Li Shen, Ruiqi Hu, Samuele G. Marro, and Ian Maze

[2]Beijing Advanced Innovation Center for Structural Biology, MOE Key Laboratory of Protein Sciences, Department of Basic Medical Sciences, School of Medicine, Tsinghua University, Beijing 100084, China
Celi Yang and Haitao Li

[3]Institute of Chemical Biology, Shenzhen Bay Laboratory, Shenzhen 518132, China
Xin Li and Rongsheng Zeng

[4]Department of Chemistry, University of Hong Kong, Hong Kong SAR, China
Xin Li, Zheng Liu, and Xiang David Li

[5]Department of Chemistry, Princeton, New Jersey 08544, USA
Juner Zhang, Kaylee M. Cappuccio, Joshua R. Sokol, and Tom W. Muir

[6]Black Family Stem Cell Institute, Icahn School of Medicine at Mount Sinai, New York, New York 10029, USA
Erdene Baljinnyam, Ruiqi Hu, and Samuele G. Marro

[7]Department of Stem Cell Biology and Regenerative Medicine, Icahn School of Medicine at Mount Sinai, New York, New York 10029, USA
Ruiqi Hu and Samuele G. Marro

[8]Sagol Department of Neurobiology, Natural Science Faculty, Center for Gene Manipulation in the Brain, University of Haifa, 3498838, Haifa, Israel
Kobi Rosenblum

[9]The Rockefeller University Proteomics Resource Center, The Rockefeller University, New York, NY 10065, USA
Henrik Molina

[10]Department of Medicinal Chemistry and Molecular Pharmacology, College of Pharmacy, Purdue University, West Lafayette, Indiana 47907, USA
Qingfei Zheng

[11]**Institute for Cancer Research, Purdue University, West Lafayette, Indiana 47907, USA**
Qingfei Zheng

[12]**Chemical Biology Program, Memorial Sloan Kettering Cancer Center, New York, New York 10065, USA**
Yael David

[13]**Tri-Institutional PhD Program in Chemical Biology, New York, New York 10065, USA**
Yael David

[14]**Department of Physiology, Biophysics and Systems Biology, Weill Cornell Medicine, New York, New York 10065, USA**
Yael David

[15]**Department of Pharmacology, Weill Cornell Medicine, New York, New York 10065, USA**
Yael David

[16]**State Key Laboratory of Synthetic Chemistry, University of Hong Kong, Hong Kong SAR, China**
Xiang David Li

[17]**Department of Pharmacological Sciences, Icahn School of Medicine at Mount Sinai, New York, New York 10029, USA**
Ian Maze

[18]**Howard Hughes Medical Institute, Icahn School of Medicine at Mount Sinai, New York, New York 10029, USA**
Ian Maze

[#]**Denotes equal contributions**

***Corresponding authors**
Ian Maze
Email: ian.maze@mssm.edu

Haitao Li
Email: lht@tsinghua.edu.cn

Xiang D. Li
Email: xiangli@hku.hk

ABSTRACT

Histone H3 Gln5 serotonylation (H3Q5ser) is a recently described posttranslational modification[1] that plays important roles in guiding transcriptional permissiveness in brain and peripheral systems[2-5]. H3Q5ser has been implicated in diverse physiological and pathological processes ranging from neural differentiation[1] to sensory processing[6], circadian rhythmicity[7], stress responsivity[8], placental gene regulation[9], and tumorigenesis[10-19]. Since H3Q5ser can occur in combination with H3 Lys4 trimethylation (H3K4me3), most mechanistic studies to date have focused on H3Q5ser's roles in modulating H3K4me3 *reader* interactions, where it has been shown to potentiate TAF3/TFIID binding to H3K4me3[1,20,21] and inhibit the recruitment of K4me3 demethylases[21]; however, whether H3 serotonylation functions as an autonomous chromatin signaling mark through dedicated *reader* proteins has remained unknown. Here, using a combination of proteomic-, structural-, molecular-, epigenomic-, and cellular-based approaches, we demonstrate that the Quinone reductase 2 (QR2) enzyme *reads* H3Q5ser independently of H3K4me3. CRISPR-Cas9-mediated disruption of H3 serotonylation or QR2's binding to the mark in human induced pluripotent stem cell-derived neurons impairs the establishment of neuronal transcriptional programs, alters synaptic connectivity, and disrupts electrophysiological maturation. These findings thus uncover an H3 serotonylation-dependent chromatin signaling axis that is essential for human neurodevelopment.

INTRODUCTION

Biogenic amines, such as serotonin (5-hydroxytryptamine or 5-HT), are a large class of evolutionarily ancient signaling molecules that contain one or more amino groups. These metabolites are found in diverse tissues in animals and can elicit biological effects locally at the site of production or remotely following transmission through the circulating blood system[2,22]. 5-

119 HT plays critical and broad roles in normal animal physiology, including embryonic development,
120 inflammation, cardiovascular, and gastrointestinal regulation, as well as the stimulation of a broad
121 spectrum of behaviors[23-26]. By extension, aberrant levels of 5-HT, and/or disruption of its signaling
122 pathways, are associated with many diseases, including digestive, cardiac, respiratory, and
123 neuronal disorders[24,26,27]. In brain, 5-HT regulates neural activity via vesicular release from
124 extended axonal projections originating in the dorsal raphe nucleus (DRN), where it acts on
125 multiple G protein-coupled receptor families to regulate behavioral plasticity[23-26].
126
127 In addition to receptor-mediated signaling, 5-HT can be conjugated to Gln residues within certain
128 protein substrates via transamidation by the Ca^{2+}-dependent transglutaminase 2 (TG2) enzyme[28,29].
129 While initially described in the context of cytosolic substrates, we discovered that these
130 monoaminylation reactions additionally occur in the nucleus. For example, 5-HT (as well as
131 dopamine[30-32] and histamine[7]) can be covalently bound to histone H3 at Gln 5 (H3Q5) to establish
132 H3Q5 serotonylation (H3Q5ser) on nucleosomes[1,21,33]. H3Q5ser can occur independently of
133 neighboring posttranslational modifications (PTMs); however, this PTM often co-occurs with H3
134 Lys4 (K4) trimethylation (me3), establishing the dual H3K4me3Q5ser mark at transcriptional start
135 sites (TSSs). The presence of H3K4me3Q5ser serves to potentiate transcription via: 1) increased
136 binding of TAF3, a TFIID subunit, which aids in RNA Pol II-mediated transcription[1,20,21]; and 2)
137 inhibition of H3K4 demethylases (KDM5 family and LSD1)[21]. Moreover, H3Q5ser has been
138 shown to engage WDR5, a member of MLL and SETD1 H3K4 methyltransferase complexes,
139 where it functions to stimulate deposition of H3K4 methylation[7,34]. H3 serotonylation levels have
140 been observed to increase following post-mitotic differentiation of human induced pluripotent
141 stem cells (hiPSCs) to 5-HTergic neurons, as well as in rat neuronal precursor cells from the 5-
142 HTergic DRN (RN46A-B14 cells)[1]. Mutating H3Q5 to alanine (H3Q5A) in RN46A-B14 cells

143 prevents H3 serotonylation, thereby reversing gene expression programs important for neural
144 differentiation. In addition to its documented actions in 5-HTergic cells, the H3K4me3Q5ser mark
145 has been detected *in vivo* in other monoaminergic and non-monoaminergic cells (both neurons and
146 glia) of the brain[1,6], with its non-monoaminergic distribution hypothesized to be regulated, at least
147 in part, by the ubiquitously expressed high-capacity, low-affinity monoamine transporter
148 OCT3/SLC22A3. In addition to its roles in neural development, H3Q5ser has been found to have
149 important functions in regulating gene expression and cellular outputs in the context of sensory
150 processing[6], stress- and depression-related phenotypes[8], placental gene regulation[9], cancer
151 progression[10-19], and circadian rhythms[7].
152
153 While H3Q5ser's functions in the context of neighboring H3K4me3 are now well documented, it
154 remains unclear whether H3Q5ser itself engages with dedicated – non-H3K4me3-associated –
155 *reader* proteins to facilitate its functions in mammalian cells. Here, employing a series of
156 proteomic-, structural-, molecular-, epigenomic-, and cellular-based assays, we now demonstrate
157 that H3Q5ser is *read* by the Quinone reductase 2 (QR2) enzyme, both *in vitro* and *in vivo*, and that
158 this interaction can occur in the context or absence of adjacent H3K4me3. Importantly,
159 implementing CRISPR-Cas9-mediated gene editing to specifically disrupt QR2-H3Q5ser
160 interactions without perturbing QR2's endogenous enzymatic functions, we show that QR2
161 binding to H3Q5ser is critical for establishing appropriate gene expression programs in human
162 neurons, which contribute to cellular maturation. These findings thus establish QR2 as a *bona fide*
163 *reader* of H3Q5ser, an interaction that plays essential roles during human neurodevelopment, and
164 one that may contribute to pathological states associated with aberrant 5-HTergic signaling in the
165 brain and beyond.
166

167 **RESULTS**

168 ***Identification of QR2 as an H3Q5ser binding protein***
169
170 To initially assess binding interactions between the H3Q5ser modification and nuclear proteins,
171 we performed H3 N-terminal peptide pulldown assays using biotinylated $H3_{1-18}$Q5ser *vs.* $H3_{1-18}$
172 unmodified, followed by Streptavidin capture and mass spectrometry, to enrich for/identify
173 proteins from HeLa nuclear extracts that display potentiated binding to the serotonyl mark.
174 Following LC-MS/MS analysis, we observed that numerous proteins displayed either modestly
175 attenuated or potentiated binding to H3Q5ser *vs.* H3 unmodified, some of which were consistent
176 with previous studies from our group and others (e.g., attenuated – KDM5A/B[21]; potentiated –
177 WDR5[7,34]). However, one protein – the Quinone reductase 2 enzyme (QR2; aka NQO2 or N-
178 ribosyldihydronicotinamide: quinone dehydrogenase 2) – was found to display a considerably
179 stronger interaction with the H3Q5ser peptide *vs.* other proteins identified in our analysis (**Fig. 1a**;
180 **Supplementary Data 1**); note that QR2's paralog, QR1, was not found to interact with the
181 H3Q5ser peptide (**Fig. 1a**, **inset**), indicating that these two evolutionarily related proteins may
182 have diverged to carry out distinct functions in cells. Next, given previously observed roles for
183 H3Q5ser in guiding gene expression programs within neural cells specifically[1,8], we developed an
184 orthogonal photoaffinity-based chemical probe approach (probe 1; derived from an $H3_{1-15}$Q5ser
185 peptide in which the Ala7 residue was replaced by a diazirine-containing photoreactive amino
186 acid; **Extended Data Fig. 1a**), to covalently capture H3Q5ser binding proteins upon UV
187 irradiation in SK-N-SH cell lysates (a neuroblastoma cell line). This probe also introduced an
188 alkyne-containing amino acid at its C-terminus to enable bioorthogonal conjugation of
189 fluorescence tags (for visualization) or biotin (for isolation) to target proteins. An unmodified
190 probe C (**Extended Data Fig. 1a**) was developed in tandem as a negative control. To further profile

191 potential binding proteins of H3Q5ser, whole-cell lysates were extracted from SK-N-SH cells and
192 were photo-crosslinked with probe 1 and probe C. Proteins captured by the probes were conjugated
193 to biotin via click chemistry, followed by affinity purification and trypsin digestion. The resulting
194 peptides were labeled with Tandem Mass Tag (TMT) reagents and pooled for subsequent
195 quantitative mass spectrometry analysis (**Fig. 1b**). Similar to our results from HeLa cells, the QR2
196 enzyme, but not QR1, exclusively stood out with a high TMT ratio (**Fig. 1c; Supplementary Data**
197 **2**; validated via immunoblotting in **Fig. 1d**). Importantly, QR2's binding to H3Q5ser was also
198 validated via peptide pulldowns from human brain nuclear extracts (**Fig. 1e**), indicating that such
199 interactions are preserved in endogenous brain tissues. We next verified that interactions between
200 QR2 and H3Q5ser are specific, demonstrating that recombinant full-length QR2, but not QR1, can
201 be robustly labeled by serotonylated probe 1, but not the unmodified probe C (**Fig. 1f**). We
202 subsequently performed biotinylated peptide pulldown assays, followed by immunoblotting, to
203 compare recombinant QR2's binding to an unmodified H3 peptide *vs.* those containing H3K4me3,
204 H3Q5ser, or H3K4me3Q5ser (all $H3_{1-18}$). These results indicated that while QR2 does not bind to
205 H3 unmodified or H3K4me3, it does bind to both H3Q5ser and H3K4me3Q5ser peptides with
206 roughly equal affinity (**Fig. 1g**, **top**). Given that additional H3 monomainylation marks have also
207 recently been identified, such as H3Q5 dopaminylation (dop)[30-32] and histaminylation (his)[7], we
208 next compared QR2 binding to H3 peptides containing H3Q5ser *vs.* H3Q5dop *vs.* H3Q5his *vs.* H3
209 unmodified, which revealed that QR2 selectively interacts with H3Q5ser (**Fig. 1g**, **bottom**). To
210 confirm the strength of QR2's selective binding to H3Q5ser (in the presence or absence of adjacent
211 H3K4me3), we performed isothermal titration calorimetry (ITC) to determine the K_D of these
212 interactions. Consistent with our *in cellulo* and *in vitro* peptide pulldown assays, we observed that
213 QR2 binds to H3Q5ser with moderately high affinity (3 μM), an interaction that was unaffected

214 by the presence of H3K4me3 (H3K4me3Q5ser; 3 μM) (**Fig. 1h**; **Extended Data Table 1**).
215 Importantly, our ITC results similarly indicated that QR2 does not bind H3 unmodified or
216 H3K4me3 peptides (**Fig. 1h**), nor does it bind H3Q5dop or H3Q5his PTMs (**Fig. 1i**; **Extended**
217 **Data Table 1**). Finally, using our orthogonal cross-linking approach, we observed that probe 1-
218 induced labeling could be effectively competed off by H3Q5ser and H3K4me3Q5ser peptides, but
219 not by H3 unmodified, H3K4me3, H3Q5dop, or H3Q5his (**Extended Data Fig. 1b-c**).
220
221 To date, QR2 has primarily been characterized as a cytosolic flavoprotein (with flavin adenine
222 dinucleotide (FAD) as its coenzyme), which functions as a putative detoxification enzyme
223 involved in the chemical reduction of reactive quinones[35]. Interestingly, QR2 has already been
224 shown to bind free 5-HT (as well as melatonin), and these interactions appear to inhibit its
225 reductase activities[36,37]. QR2 exists as a homodimer[38], and while it is expressed across sub-cellular
226 compartments, it currently has no known nuclear functions. Genetic variants of *NQO2* have been
227 identified in humans, linking dysregulation of its function to tumorigenesis and neurodegenerative
228 disorders[39]. Additionally, studies in *Nqo2* deficient mice have indicated roles for this protein in the
229 regulation of cognitive behaviors[40]. While our data indicate that QR2 binds to H3Q5ser in neural
230 cells, including in human brain tissues, whether such interactions contribute to previously observed
231 neural phenotypes remains unknown.
232
233 ***Molecular recognition of H3Q5ser by QR2***
234
235 Given that QR2 binds to H3Q5ser directly, we next wished to elucidate the manner in which this
236 molecular recognition occurs. To do so, we performed x-ray crystallography to capture the QR2-
237 H3Q5ser complex containing QR2's coenzyme FAD. These analyses demonstrated that H3Q5ser
238 inserts within a binding pocket near the homodimerization interface of QR2's chain A and chain

239 B (**Fig. 2a-b**; **Extended Data Table 2**), with rotation of the complex revealing full electron density
240 tracing of the H3Q5ser peptide from H3 Arg (R) 2 to H3 Ala (A) 7 (**Fig. 2c**; **Extended Data Fig.**
241 **2a**). Further zooming into this binding pocket, we were able to determine that Tyr (Y) 104 of
242 QR2's chain A, the indole ring of 5-HT, and FAD form π-π stacking interactions, while QR2's
243 chain A Trp (W) 105 and Phe (F) 106, along with QR2's chain B F126 and F178, collectively form
244 a hydrophobic aromatic cage to facilitate the specific binding pocket for H3Q5ser recognition (**Fig.**
245 **2d**). This binding requires the formation of critical contacts between the H3Q5ser peptide and
246 QR2, with the main chain of the H3Q5ser peptide being surrounded by multiple hydrophobic
247 interactions and several pairs of hydrogen bonds (**Extended Data Fig. 2b**). Of note, the *apo* form
248 of QR2 lacking the co-factor FAD was observed to completely lose its H3Q5ser binding activity
249 (**Extended Data Fig. 2c**), highlighting the FAD-dependent nature of H3Q5ser recognition by
250 QR2. Importantly, given that QR2 is able to bind to H3Q5ser in both the absence and presence of
251 H3K4me3, we next performed x-ray crystallography to capture the QR2-H3K4me3Q5ser
252 complex, again containing QR2's coenzyme FAD. These data demonstrated that QR2's molecular
253 recognition of the dual PTM follows a similar logic to its binding of H3Q5ser alone, with
254 H3K4me3 projecting outward from the QR2-H3Q5ser binding pocket (**Extended Data Fig. 2d-g**;
255 **Extended Data Table 2**); such findings provide further support to our previous observations that
256 the presence of H3K4me3 in the context of H3Q5ser does not impact the strength of QR2's
257 interaction with the serotonyl mark.
258
259 To provide orthogonal evidence for how QR2 interacts with the H3Q5ser peptide, we additionally
260 mapped peptide binding sites on the protein surface using our photo-crosslinking strategy[41]
261 (**Extended Data Fig. 3a-c**), which revealed major crosslinks at residues located around the Q5ser-
262 binding pocket of QR2 when mapped back to our co-crystal structure (see **Extended Data Fig. 4a**

263 and **Extended Data Table 1** for further ITC validations of QR2's molecular recognition of
264 H3Q5ser). Given that such photo-crosslinking was performed in solution, where both the protein
265 and peptide exist in a freely moving state, these binding site mapping results complement and
266 further support our crystallographic study,
267
268 Finally, to determine whether unique interactions observed in the QR2-H3Q5ser binding pocket
269 are indeed critical for QR2's molecular recognition of the mark, we focused our attention on two
270 specific residues that contribute to hydrophobic interactions when QR2 is bound to H3Q5ser, Ile
271 (I) 129 and I195. To disrupt QR2 binding to H3Q5ser, we next generated mutations in QR2
272 (I129EI195R) that were predicted – via structural modeling – to abrogate binding through the
273 introduction of a salt bridge (**Fig. 2e**). These mutations were found to have no impact on QR2's
274 endogenous enzymatic functions (*vs.* QR2 Asn (N) 162 to E); **Fig. 2f**), while fully attenuating
275 QR2's binding to H3Q5ser, both in the context of peptides (**Fig. 2g**; **Extended Data Fig. 5a,c**;
276 **Extended Data Table 1**) and mononucleosomes (**Fig. 2h; Extended Data Fig. 5d**). Given that
277 QR2 has also been reported to bind free 5-HT, we additionally performed ITC assessments to
278 explore the impact of QR2 I129EI915R mutations on its binding to free 5-HT, where we observed
279 negligible effects (**Extended Data Fig. 5b**).
280
281 ***QR2 binding to H3Q5ser contributes to cellular gene expression across species and cell-types***
282 Since our structural analyses indicated that specific hydrophobic interactions within the QR2-
283 H3Q5ser binding pocket can be perturbed to prevent QR2-H3Q5ser recognition without impacting
284 other aspects of QR2's functions, we next aimed to exploit these QR2 I129EI195R mutations in
285 cells to explore potential roles for QR2-H3Q5ser binding in the regulation of mammalian gene
286 expression. To do so, we first examined whether QR2 co-enriches with H3(K4me3)Q5ser genome-

287 wide in HeLa cells, a simple genetically modifiable tissue culture system, which has previously
288 been shown to contain the H3 serotonyl mark owing to the presence of 5-HT supplemented to the
289 media via serum[33]. We performed CUT&RUN-seq[42] using antibodies recognizing
290 H3K4me3Q5ser (validated previously[1]), QR2, and RNA Pol II, which demonstrated that QR2 co-
291 enriches with H3K4me3Q5ser genome-wide, largely at permissive genes displaying co-
292 enrichment with RNA Pol II (**Extended Data Fig. 6a-b**; **Supplementary Data 3**). Given such co-
293 enrichment, we next performed CRISPR-Cas9 editing to knockdown endogenous QR2 in HeLa
294 cells, followed by genetic complementation (under the endogenous *NQO2* promoter) with either
295 FLAG-HA-tagged QR2 wildtype or QR2 I129EI195R (**Extended Data Fig. 6c**); note that
296 complementation with the mutant form of QR2 did not have any impact on QR2's subcellular
297 localization, which is both cytoplasmic and nuclear (**Extended Data Fig. 6d**). Importantly,
298 employing $H3_{1-18}$Q5ser *vs.* $H3_{1-18}$ unmodified peptide pulldowns in HeLa nuclear extracts from
299 wildtype *vs.* mutant complemented cells, we first verified that our approach worked, demonstrating
300 that biotinylated H3Q5ser peptides efficiently pulldown wildtype, but not mutant, QR2 in
301 knockdown/complemented cells (**Extended Data Fig. 6e**). Next, we performed CUT&RUN-seq
302 for H3K4me3Q5ser, QR2, and RNA Pol II in wildtype *vs.* QR2 knockdown (no complementation)
303 *vs.* FLAG-HA-QR2 *vs.* FLAG-HA-QR2 I129EI195R complemented cells, demonstrating that
304 QR2 knockdown results in reduced co-enrichment of QR2 at H3K4me3Q5ser/RNA Pol II positive
305 loci, an effect that was fully rescued with wildtype, but not mutant, QR2 complementation
306 (**Extended Data Fig. 6f-h**; **Supplementary Data 4**). Finally, to assess whether QR2's binding to
307 H3Q5ser plays functional roles in guiding gene expression in HeLa cells, we performed RNA-seq
308 in wildtype *vs.* QR2 knockdown (no complementation) *vs.* QR2 (wildtype or mutant)
309 complementation cells, which demonstrated that the vast majority of genes displaying differential

310 expression between QR2 knockdown *vs.* wildtype cells were efficiently rescued by
311 complementation with wildtype, but not mutant, QR2 (**Extended Data Fig**; **6i-l**, **Supplementary**
312 **Data 5**).
313
314 To ensure that QR2-H3Q5ser interactions are indeed conserved across species and/or cell-types,
315 we next assessed QR2's subcellular localization in mouse brain (**Extended Data Fig. 7a**) and
316 primary neurons (mouse cerebellar granule neurons (cGNs); **Extended Data Fig. 7b**), where we
317 found that – as in HeLa cells – QR2 is distributed throughout both cytoplasmic and nuclear
318 compartments. CUT&RUN-seq for H3(K4me3)Q5ser, QR2, and RNA Pol II in cGNs further
319 revealed that QR2 largely co-localizes with H3(K4me3)Q5ser genome-wide at permissive genes
320 co-enriched by RNA Pol II (**Extended Data Fig. 7c-e**; **Supplementary Data 6**). We additionally
321 found that loci determined to be activity-dependent in response to KCl-mediated neuronal
322 depolarization displayed concordant regulation (primarily induction) of H3Q5ser, QR2, and RNA
323 Pol II enrichment (**Extended Data Fig. 7f-h**; **Supplementary Data 6**). To further assess whether
324 activity-dependent regulation of H3Q5ser-QR2 co-enrichment plays causal roles in the regulation
325 of depolarization-induced gene expression (focused here on immediate early genes (IEGs)), we
326 performed two complementary sets of analyses. (1) following transduction of cGNs with
327 lentiviruses expressing either FLAG-HA-tagged H3.3 WT or H3.3 Q5A ± KCl (note that since
328 neurons can only actively incorporate replication-independent H3.3 into postmitotic chromatin[43],
329 expression of H3.3Q5A effectively functions as a dominant negative to reduce levels of H3Q5
330 monoaminylations[1,7,8,30]), we performed chromatin immunoprecipitations (ChIPs) to enrich for
331 exogenously expressed H3.3 (wildtype or mutant), followed by re-ChIPs for either H3Q5ser or
332 RNA Pol II. In doing so, we found that while depolarization resulted in significantly increased
333 enrichment of both H3Q5ser and RNA Pol II at IEG promoters in H3.3 wildtype-expressing cells,

334 such enrichment was lost following transduction with the H3.3Q5A mutant (**Extended Data Fig.**
335 **7i-j**); these reductions in H3Q5ser and RNA Pol II in the mutant expressing cells similarly
336 corresponded to a loss of IEG expression (**Extended Data Fig. 7k**). (2) To examine whether
337 disrupting QR2 binding to H3Q5ser similarly results in a loss of KCl-mediated IEG induction, we
338 employed recently described QR2 inhibitors, yb800 and yb537, which have been shown to bind
339 QR2 within the QR2-H3Q5ser binding pocket near QR2 I129[44]. Both QR2i inhibitors were found
340 to reduce QR2 binding to H3Q5ser *in vitro* (**Extended Data Fig. 7l**), and yb800 was found to
341 significantly reduce the induction of IEGs in cGNs following depolarization (**Extended Data Fig.**
342 **7m**).
343
344 ***QR2-H3Q5ser binding in human neurons is required for maintaining gene expression***
345 ***programs that guide cellular differentiation and maturation***
346
347 Based on our findings that QR2 binding to H3Q5ser appears critical to cellular gene expression
348 programs in both HeLa cells and cGNs (including in the context of neuronal activity-dependent
349 transcription), we next wished to explore whether these interactions play causal roles in guiding
350 gene expression programs in human neurons contributing to their maturation. We had shown
351 previously that H3Q5ser is robustly induced in response to human 5-HTergic neuronal
352 differentiation, and that disrupting H3Q5ser levels in immortalized 5-HTergic rat cells results in
353 differentiation deficts[1]; however, we had yet to conclusively demonstrate whether the serotonyl
354 mark, or its *reader* interactions, causally contribute to human neurodevelopmental processes. As
355 such, and given that H3Q5ser has been found to be widely distributed across neuronal cell-types
356 in brain[1], we turned to a rapid single-step human neuronal induction system in which hiPSCs
357 expressing the transcription factor Neurogenin-2 (NGN2) are efficiently differentiated into
358 excitatory neurons[45] (**Extended Data Fig. 8a**). NGN2-induced glutamatergic neurons can be co-

359 cultured with mouse astrocytes, which allows for induction of robust neuronal
360 differentiation/maturation gene expression programs over the course of only 35 days *in vitro* (DIV)
361 (**Extended Data Fig. 8b-d**; **Supplementary Data 7**). Supplementation with 5-HT-containing
362 serum was sufficient to sustain H3 serotonylation, and this maturation trajectory was accompanied
363 by progressive co-enrichment for H3K4me3Q5ser and QR2 from DIV0 to DIV35 (**Extended Data**
364 **Fig. 8e-h**; **Supplementary Data 8-9**).
365
366 Using CRISPR-Cas9-mediated gene editing in the parental hiPSC line WTC11[46], we generated
367 multiple homozygous knock-in clones targeting the *NQO2* (QR2 I129EI195R; disrupting H3Q5ser
368 binding while preserving enzymatic functions), *TGM2* (C277A; catalytically inactivating its
369 monoaminylase functions), and *H3F3B* (Q5A and Q5N; rendering ~50% of H3 in post-mitotic
370 neurons incapable of serotonylation). These lines enabled us to directly assess roles for H3Q5ser
371 and QR2-H3Q5ser interactions during human neuronal development. Although both *H3F3A* and
372 *H3F3B* encode the H3.3 variant in humans note that while two genes – *H3F3A* and *H3F3B* –
373 encode for the H3.3 variant in humans, we selectively targeted *H3F3B* to achieve partial disruption
374 of serotonylation while preserving neuronal viability[47]. Correct targeting was confirmed by Sanger
375 sequencing (**Extended Data Fig. 9a-f**). In differentiated neurons at DIV35, H3.3 Q5A and Q5N
376 mutations resulted in significantly reduced levels of H3K4me3Q5ser relative to wildtype isogenic
377 controls, with similar attenuation observed in QR2 I129EI195R mutant neurons (**Extended Data**
378 **Fig. 9g**), suggesting that QR2 binding to H3Q5ser may help to stabilize the mark against TG2-
379 mediated erasure. Notably, the QR2 mutation did not alter overall protein expression levels in
380 differentiated neurons (**Extended Data Fig. 9h**). Peptide pulldown assays using $H3_{1-18}$Q5ser *vs.*
381 $H3_{1-18}$ unmodified peptides further demonstrated robust binding of wildtype, but not mutant, QR2
382 to the H3 serotonylation mark (**Extended Data Fig. 9i**).

383
384 Employing CUT&RUN-seq, we then profiled enrichment patterns for H3K4me3Q5ser, QR2, and
385 RNA Pol II across wildtype *vs.* mutant NGN2-induced neurons at DIV35. Similar to that observed
386 in HeLa cells and mouse cGNs, we found that QR2 displays robust co-enrichment with
387 H3K4me3Q5ser at permissive loci (co-enriched for RNA Pol II) in wildtype human neurons (**Fig.**
388 **3a**, **f**; **Supplementary Data 7**); however, this co-enrichment was severely attenuated across all
389 four mutant lines (**Fig. 3b-f**; **Supplementary Data 10**), indicating that both direct (Q5A and Q5N)
390 and indirect manipulations of the mark or its binding interactions with QR2 (QR2 I129EI195R and
391 TG2 C277A) are sufficient to disrupt H3Q5ser-QR2 co-enrichment genome-wide. In addition,
392 consistent with our findings in mouse cGNs, we observed that such perturbations are also sufficient
393 to reduce RNA Pol II localization at H3K4me3Q5ser-marked loci. Corresponding RNA-seq
394 analyses of wildtype *vs.* mutant lines revealed that both direct and indirect manipulations of the
395 mark or its binding interactions with QR2 similarly result in dysregulated patterns of gene
396 expression in maturing neurons (**Fig. 3g-j**; **Extended Data Fig. 9j-k**; **Supplementary Data 7**,
397 **11**). Indeed, differential expression analysis identified 1,193 protein-coding genes displaying
398 overlapping and consistent dysregulation across the four mutant lines (**Fig. 3k-m**; **Supplementary**
399 **Data 12**), with these overlapping genes found to be enriched for gene ontologies related to
400 neuronal maturation (e.g., axonogenesis, nervous system development, synapse organization, and
401 so on; **Fig. 3n**; **Supplementary Data 13**). Finally, since both disruption of H3Q5ser levels (H3.3
402 Q5A *vs.* WT transduction) and inhibition of QR2 binding to H3Q5ser (yb800 *vs.* vehicle) were
403 found to disrupt activity-dependent gene expression in mouse cGNs, we next assessed the potential
404 impact of perturbing H3Q5ser (Q5N) or QR2 binding to H3Q5ser (QR2 I129EI195R) in
405 differentiated human neurons in response to KCl-mediated depolarization. Consistent with our

406 studies in mouse cGNs, we observed that both manipulations were sufficient to attenuate activity-
407 dependent gene regulation in NGN-induced neurons (**Extended Data Fig. 9l**).
408
409 ***QR2-H3Q5ser interactions are required for human neuronal physiological maturation***
410
411 Given our observations that disruption of either H3Q5ser itself or its interactions with QR2
412 produces similar alterations in gene expression programs associated with human neuronal
413 maturation, we next investigated the functional and physiological consequences of these
414 perturbations in mature NGN2-induced neurons. To determine whether QR2-H3Q5ser disruption
415 affects structural maturation, we quantified neuronal morphology at DIV35 using sparse GFP
416 labeling of wildtype and mutant neurons. While the total number of neurites were found to be
417 reduced only in select lines *vs.* wildtype (H3.3Q5N, TG2 C277A; **Fig. 4a**,**c**), all four mutants
418 displayed significantly reduced neurite outgrowth (**Fig; 4b-c**), suggestive of deficits in dendritic
419 maturation. We next examined synaptic architecture to determine whether disruption of QR2-
420 H3Q5ser signaling impairs synaptic connectivity. Synapses were quantified by co-localization of
421 the presynaptic marker SYN1 and the postsynaptic marker PSD95 (**Fig. 4d**,**f**). All four mutant
422 lines exhibited a significant reduction in synaptic density, measured as double-positive puncta
423 relative to wildtype neurons. In addition, puncta size was significantly decreased across all mutants
424 (**Fig. 4e-f**), suggesting that disruption of H3Q5ser or its interaction with QR2 impairs synaptic
425 maturation. Finally, to explore the impact of these perturbations, we performed multielectrode
426 array (MEA) recordings in mature wildtype *vs.* mutant neurons. Consistent with structural and
427 synaptic deficits observed above, all four mutant lines exhibited significant reductions in firing
428 rates (**Fig. 4g**,**k**), spiking activity (**Fig. 4h**,**k**), and burst frequency (**Fig. 4i**,**k**), with comparatively
429 modest effects on burst duration (**Fig. 4j-k**). Similar impairments were observed following
430 pharmacological inhibition of QR2 in wildtype NGN2-induced neurons (**Extended Data Fig. 9m**),

431 supporting a specific role for QR2 activity in neuronal network maturation. Together, these
432 findings demonstrate that the H3Q5ser-dependent recruitment of QR2 to active chromatin is
433 required for proper neuronal gene expression, as well as structural and functional maturation of
434 human neurons.
435
436 ***QR2 binding to H3Q5ser co-recruits POU2F1 to loci important for neuronal maturation***
437
438 Although our data indicate that QR2-H3Q5ser interactions are required for neuronal gene
439 expression and maturation, the chromatin mechanisms underlying this effect remained unclear.
440 We therefore next investigated how QR2 binding to H3Q5ser promotes transcriptional activation.
441 Previous studies had shown that QR2 binds to free 5-HT, thereby inhibiting its endogenous
442 reductase activities[36,37]. Therefore, we assessed whether QR2 binding to H3Q5ser results in similar
443 disruptions to its enzymatic capacity. We performed QR2 enzymatic activity assays *in vitro* (again
444 using BNAH as an electron donor) with purified wildtype QR2 *vs.* QR2 I129EI195R following
445 pre-incubation with non-biotinylated $H3_{1-18}$Q5ser *vs.* $H3_{1-18}$ unmodified peptides. Consistent with
446 its inhibition by free 5-HT, we found that wildtype QR2 displayed significantly attenuated quinone
447 reductase activity in the presence of H3Q5ser *vs.* H3 unmodified peptides; note that such pre-
448 incubation with H3Q5ser peptides had no effect on the QR2 mutant, which cannot bind to the mark
449 (**Fig. 5a**).
450
451 Given the impact of QR2 binding to H3Q5ser on its enzymatic functions, we next hypothesized
452 that QR2 may act to recruit additional co-factors to chromatin when bound to the serotonyl mark,
453 which may, in turn, facilitate the PTM's impact on permissive gene expression. For this, we
454 revisited our established QR2 knockdown/complementation HeLa cell lines, where we next
455 performed FLAG immunoprecipitations to enrich for QR2 (complemented wildtype QR2 *vs.* QR2

456 I129EI195R) in chromatin fractions, followed by LC-MS/MS analysis to identify QR2 binding
457 partners whose interactions are dependent on the protein's ability to engage with H3Q5ser.
458 Following mass spectrometry, we identified numerous proteins that displayed significantly
459 enriched binding to wildtype QR2 in the context of chromatin (**Fig. 5b, Supplementary Data 14**),
460 with a number of these interactions found to be significantly attenuated in the QR2-H3Q5ser
461 binding-dead mutant line (**Fig. 5c, Supplementary Data 14**). Among these candidate factors was
462 POU2F1 (aka OCT1; **Fig. 5b-d**), a broadly expressed transcription factor that has recently been
463 shown to be repurposed in excitatory neurons to regulate chromatin programs important for
464 neurodevelopment[48,49]. To assess whether QR2 binds POU2F1 directly in the absence of a
465 chromatin context in which H3Q5ser is present, we purified both QR2 (wildtype and mutant, 6X-
466 His-tagged) and full length POU2F1 (HA-tagged), and performed co-immunoprecipitation assays
467 *in vitro*. Interestingly, while QR2 and POU2F1 did not appear to interact directly in the absence
468 of H3Q5ser (**Fig. 5e**), they were found to interact following spike-in of an H3Q5ser peptide (*vs.*
469 unmodified; **Fig. 5f**), suggestive of a potential allosteric mode of recognition through which QR2
470 binding to the mark may facilitate structural re-organization of the complex to allow for POU2F1
471 binding/recruitment to chromatin.
472
473 To examine this possibility in NGN2-induced neurons, we then performed CUT&RUN-seq for
474 POU2F1 in wildtype *vs.* mutant cells. In addition to demonstrating that POU2F1indeed co-enriches
475 with H3K4me3Q5ser and QR2 at TSSs of permissive, RNA Pol II-marked genes (**Extended Data**
476 **Fig. 10a**; **Supplementary Data 15**), these results identified a large number of loci that were
477 enriched for POU2F1 in wildtype neurons but displayed differential enrichment following
478 H3Q5ser depletion or in response to disrupting QR2's recognition of H3Q5ser (**Fig. 5g**; **Extended**
479 **Data Fig. 10b**; **Supplementary Data 15**). Importantly, for those loci displaying loss of POU2F1

480 enrichment in mutant neurons – sites that largely mapped to consensus POU2F1 motifs – we
481 observed that loss of chromatin accessibility at these sites (via ATAC-seq) was strongly correlated
482 (**Fig. 5h**; **Supplementary Data 16**), along with a decrease in expression of corresponding genes
483 (**Fig. 5i**). Finally, for those loci displaying concomitant reductions in POU2F1 enrichment,
484 attenuated chromatin accessibility, and decreased expression in the mutant lines, we found that
485 these genes were highly enriched for gene ontologies related to human neuronal development and
486 maturation, including pathways related to synapse organization, axonogenesis, glutamatergic
487 synaptic transmission, etc. (**Fig. 5j**; **Supplementary Data 17**). In sum, our data suggest that during
488 human neuronal differentiation and maturation, QR2 binds to H3Q5ser, leading to the recruitment
489 of important lineage specific transcription factors, such as POU2F1, which, in turn, results in
490 altered chromatin accessibility and activation of genes important for neuronal development.
491
492 **DISCUSSION**
493
494 Here, we explored the possibility that in addition to its previously described roles as a modifier of
495 H3K4me3-mediated *reader* interactions and permissive gene expression, H3Q5ser may recruit
496 additional dedicated binding proteins that facilitate its impact on transcription within mammalian
497 cells. Employing proteomic-, structural-, molecular-, epigenomic-, and cellular-based approaches,
498 we found that the quinone reductase enzyme, QR2, is a *bona fide reader* of H3Q5ser, both *in vitro*
499 and *in cellulo*, and that this interaction can occur in the absence or presence of adjacent H3K4me3.
500 Using X-ray crystallography to determine the structure of QR2 in complex with H3(K4me3)Q5ser,
501 we identified a specific pair of mutations that fully abrogate QR2's binding to H3Q5ser without
502 impacting QR2's expression, subcellular localization, or enzymatic functions. Introducing these
503 mutations to human cells, including neurons, resulted in dysregulated gene expression, including
504 those that play critical roles in neuronal maturation. Consistent with the impact of disrupting QR2-

505 H3Q5ser interactions in human neurons, we found that these manipulations promote deficits in
506 human neuronal morphology, synaptic connectivity, and electrophysiology. While QR2 has well
507 documented roles as a quinone reductase in the cytoplasm, its binding to H3Q5ser within the
508 nucleus inhibits its enzymatic activities; however, such binding then allows for the recruitment of
509 additional transcription factors, such as POU2F1, which play key roles in promoting gene
510 expression programs that are required for appropriate patterns of neuronal differentiation and
511 maturation.
512
513 While it is now clear from our studies that QR2's interactions with H3Q5ser in chromatin play
514 important roles in permissive gene transcription, particularly within neurons, it remains unclear to
515 what extent these interactions can explain QR2's previously documented roles within cells.
516 Physiologically, quinones are reactive molecules that act as oxidizing agents, easily forming
517 reactive oxygen species (ROS). While ROS have essential roles in a variety of cellular functions,
518 including innate immunity[50], they can also cause significant oxidative damage, which, at high
519 levels, can impair physiological functions through DNA damage and disrupted protein function,
520 resulting in human pathologies such as disorders of aging, cancer, and neurodegenerative
521 disease[51,52]. As mentioned above, QR2 is a flavoprotein closely related to the enzyme QR1[53], and
522 while a plethora of data is available regarding QR1 and its functions – such as its co-factor,
523 substrate, and inhibitor profile – very little remains known about QR2[35]. Evolutionary research has
524 additionally shown that both QR1 and QR2 evolved from the same common ancestor, with QR1
525 becoming selectively more efficient in utilizing NADH as a co-factor, and QR2 less efficient in
526 utilizing NADH, resulting in two similar enzymes with different cellular functions[54]. For example,
527 it remains unknown which endogenous quinones, if any, QR2 is capable of enzymatically
528 reducing, and a recent study even demonstrated that QR2 inhibition paradoxically increases

529 ROS[55]. In addition, it was also recently suggested that QR2 may have simply lost its reductase
530 functions throughout evolution in the absence of extremely high levels of ROS[56]. Also, while our
531 data demonstrated that QR2's enzymatic functions are significantly inhibited when bound to
532 H3Q5ser, such attenuation was not complete, leaving open the possibility that QR2 may still
533 function as a chromatin redox sensing protein when bound to the mark. However, given such
534 evolutionary divergence from QR1, and in light of our findings suggesting a prominent role for
535 QR2-H3Q5ser interactions in mammalian gene expression, this begs the question as to whether
536 previous interpretations of QR2's functions within cells – which have been solely anchored on the
537 premise that it functions as a quinone reductase – truly encapsulate its primary (or perhaps most
538 important) mechanistic roles in brain or beyond.
539
540 In addition, the interplay between QR2 and learning and memory (which require appropriate
541 patterns of neuronal maturation and plasticity) has been previously studied, where an inverse
542 relationship between QR2 expression and memory formation has been observed. In other words,
543 increased expression of QR2 in the hippocampus was found to be associated with impairments in
544 novel memory formation and learning, particularly in Alzheimer's Disease (AD) models and in
545 aged animals[57-59]. Reducing the expression of QR2 via genetic knockdown or using lentiviruses
546 harboring short hairpin RNAs (shRNAs)[60] all result in improved novel memory. Importantly,
547 activation of acetylcholine in the cortex or dopamine in the hippocampus repress QR2 expression,
548 resulting in enhanced memory formation during novel experiences. In addition, vital elements that
549 lie upstream of QR2 are often dysregulated with age[61]. Prolonged metabolic stress is another major
550 contributing factor to the sensitivity of novel memory formation in age-related neurodegenerative
551 disease and pathologies[62-64]. While investigating roles for QR2 in memory and learning, QR2 was
552 identified as a removable memory constraint in brain that contributes to memory decline and

553 metabolic stress[58,65]. For example, it has been shown that following acquisition of novel
554 information, activation of miR-182 in the CA1 region of the hippocampus suppresses QR2
555 expression and reduces the activation of ROS, leading to a decrease in the activity of specific
556 inhibitory interneurons[58,65,66]. In addition, within the cortex, not only does the removal of QR2
557 enhance memory consolidation, but QR2 inhibition reduces excitability in certain neuronal
558 populations[66]. Importantly, all the aforementioned studies relied on global QR2
559 knockdown/knockout/overexpression models or QR2 inhibition (using inhibitors, such as yb800,
560 which also abrogate QR2 binding to H3Q5ser), so it is impossible at this time to decipher precisely
561 which resulting phenotypes are the result of QR2's enzymatic functions *vs.* its roles in mediating
562 H3Q5ser-mediated gene expression (or a combination of both). Although our findings establish a
563 role for QR2-H3Q5ser signaling in neuronal maturation, the present study does not definitively
564 distinguish whether the observed synaptic impairments arise during early neurogenesis or during
565 later stages of synaptogenesis. Future work will be required to dissect how QR2-H3Q5ser
566 signaling contributes to these processes and whether they ultimately relate to QR2's previously
567 described roles in learning and memory.
568
569 Importantly, in humans, QR2 is predominantly expressed in the liver (where QR1 levels are low),
570 as well as in heart, brain, lung, liver, kidney, and skeletal muscle. As such, while our initial studies
571 of QR2-H3Q5ser interactions were largely focused on human neurons given H3Q5ser's previously
572 established roles in brain, it stands to reason that such interactions may also play equally important
573 roles in other organ systems and/or cell-types, especially given H3 serotonylation's broad
574 distribution across tissues. Consistent with this possibility, prior constitutive knockout studies in
575 mice have revealed important roles for QR2 in preventing myeloid hyperplasia[67,68] and other
576 malignancies[69], yet whether such effects are induced via QR2's enzymatic *vs.* chromatin functions

577 (or a combination of both) remains unclear. Indeed, future research will be necessary to fully
578 elucidate QR2's diverse functions in cells; however, we posit that its binding to H3Q5ser likely
579 plays a prominent, and perhaps even evolutionarily conserved, role across organismal systems.
580
581 Finally, while our data identified QR2 as a *bona fide reader* of H3Q5ser in mammalian cells, the
582 fact that QR2 was not observed to bind other H3 monoaminylation marks, such as H3Q5dop or
583 H3Q5his, suggests that additional dedicated *readers* may exist for these PTMs, which have yet to
584 be identified. Such exciting possibilities will indeed require further efforts; however, it is our hope
585 that the approaches presented here will serve as a valuable framework for the future identification
586 and functional characterization of additional H3 monoaminylation interacting proteins.
587
588
589
590
591
592
593
594
595
596
597
598
599
600
601
602
603
604
605
606
607
608
609
610
611
612
613

MAIN FIGURES AND LEGENDS

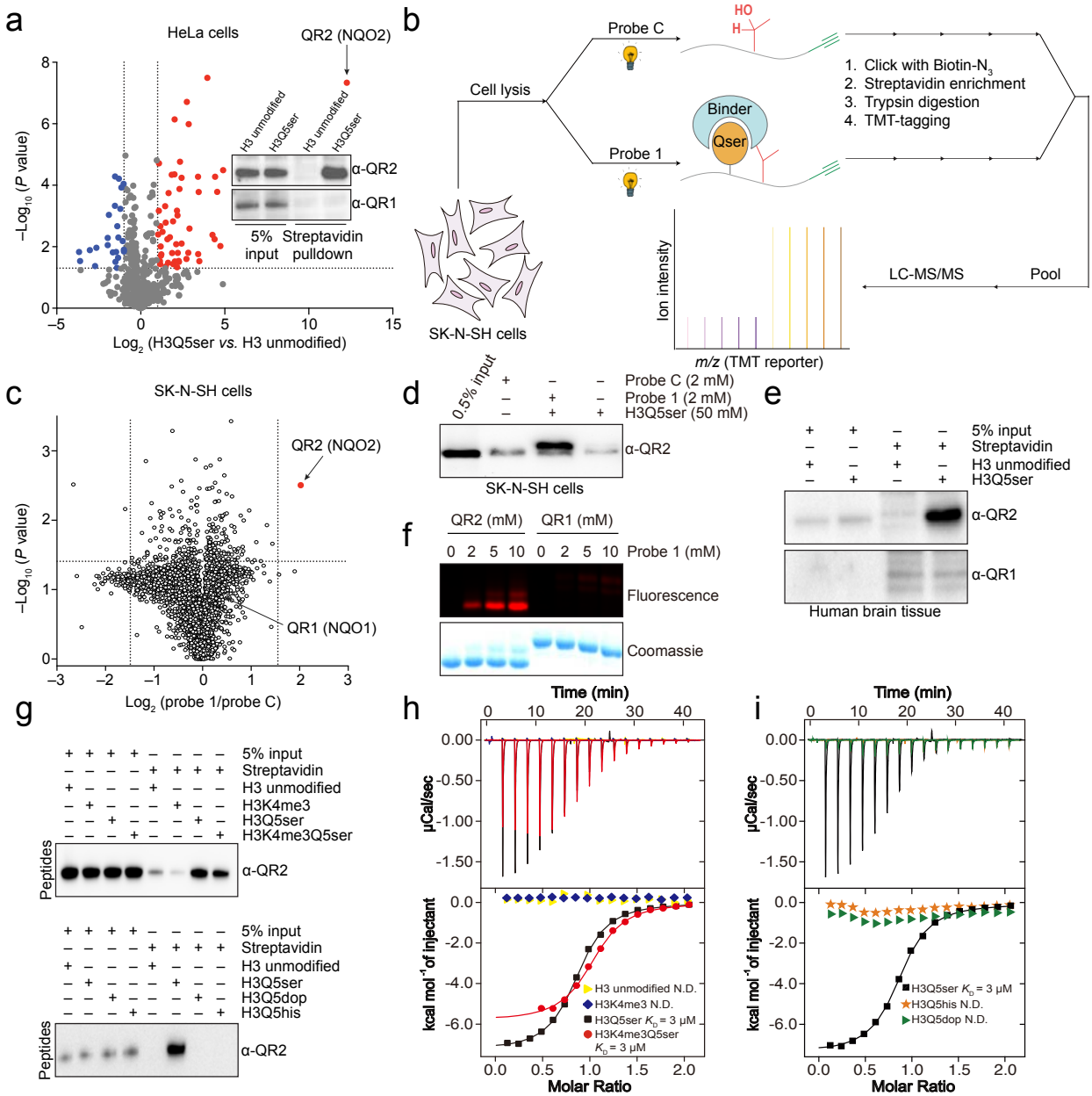

Figure 1. Identification and characterization of QR2 as an H3Q5ser binding proteins

(**a**) Volcano plots of $H3_{1\text{-}18}$Q5ser *vs.* $H3_{1\text{-}18}$ unmodified binders from HeLa nuclear extracts identified by Streptavidin capture and LC-MS/MS (n = 4; $-\log_{10} P$ value < 0.05; Log_2 fold difference > 1). Inset: immunoblotting validation of QR2, but not QR1, binding to H3Q5ser in HeLa cells. (**b**) Workflow of TMT-based chemical proteomic profiling of H3Q5ser binding proteins. (**c**) Volcano plot of proteins captured by serotonylated probe 1 *vs.* unmodified probe C from SK-N-SH cell lysates. Statistical analysis was conducted using an unpaired two-tailed Student's *t*-test. Cutoffs: significance $P < 0.05$; TMT ratio Log_2 (probe 1/probe C) > 1.5 (n = 5). (**d**) Photo-crosslinking pulldown validation of QR2 binding to H3Q5ser in SK-N-SH cell lysates.

(**e**) $H3_{1-18}$Q5ser *vs.* $H3_{1-18}$ unmodified peptide pulldowns from human brain nuclear extracts, followed by immunoblotting for QR2 or QR1. (**f**) Recombinant QR2, but not its paralog QR1, could be labeled by probe 1. (**g**) Peptide pulldowns with recombinant QR2, followed by immunoblotting for QR2. (**h-i**) Titration and fitting curves of peptides titrated into QR2. K_D values are provided. See **Extended Data Table 1** for ITC statistics. All immunoblotting experiments repeated 3X. See **Supplementary Figure 1** for uncropped blots.

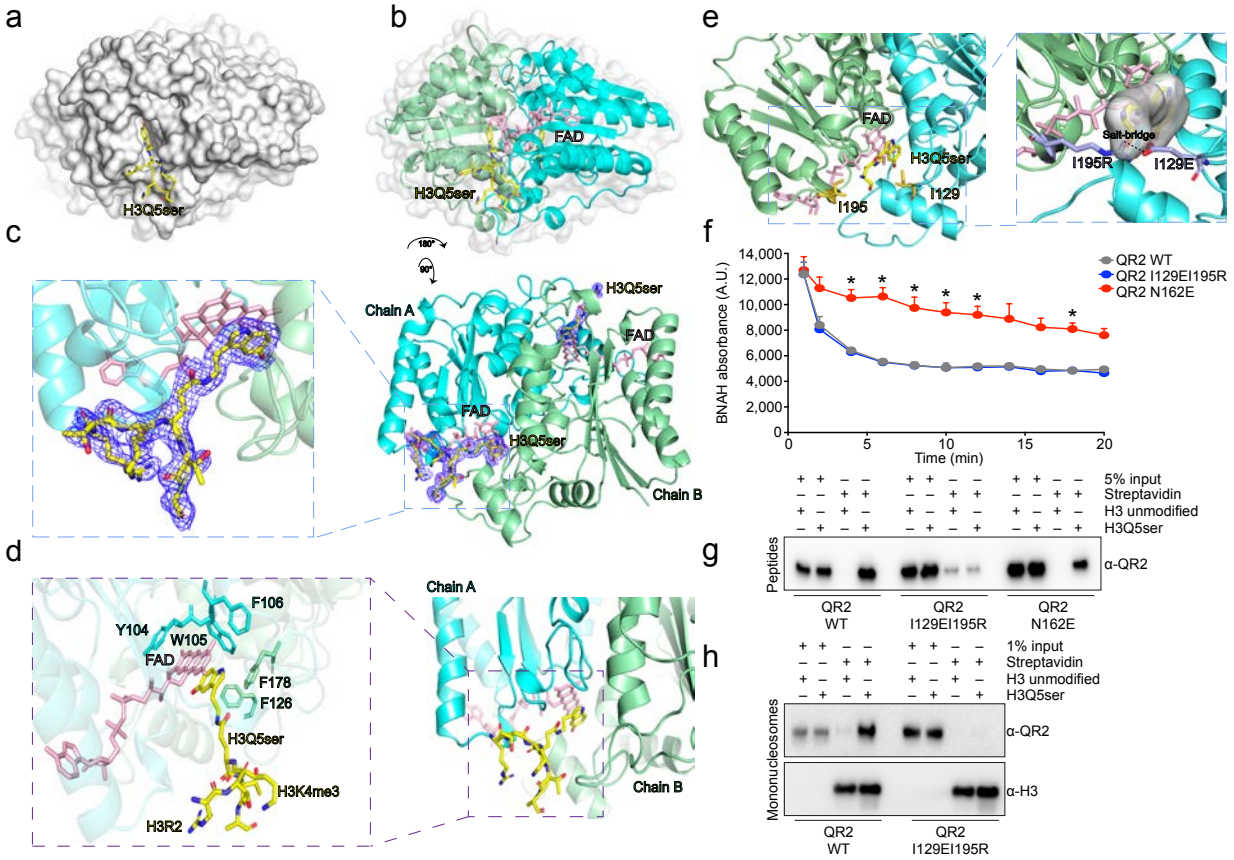

Figure 2. Molecular recognition of H3 Gln5 serotonylation by QR2

(**a**) Structure of the QR2-H3Q5ser complex. H3 residues are shown as yellow sticks, QR2 is shown as a white surface. The H3Q5ser residue inserts into the binding pocket of QR2. (**b**) Ribbon structure of the QR2-H3Q5ser complex. Ribbon shows detailed construction of QR2, H3 residues are shown as yellow sticks, coenzyme FAD is shown as pink sticks. (**c**) After rotating by a certain angle, as indicated in the diagram, the electron density of the H3Q5ser peptide is displayed, shown as a blue mesh. Chain A and Chain B in the QR2 dimer are respectively labeled. (**d**) Details of the QR2-H3Q5ser complex structure are shown. H3 residues are shown as yellow sticks, coenzyme FAD is shown as pink sticks. The key amino acid residues in Chain A (cyan) and Chain B (green) are labeled. Chain A Y104, FAD, and the serotonin ring form π-π stacking interactions, while Chain A W105, F106, Chain B F126, and F178 collectively form a hydrophobic aromatic cage, constituting the specific pocket for recognizing H3Q5ser. See **Extended Data Table 2** for x-ray

crystallography data collection and refinement statistics. (**e**) Molecular design of mutants to disrupt binding to H3Q5ser. The key amino acid residues I129 and I195 are labeled in orange. The mutants I129E and I195R are displayed as purple sticks. I129E and I195R are predicted to form a salt bridge via structural modeling, preventing the H3Q5ser peptide from inserting into the internal pocket of QR2. (**f**) BNAH enzymatic assay comparing wildtype *vs.* I129EI129R (H3Q5ser binding deficient) *vs.* N162E (catalytically deficient) QR2. n = 3. Two-way RM ANOVA [main effects: time ($F_{1.908,\ 11.45}$ = 107.2, P<0.001), QR2 mutation ($F_{2,6}$ = 21.20, P=0.0019), and QR2 mutation x time ($F_{3.816,\ 11.45}$ = 4.884, P=0.0161); post hoc: Dunnett's MC test (*p<0.05; QR2 N162E *vs.* wildtype)]. Data shown as mean ± SEM. (**g**) Peptide pulldown validations of mutant *vs.* WT QR2 abrogation of binding on H3Q5ser. (**h**) Mononucleosome pulldown validations of mutant *vs.* WT QR2 abrogation of binding on H3Q5ser. All immunoblotting experiments repeated 3X. See **Supplementary Figure 1** for uncropped blots.

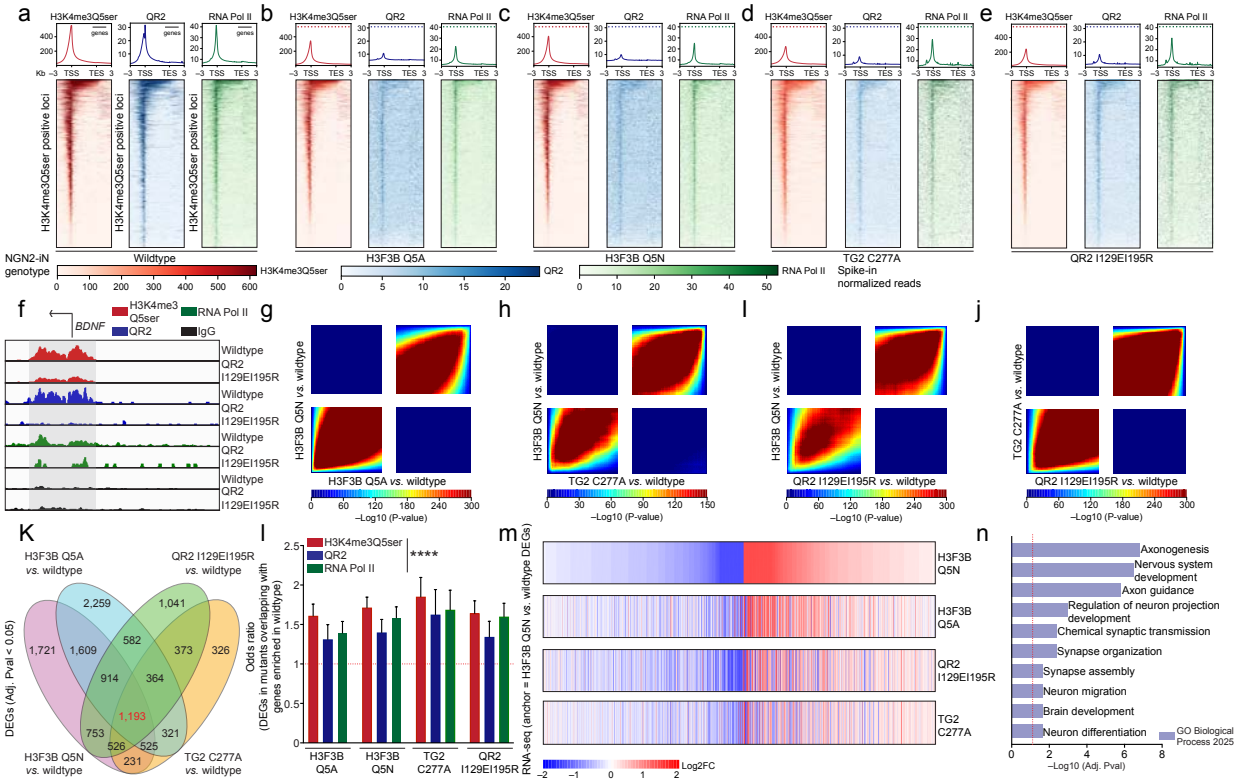

Figure 3. QR2-H3Q5ser interactions contribute to human neurodevelopmental gene expression

CUT&RUN-seq heatmaps of H3K4me3Q5ser, QR2, and RNA Pol II enrichment in (**a**) wildtype, (**b**) H3F3BQ5A, (**c**) H3F3BQ5N, (**d**) TG2 C277A, and (**e**) QR2 I129RI195R hiPSC neurons at DIV 35 (n = 3 for all; peak enrichment (spike-in normalized read coverage) anchored on wildtype signal for each line). For **b-e**, dashed lines represent wildtype signal. (**f**) IGV tracks for H3K4me3Q5ser, QR2, and RNA Pol II at the *BDNF* locus in wildtype *vs.* QR2 I129EI195R hiPSC neurons. For each antibody, scales are consistent between wildtype and QR2 mutants. RRHO

677 analyses comparing gene expression patterns (RNA-seq) between (**g**) H3F3B Q5A *vs.* wildtype
678 and H3F3B Q5N *vs.* wildtype, (**h**) H3F3B Q5N *vs.* wildtype and TG2 C277A *vs.* wildtype, (**i**)
679 H3F3B Q5N *vs.* wildtype and QR2 I129EI195R *vs.* wildtype, and (**j**) TG2 C277A *vs.* wildtype and
680 QR2 I129EI195R *vs.* wildtype demonstrating concordance across mutant lines (n = 3 for all). (**k**)
681 Venn diagram displaying the number of overlapping differentially expressed genes (DEGs)
682 between wildtype and mutant hiPSC neurons (FDR < 0.05). (**l**) Bar plot of odds ratio analysis
683 (Fisher's exact text) examining the overlap of DEGs across mutant lines *vs.* wildtype and
684 enrichment of H3K4me3Q5ser, QR2, and RNA Pol II in wildtype neurons at these same genes
685 (****P<0.0001). (**m**) Heatmaps of genes identified as being differentially expressed in H3F3B
686 Q5N *vs.* wildtype neurons (anchor; FDR < 0.05) across all mutant lines. (**n**) Go Biological Process
687 2025 enrichment for the 1,193 overlapping DEGs identified in panel **k** (FDR<0.05).
688
689
690
691
692
693
694
695
696
697
698
699
700
701
702
703
704
705
706
707
708

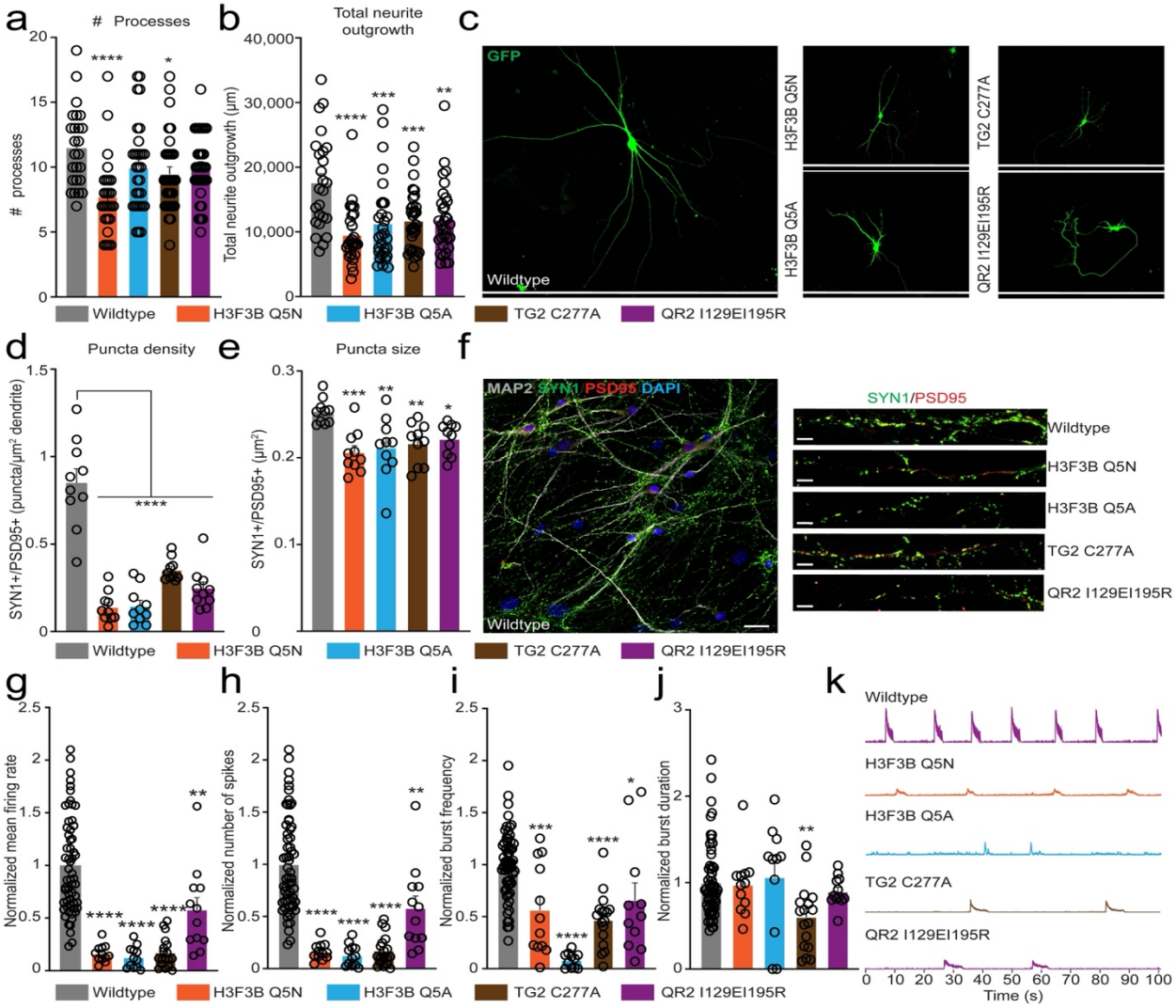

Figure 4. QR2-H3Q5ser interactions are required for human neuronal physiological maturation

(**a**) Quantification of the number of neuronal processes in wildtype *vs.* mutant hiPSC neurons [n = 25 wildtype cells, 26 H3F3B Q5N cells, 30 H3F3B Q5A cells, 31 TG2 C277A cells, and 32 QR2I129EI195R cells; one-way ANOVA, $F_{4,139} = 5.105$, P=0.0007; post hoc: Dunnett's MC test – H3F3B Q5N (****P<0.0001) and TG2 C277A (*P=0.0497)]. (**b**) Quantification of total neurite outgrowth in wildtype *vs.* mutant hiPSC neurons [n = 25 wildtype cells, 26 H3F3B Q5N cells, 30 H3F3B Q5A cells, 31 TG2 C277A cells, and 32 QR2I129EI195R cells; one-way ANOVA, $F_{4,139} = 7.222$, P<0.0001; post hoc: Dunnett's MC test – H3F3B Q5N (****P<0.0001), H3F3B Q5A (***P=0.0003), TG2 C277A (***P=0.0008), and QR2 I129EI195R (**P=0.0011). (**c**) Representative images of GFP labeled neurons from wildtype *vs.* mutant hiPSC neurons (scale = 625 µm). (**d**) Quantification of SYN1+/PSD95+ co-puncta density in wildtype *vs.* mutant hiPSC neurons [n = 10; one-way ANOVA, $F_{4,45} = 43.69$, P<0.0001; post hoc: Dunnett's MC test **** P<0.0001. (**e**) Quantification of SYN1+/PSD95+ co-puncta size in wildtype *vs.* mutant hiPSC

727 neurons [n = 10; one-way ANOVA, $F_{4,45}$ = 5.723, P=0.0008; post hoc: Dunnett's MC test – H3F3B
728 Q5N (***P=0.0003), H3F3B Q5A (**P=0.0015), TG2 C277A (**P=0.0056), and QR2
729 I129EI195R (*P=0.0208). (**f**) Representative images of co-puncta labeling from wildtype *vs.*
730 mutant hiPSC neurons (scale = left panel 25 µm; right panel 15 µm). MEA-based quantification
731 of: (**g**) normalized mean firing rate [n = 60 wildtype cells, 12 H3F3B Q5N cells, 12 H3F3B Q5A
732 cells, 18 TG2 C277A cells, and 12 QR2I129EI195R cells; one-way ANOVA, $F_{4,109}$ = 32.19,
733 P<0.0001; post hoc: Dunnett's MC test – **** P<0.0001, ** P=0.0020]; (**h**) normalized spike
734 number [n = 60 wildtype cells, 12 H3F3B Q5N cells, 12 H3F3B Q5A cells, 18 TG2 C277A cells,
735 and 12 QR2I129EI195R cells; one-way ANOVA, $F_{4,109}$ = 32.19, P<0.0001; post hoc: Dunnett's
736 MC test – **** P<0.0001, ** P=0.0020]; (**i**) normalized burst frequency [n = 60 wildtype cells,
737 12 H3F3B Q5N cells, 12 H3F3B Q5A cells, 18 TG2 C277A cells, and 12 QR2I129EI195R cells;
738 one-way ANOVA, $F_{4,106}$ = 22.28, P<0.0001; post hoc: Dunnett's MC test – **** P<0.0001, ***
739 P=0.0004, * P=0.0121]; and (**j**) normalized burst duration [n = 60 wildtype cells, 12 H3F3B Q5N
740 cells, 12 H3F3B Q5A cells, 18 TG2 C277A cells, and 12 QR2I129EI195R cells; one-way
741 ANOVA, $F_{4,107}$ = 3.323, P=0.0132; post hoc: Dunnett's MC test – ** P=0.0032]. (**k**)
742 Representative MEA traces from wildtype *vs.* mutant hiPSC neurons. Data shown as mean ± SEM.
743
744
745
746
747
748
749
750
751
752
753
754
755

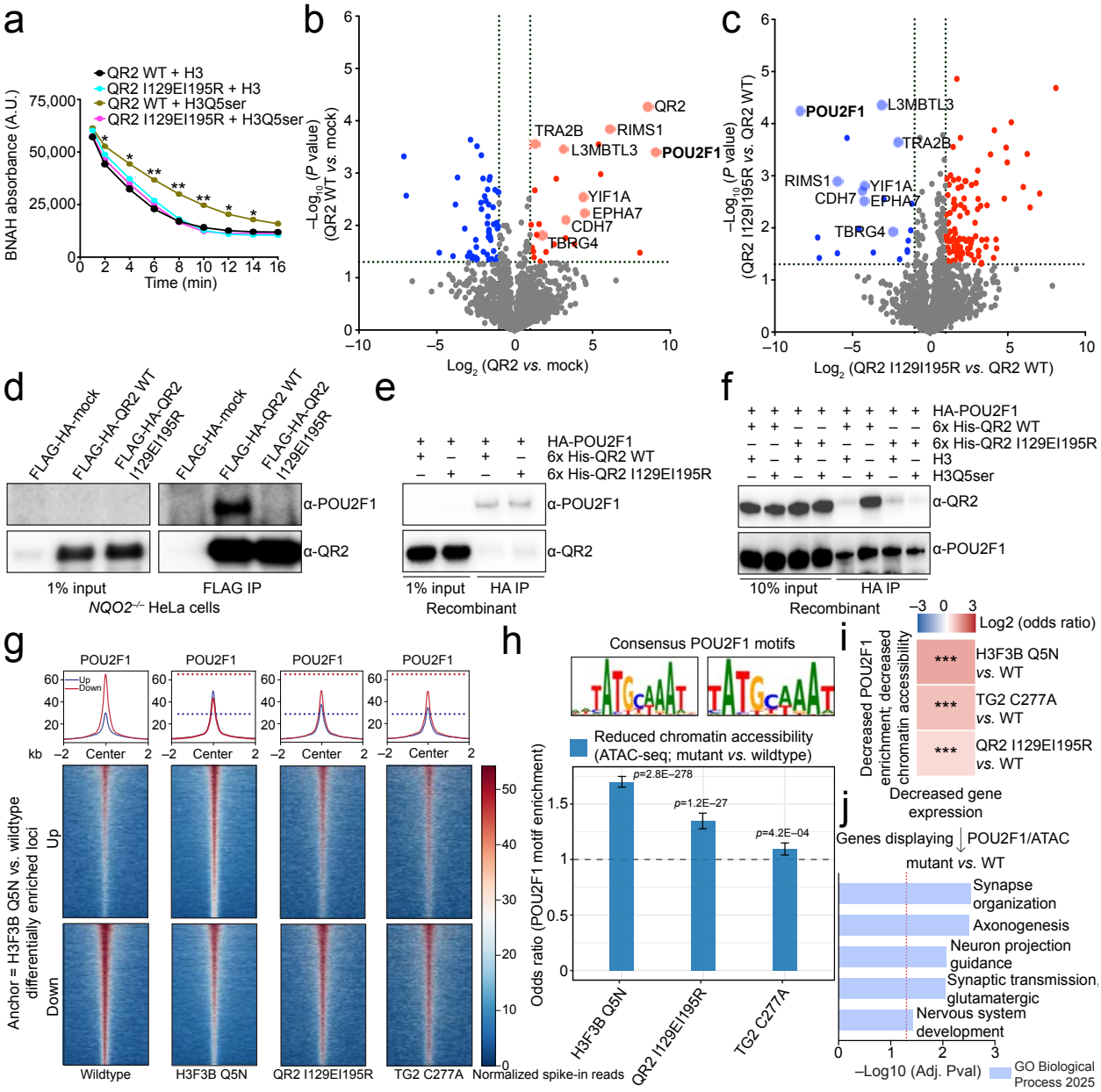

Figure 5. QR2 binding to H3Q5ser co-recruits POU2F1 to loci associated with neuronal maturation

(**a**) BNAH enzymatic assay comparing wildtype *vs.* I129EI129R QR2 following spike-in with either H3 unmodified or H3Q5ser peptides. n = 3. Two-way RM ANOVA [main effects: time ($F_{2.088,16.70}$ = 22145, P<0.0001), treatment ($F_{3,8}$ = 28.33, P=0.0001), and treatment x time ($F_{6.264,16.70}$ = 84.04, P<0.0001); post hoc: Dunnett's MC test (*P<0.05, ** P<0.01; QR2 wildtype H3Q5ser *vs.* QR2 wildtype H3 unmodified)]. Volcano plots of (**b**) FLAG-HA-tagged QR2 wildtype binders (*vs.* mock) from HeLa nuclear extracts (*NQO2* knockdown background) identified by immunoprecipitation and LC-MS/MS (n = 3; $-\log_{10} P$ value < 0.05; student's t-test difference > 1), and (**c**) FLAG-HA-tagged QR2 I129EI195R binders (*vs.* FLAG-HA-tagged QR2) from HeLa nuclear extracts (*NQO2* knockdown background) identified by immunoprecipitation and LC-

770 MS/MS (n = 3; $-\log_{10}$ P value < 0.05; student's t-test difference > 1). (**d**) Immunoblotting
771 validation of QR2-POU2F1 co-immunoprecipitation by FLAG-HA-tagged QR2 wildtype, but not
772 FLAG-HA-tagged QR2 I129EI195R, from HeLa nuclear extracts (*NQO2* knockdown
773 background). (**e**) *in vitro* QR2-POU2F1 co-immunoprecipitation experiment in the absence of H3
774 peptides. (**f**) *in vitro* QR2-POU2F1 co-immunoprecipitation experiment in the presence of
775 H3Q5ser *vs.* H3 unmodified peptides. (**g**) CUT&RUN-seq heatmaps of POU2F1 enrichment at
776 sites of differential enrichment for POU2F1 in mutant *vs.* wildtype hiPSC neurons (n = 3 for all;
777 anchor: H3F3B Q5N *vs.* wildtype). Dashed lines represent wildtype signal. (**h**) Odds ratio analysis
778 (Fisher's exact test) comparing overlap between POU2F1 consensus motifs displaying loss of
779 enrichment in mutant *vs.* wildtype hiPSC neurons and loss of chromatin accessibility (via ATAC-
780 seq) at these same loci. P values are indicated. (**i**) Odds ratio analysis (Fisher's exact test)
781 comparing overlap between genes displaying loss of POU2F1 enrichment, reduced chromatin
782 accessibility, and decreased gene expression in mutant *vs.* wildtype hiPSC neurons. *** P< 0.001.
783 (**j**) Go Biological Process 2025 enrichment for genes identified in panel **i** (FDR<0.05). Data shown
784 as mean ± SEM. All immunoblotting experiments repeated 3X. See **Supplementary Figure 1** for
785 uncropped blots.
786
787
788 **MATERIALS AND METHODS**
789
790 **General reagents**

791 *Antibodies*

792 All primary antibodies used in this study were validated, where appropriate, for use in
793 immunoblotting, immunofluorescence, chromatin immunoprecipitation (ChIP), and CUT&RUN
794 experiments. Histone H3 (Abcam, ab1791, rabbit, 1:5,000), H3Q5ser (Millipore, ABE1791,
795 rabbit, 1:500), H3K4me3Q5ser (Millipore, ABE2580, rabbit, 1:500), NQO2 (Biorbyt, orb400516,
796 rabbit, 1:500), NQO2 (Santa Cruz, mouse, sc-271665, 1:1,000), NQO2 (Abcam, ab181049, rabbit,
797 1:1,000), RNA polymerase II (Active Motif, 39097, mouse, 1:1,000), NQO1 (Santa Cruz, mouse,
798 sc-32793, 1:1,000), Rabbit IgG (Epicypher, 13-0042), POU2F1/OCT1 (Cell Signaling technology,
799 8157S, rabbit, 1:500), MAP2 (Abcam, AB5392; chicken, 1:20,000), Synapsin I/II (Synaptic
800 Systems, 106002, rabbit, 1:500), PSD95 (Synaptic Systems, 124308, guinea pig, 1:500), Alexa
801 Fluor 488-conjugated anti-chicken IgY (H+L) (Invitrogen, A-11039, 1: 1,000), Alexa Fluor 555-

802 conjugated anti-rabbit IgG (H+L) (Invitrogen, A-21428, 1:1,000), Alexa Fluor 647-conjugated
803 anti-guinea pig IgG (H+L) (Invitrogen, A-21450, 1:1000).
804
805 *Cell culture materials*
806 DMEM (Gibco, 10569044); fetal bovine serum (FBS; Gibco, A5670801); penicillin–streptomycin
807 (Gibco, 15140122); Basal Medium Eagle (Gibco, 21010046); HyClone bovine growth serum
808 (Cytiva, SH30541.03); GlutaMAX™ supplement (Gibco, 35050061); potassium chloride (KCl;
809 Invitrogen, AM9640G); tetrodotoxin citrate (TTX; Tocris, 1069); DL-2-amino-5-
810 phosphonopentanoic acid (DL-AP5; Tocris, 0105); Geltrex™ matrix (Gibco, A1413302);
811 DMEM/F-12 (Gibco, 11320033); StemFlex™ medium (Gibco, A3349401); EDTA (Invitrogen,
812 AM9260G); Dulbecco's phosphate-buffered saline (DPBS; Gibco, 14190144); Chroman 1
813 (Sigma, SML3272); doxycycline hyclate (Sigma, D3447); Opti-MEM™ I reduced-serum medium
814 (Gibco, 31985070); Lipofectamine™ Stem transfection reagent (Invitrogen, STEM00015);
815 Lipofectamine™ 3000 transfection reagent (Invitrogen, L3000008); puromycin dihydrochloride
816 (Sigma, P9620); Accutase (STEMCELL Technologies, 07920); Neurobasal™ medium (Gibco,
817 21103049); Neurobasal™-A medium (Gibco, 10888022); B-27™ supplement (Gibco, 17504044);
818 cytosine β-D-arabinofuranoside (Ara-C; Sigma, 251010); calcium chloride ($CaCl_2$; Sigma, 21115);
819 magnesium chloride ($MgCl_2$; Sigma, 63069); HEPES (Gibco, 15630080); N2 supplement (Gibco,
820 17502048); insulin (Sigma, I0516); Hank's balanced salt solution (HBSS; Gibco, 14175103);
821 papain (Worthington Biochemical Corporation, NC9597281); HyClone™ Cosmic Calf Serum
822 (Cytiva, SH30087.04); sodium pyruvate (Gibco, 11360070); MEM non-essential amino acids
823 solution (NEAA; Gibco, 11140050); 2-mercaptoethanol (Sigma, M3148); Bambanker
824 cryopreservation medium (FUJIFILM Wako, 302-14681); 0.25% trypsin–EDTA (Gibco,
825 25200056); polyethylenimine (PEI, 25 kDa; Polysciences, 23966); poly-L-ornithine

826 hydrobromide (Sigma, P4957); polybrene (Sigma, TR-1003); mTeSR™ Plus medium
827 (STEMCELL Technologies, 100-0276); CloneR™ supplement (STEMCELL Technologies,
828 05888).
829
830 **HEK 293T and HeLa cell culture**
831 HEK 293T and HeLa cell lines were obtained from the American Type Culture Collection (ATCC)
832 and grown in DMEM supplemented with 10% FBS with 100 μg ml^{-1} streptomycin and 100 U
833 ml^{-1} penicillin. Cells were maintained at 37 °C in a 5% CO_2, 95% humidified incubator.
834
835 **HeLa cell H3 peptide pulldowns and mass spectrometry**
836 *Preparation of HeLa nuclear extracts*
837 HeLa cells were cultured in DMEM to confluence, harvested, and washed with ice-cold DPBS.
838 Nuclei were isolated by hypotonic lysis using a Dounce homogenizer (20 strokes) in hypotonic
839 buffer containing: 10 mM HEPES (pH 7.5), 1.5 mM $MgCl_2$, 10 mM KCl, 0.5 mM DTT, 1 mM
840 PMSF, and a protease inhibitor cocktail. Nuclei were collected by centrifugation and lysed in high-
841 salt buffer containing: 50 mM HEPES (pH 7.5), 10% (v/v) glycerol, 500 mM KCl, 5 mM $MgCl_2$,
842 0.1% NP-40, 0.5 mM DTT, 1 mM PMSF, and protease inhibitor cocktail for 30 min at 4 °C with
843 rotation. Lysates were clarified by centrifugation at 13,000 rpm for 10 min at 4 °C, and the
844 resulting supernatant was dialyzed overnight at 4 °C against 2 L of dialysis buffer containing:
845 50 mM Tris-HCl (pH 8.0), 5% (v/v) glycerol, 150 mM KCl, 2 mM $MgCl_2$, 0.1% NP-40, and 1 mM
846 DTT. Following dialysis, extracts were transferred to fresh tubes and further clarified by
847 centrifugation at 13,000 rpm for 20 min at 4 °C. The final supernatant was used for peptide
848 pulldown assays.
849
850 *H3 peptide pulldown assay*

851 For each pulldown assay, 100 µg of biotinylated histone peptide ($H3_{1-18}$Q5ser *vs.* $H3_{1-18}$
852 unmodified) was incubated overnight at 4 °C with rotation with 100 µL of prewashed immobilized
853 streptavidin beads (Dynabeads™ M-280 Streptavidin, Invitrogen, 11206D) in DPBS containing
854 0.01% Triton X-100. For each immunoprecipitation, 40 µL of a 50% peptide–bead slurry was
855 incubated with dialyzed HeLa nuclear extract for 4 h at 4 °C with rotation. Peptide–protein
856 complexes were collected by centrifugation at 1,000 rpm for 1 min, and beads were washed four
857 times with dialysis buffer followed by four washes with detergent-free dialysis buffer (50 mM
858 Tris-HCl (pH 8.0), 150 mM KCl, 2 mM $MgCl_2$, and 1 mM DTT). For western blot analysis, beads
859 were boiled for 8 min in 30 µL of denaturing sample buffer and proteins were resolved by SDS–
860 PAGE.
861
862 *Sample preparation for mass spectrometry*
863 For *liquid chromatography tandem mass spectrometry analysis (LCMS)* , proteins bound to histone
864 peptides were reduced (10mM Dithiothreitol) and alkylated (30mM iodoacetamide) followed by
865 partial trypsinization (10ng/uL, Promega). elution . After 4h at room temperature, the supernatant
866 was transferred to new vial and re-trypsinized overnight. Digestion was halted by addition of 10%
867 trifluoroacetic acid (TFA; Thermo Scientific, 85183 and peptides were solid phase extracted prior
868 to being analyzed by direct loading reversed-phase nano–LC–MS/MS using a Fusion Lumos mass
869 spectrometer operated in high/high acquisition mode. Petptides were separated using a packed-in-
870 emitter 12cm/75um ID/3um C18 column (Nikkyo Technos Co., Ltd. Japan). Peptides were eluted
871 using a gradient delivered at 300nL/min increasing from 2% Buffer B (0.1% formic acid in 80%
872 acetonitrile) / 98% Buffer A (0.1% formic acid) to 35% Buffer B / 65% Buffer A, over 70 minutes
873 (EasyLC 1200, Thermo Scientific). All solvents were LCMS grade (Optima, Fisher Scientific).
874

875 *Mass spectrometry data processing and analysis*

876 Mass spectrometry data were searched against the UniProt human protein database using
877 MaxQuant (v. 2.0.3.0 or v. 2.4.2.0)[70] using full tryptic constraints. Oxidation of methionine
878 residues and protein N-terminal acetylation were specified as variable modifications, and
879 carbamidomethylation of cysteine residues was set as a fixed modification. False Discover Rate
880 (FDR) were set at 1% for both peptides and proteins. The experiment comprised two peptide
881 conditions ($H3_{1-18}$Q5ser *vs*. $H3_{1-18}$ unmodified), each analyzed with four biological replicates.
882 Quantitative data were processed using Perseus v. 2.0.10.0[70]. Reverse database hits and potential
883 contaminants were removed prior to analysis. Log_2-transformed intensity-based absolute
884 quantification (iBAQ) values were median-normalized on a per-sample basis. Proteins were
885 required to be quantified in at least three replicates in at least one condition to be included in
886 downstream analyses. Missing values were imputed using a normal distribution (width = 0.3;
887 downshift = 1.8). Statistical comparisons between unmodified H3 and H3Q5ser conditions were
888 performed using a permutation-based two-sided t-test with an FDR threshold of 0.05.

889

890 **Western blotting**

891 Proteins were electrophoresed on 4–12% NuPAGE Bis-Tris protein gels (Invitrogen) and
892 transferred to nitrocellulose membranes. Efficient transfer was always confirmed with direct blue
893 staining (0.1% stock aqueous solution in milliQ water) before being incubated with primary
894 antibodies overnight at 4 °C (all membranes were blocked in 5% milk or 5% BSA depending on
895 the primary antibody used). Membranes were then washed and incubated with peroxidase-labelled
896 secondary antibodies (1:2,000–1:10,000, depending on the primary antibody used). Bands were
897 detected using SuperSignal™ West Femto Maximum Sensitivity Substrate (Thermo Scientific,
898 34095) and imaged on a ChemiDoc Imaging System (Bio-Rad) under chemiluminescent detection.

899 Molecular weight markers were visualized using the colorimetric (Ponceau S) imaging setting of
900 the ChemiDoc system. Chemiluminescent images were acquired using fixed exposure settings and
901 are presented in the main figures. Composite images merging chemiluminescent signals and
902 molecular weight marker images were generated for the supplementary materials to display
903 molecular weight references.
904
905 **Chemical proteomics profiling and validations**
906 *Culturing of SK-N-SH cell*
907 SK-N-SH cells (American Type Culture Collection, HTB-11) were cultured in DMEM
908 supplemented with 10% fetal bovine serum (FBS), 100 U/mL penicillin, and 100 μg/mL
909 streptomycin. Cells were maintained in a humidified 37 °C incubator with 5% CO_2.
910
911 *Protein expression and purification*
912 Plasmids for human QR1 and QR2 proteins, containing an N-terminal hexahistidine (6×His) tag
913 in a pProEX-HTa expression vector, were generous gift from R. M. Vabulas. Point mutations in
914 QR2 were introduced using the Mut Express Universal Fast Mutagenesis Kit (Vazyme) and
915 verified by Sanger sequencing. Full-length QR1/QR2 proteins were expressed in *Escherichia coli*
916 Rosetta (DE3) cells. Protein expression was induced with 0.2 mM isopropyl β-D-1-
917 thiogalactopyranoside (IPTG) at 16 °C overnight in LB medium. Cells were lysed by sonication
918 or French press homogenization in lysis buffer (1 × PBS, pH 7.4, 20 mM imidazole, 1 mM PMSF,
919 0.5× Roche Complete EDTA-free protease inhibitor cocktail). Clarified lysates were obtained by
920 centrifugation at 25,000 × *g* for 30 min at 4 °C. The supernatant was incubated with Ni–NTA resin
921 for 2 h at 4 °C. Following target protein loading, the resin was washed extensively with 1 × PBS
922 and wash buffer (1× PBS, pH 7.4; 20 mM imidazole). For removal of bound flavin cofactors, the

923 resin was washed with denaturing buffer (1 × PBS, pH 7.4; 2 M urea; 2 M KBr) and incubated in
924 this buffer. This process was repeated until fluorescence spectroscopy (Ex 450 nm/Em 530 nm)
925 detected no FAD signal in the supernatant. The resin was then incubated overnight in 1× PBS (pH
926 7.4) containing 20 mM FAD to reload the cofactor. Proteins were eluted with elution buffer (1 ×
927 PBS, pH 7.4, 500 mM imidazole) and further purified by size-exclusion chromatography (SEC)
928 using a Superdex 75 column (Cytiva) equilibrated with gel filtration buffer (50 mM HEPES, pH
929 7.4, 150 mM NaCl). An identical purification protocol was applied to all QR2 mutant proteins.
930
931 *Preparation of SK-N-SH lysates*
932 Harvested SK-N-SH cells were resuspended in hypotonic buffer (10 mM HEPES, pH 7.5, 2 mM
933 $MgCl_2$, 0.1% Tween-20, 20% glycerol, 2 mM PMSF, and Roche Complete EDTA-free protease
934 inhibitors) and lysed on ice using a glass Dounce homogenizer (pestle B, 30 strokes). The
935 homogenate was centrifuged at 16,000 × *g* for 15 min at 4 °C. The supernatant was collected and
936 the pellet was resuspended in high-salt buffer (50 mM HEPES, pH 7.5, 420 mM NaCl, 2 mM
937 $MgCl_2$, 0.1% Tween-20, 20% glycerol, 2 mM PMSF, and Roche Complete EDTA-free protease
938 inhibitors) and homogenized with a Dounce homogenizer (pestle B, 3 × 30 strokes). The
939 suspension was centrifuged at 16,000 × *g* for 15 min at 4 °C. Supernatants from two portions were
940 pooled and clarified again at 21,000 × *g* for 15 min at 4 °C. Protein concentration was determined
941 using the Bradford assay (Bio-Rad).
942
943 *Photo-crosslinking experiments*
944 Photoaffinity probes in the absence or presence of different concentrations of competitors were
945 incubated with recombinant proteins (1 μM) or cell lysate (1.0-1.5 mg/mL) in binding buffer (150
946 mM NaCl, 50 mM HEPES, pH 7.5, 0.05% Tween 20, 20% glycerol) for 10 min at 4 °C. Then, the

947 samples were irradiated at 365 nm (Spectrolinker XL-1000) for 20 min in 96-well (recombinant
948 proteins, 75 μL each well) or 6-well plate (cell lysate, 1-2 mL each well) on ice.
949
950 *Copper(I)-catalyzed azide–alkyne cycloaddition (CuAAC)*
951 To the prepared photo-cross-linking samples, 100 μM rhodamine-N_3 for in-gel fluorescence (10
952 mM stock in DMSO) or diazo-biotin-N_3 for pulldown (5 mM stock in DMSO) was added, followed
953 by 1 mM TCEP (freshly prepared 50 mM stock in H_2O), 100 μM TBTA (10 mM stock in DMSO),
954 and finally the reactions were initiated by the addition of 1 mM $CuSO_4$ (freshly prepared 50 mM
955 stock in H_2O). The reactions were incubated for 1 h at room temperature with regular vortexing.
956 The reactions were quenched by adding 5 volumes of ice-cold acetone and placed at -20 °C
957 overnight to precipitate proteins.
958
959 *In-gel fluorescence scanning*
960 For in-gel fluorescence, acetone-precipitated protein pellets were collected by centrifugation at
961 6,000 × *g* for 5 min at 4 °C, washed twice with ice-cold methanol, and air-dried for 10 min. Pellets
962 were resuspended in 1 × LDS sample buffer (Invitrogen) containing 50 mM DTT and heated at
963 95 °C for 10 min before separation by SDS–PAGE. Fluorescently labeled proteins were visualized
964 using an Amersham ImageQuant 800 (excitation 535 nm, emission 580 nm).
965
966 *Enrichment of biotinylated proteins*
967 For enrichment of biotinylated proteins, acetone-precipitated pellets were centrifuged at 3,500 × *g*
968 for 5 min at 4 °C, washed twice with ice-cold methanol, and air-dried for 10 min. Protein pellets
969 were dissolved in PBS containing 4% SDS, 20 mM EDTA, and 10% glycerol by vortexing and
970 heating, then diluted with 1 × PBS to a final SDS concentration of 0.5%. High-capacity
971 streptavidin agarose beads (Thermo Fisher Scientific) were added, and samples were rotated for

972 1.5 h at room temperature to capture biotinylated proteins. The beads were stepwise washed by 1
973 × PBS with 0.2% SDS (5 times), 6 M urea in 1 × PBS with 0.1% SDS (5 times) and 250 mM
974 NH_4HCO_3 with 0.05% SDS (5 times). The enriched proteins were eluted by incubating the beads
975 with 25 mM $Na_2S_2O_4$, 250 mM NH_4HCO_3, and 0.05% SDS for 1 h. The eluted proteins were dried
976 with SpeedVac.
977
978 For mass spectrometry samples, before washing by 250 mM NH_4HCO_3 with 0.05% SDS, beads
979 were incubated in 10 mM DTT, 6 M urea in 1 × PBS with 0.1% SDS at 37 °C for 1 h and then
980 were added 30 mM iodoacetamide at room temperature for another 30 min in dark to reduce and
981 alkylate cysteines.
982
983 *TMT-based quantitative proteomics*
984 SpeedVac samples were redissolved in 100 μL water. Proteins were precipitated by sequential
985 addition of 400 μL methanol, 100 μL chloroform, and 300 μL water, followed by centrifugation at
986 16,000 × *g* for 2 min; the upper aqueous phase was removed, and the protein interphase was
987 washed with 600 μL pre-chilled (−20 °C) methanol and centrifuged again under the same
988 conditions. The resulting protein pellets were air-dried and reconstituted in 50 mM
989 triethylammonium bicarbonate (TEAB, pH 8.0), then digested with 0.2 μg MS-grade trypsin at
990 37 °C for 12 h with shaking, followed by an addition of 0.1 μg trypsin for 2 h to ensure complete
991 digestion. Peptide concentrations were measured using the Pierce Quantitative Fluorometric
992 Peptide Assay (Thermo Fisher Scientific), and peptides in 80 μL (~4 mg) of 50 mM TEAB were
993 labeled with TMT reagents (Thermo Fisher Scientific) dissolved in 20 μL acetonitrile for 1 h at
994 room temperature. Labeling reactions were quenched with 4 μL of 5% hydroxylamine for 15 min
995 at room temperature, after which labeled peptides were combined and dried in SpeedVac, followed

996 by desalting using Sep-Pak Vac tC18 cartridges (Waters), and dried again. Peptides were
997 fractionated on an XBridge Peptide BEH C18 column (300 Å, 3.5 μm, 2.1 mm × 250 mm) using
998 a 2–80% acetonitrile gradient in 10 mM ammonium bicarbonate (pH 10.0) over 50 min, dried, and
999 reconstituted in 0.1% formic acid for LC-MS/MS.

1000

1001 *Binding-site mapping sample preparation for QR2*

1002 For binding-site mapping, recombinant QR2 (1 μM) was incubated with probes 2 and 3 (5 μM
1003 each) in 3 mL of binding buffer (50 mM HEPES, 150 mM NaCl, 2 mM $MgCl_2$, 0.1% Tween-20,
1004 20% glycerol, pH 7.5) for 10 min at 4 °C, followed by UV irradiation at 365 nm for 20 min. After
1005 crosslinking, acid-cleavable DADPS biotin-azide (100 μM) was added together with TCEP (1
1006 mM) and TBTA (100 μM), and CuAAC was initiated by adding 1 mM $CuSO_4$ and incubating for
1007 1.5 h at room temperature before quenching with four volumes of ice-cold acetone and overnight
1008 precipitation at −20 °C. Pellets were collected by centrifugation (3,500 × *g*, 5 min, 4 °C), washed
1009 twice with ice-cold methanol, air-dried, and dissolved in 1 × PBS containing 4% SDS, 20 mM
1010 EDTA, and 10% glycerol, then diluted to 0.5% SDS and incubated with high-capacity streptavidin
1011 agarose beads (Thermo Fisher Scientific) for 1.5 h at room temperature. Beads were washed
1012 sequentially with PBS + 0.2% SDS, PBS + 0.1% SDS + 6 M urea, and resuspended in 6 M urea
1013 in 100 mM NH_4HCO_3. Then, the samples were reduced with DTT (10 mM, 1 h, room temperature),
1014 alkylated with iodoacetamide (30 mM, 30 min, dark, room temperature), followed by washed and
1015 resuspended in 1 M urea in 100 mM NH_4HCO_3 for on-bead digestion with trypsin (1 μg, 16 h,
1016 37 °C). SC-OH–labeled peptides were eluted twice with 100 μL 2% formic acid (30 min each),
1017 followed by two washes with 50% acetonitrile + 1% formic acid. All eluates and washes were
1018 pooled, dried in a SpeedVac, resuspended in 200 μL 0.5% acetic acid, and desalted using StageTips
1019 for LC-MS/MS.

1020
1021 *LC–MS/MS analysis and data analysis*

1022 The TMT samples were analyzed on an Orbitrap Ascend Tribrid mass spectrometer coupled to a
1023 Vanquish™ Neo UHPLC system (Thermo Fisher Scientific). Peptides were first loaded onto a
1024 PepMap 100 C18 trapping cartridge (5 µm, 300 µm × 5 mm) and subsequently separated on a
1025 PepMap RSLC C18 analytical column (2 µm, 75 µm × 50 cm). Data acquisition was performed
1026 using Thermo Xcalibur 4.3 software. Electrospray ionization was achieved by applying a voltage
1027 of 1,800 V through the PEEK junction at the inlet of the microcapillary column. Peptides were
1028 separated with a 4–40% acetonitrile gradient in 0.1% formic acid over 140 min at a flow rate of
1029 250 nL/min. Data were acquired in data-dependent acquisition (DDA) mode optimized for TMT-
1030 based quantitation. Full MS1 scans were collected in the Orbitrap at a resolution of 120,000 over
1031 an m/z range of 400–1,600 Th, with an automatic gain control (AGC) target of 4E5 and a maximum
1032 injection time (IT) of 50 ms. The most intense precursor ions above the defined intensity threshold
1033 were sequentially selected for MS2 fragmentation using collision-induced dissociation (CID) with
1034 a collision energy of 30%, activation time of 10 ms, and an isolation width of 0.7 m/z. MS2 spectra
1035 were acquired in the ion trap at turbo scan rate, with an AGC target of 1E4 and IT of 35 ms. For
1036 TMT reporter ion quantitation, synchronous precursor selection (SPS) MS3 scans were performed
1037 on up to 20 MS2 fragment ions using higher-energy collisional dissociation (HCD) with a
1038 normalized collision energy (NCE) of 55%. MS3 spectra were acquired in the Orbitrap at a
1039 resolution of 30,000, with an AGC target of 1E5 and IT of 200 ms. Dynamic exclusion was set to
1040 60 s to prevent repeated analysis of the same precursor ions, and charge states of 2–6 were
1041 considered for fragmentation. Proteome Discoverer (v3.0) was used to search the raw data against
1042 the UniProt *Homo sapiens* (UP000005640). Fixed modifications included cysteine
1043 carbamidomethylation and TMT-tag labeling on lysine side chains and peptide N-termini. Variable

1044 modifications included methionine oxidation, protein N-terminal acetylation, and methionine loss.
1045 Mass error tolerances were set to 20 ppm for MS1 spectra, 0.1 Da for MS2 spectra, and 20 ppm
1046 for MS3 spectra. A maximum of two missed cleavages was allowed. The false discovery rate
1047 (FDR) for both peptides and proteins was set at 0.01. Missing values were imputed using the low-
1048 abundance sampling method. Quantification was based on five biological replicates.
1049
1050 Binding-site mapping samples were analyzed on a Q Exactive PLUS mass spectrometer (Thermo
1051 Fisher Scientific) coupled to an Ultimate 3000 RSLCnano system. Peptides were first loaded onto
1052 a PepMap 100 C18 trapping cartridge (5 µm, 300 µm × 5 mm) and then separated on a PepMap
1053 RSLC C18 analytical column (2 µm, 75 µm × 25 cm). Data acquisition was performed using
1054 Thermo Xcalibur v4.3 software. Peptides were eluted with a 4–40% acetonitrile gradient in 0.1%
1055 formic acid over 90 min at a flow rate of 300 nL/min. Electrospray ionization was achieved by
1056 applying 1,800 V through a PEEK junction at the column inlet.
1057
1058 MS acquisition was conducted in data-dependent acquisition mode. Survey scans (m/z 300–1,800)
1059 were acquired in the Orbitrap at a resolution of 70,000, followed by HCD fragmentation of the top
1060 20 most intense precursors (isolation window ±1.5 m/z, resolution 17,500). Automatic gain control
1061 (AGC) targets were set to 1×10^6 ions for MS1 and 5×10^4 ions for MS2, with maximum ion
1062 injection times of 30 ms and 50 ms, respectively. The normalized collision energy for HCD was
1063 27%. Singly charged ions, ions with >8 charges, and unassigned charge states were excluded from
1064 MS2 selection.
1065
1066 Raw data were processed using Proteome Discoverer v3.0, with SC-OH (exact mass: 326.1777 Da)
1067 specified as a variable modification on any residue. The NQO2 single-protein FASTA file was
1068 used for database searching. Default parameters were applied for identification and quantification:

1069 parent MS tolerance of 20 ppm, MS/MS tolerance of 20 ppm, minimum peptide length of 6 amino
1070 acids, and up to 2 missed cleavages. Peptide quantification was based on peptide-spectrum match
1071 (PSM) counts.
1072
1073 **Vector construction and recombinant QR2 protein purification**
1074
1075 Human *NQO2* cDNA was initially cloned into the pUC19 vector. Site-directed mutagenesis was
1076 performed to generate the I129E/I195R *NQO2* mutant. All constructs were verified by Sanger
1077 sequencing. Wildtype and mutant *NQO2* inserts were subsequently subcloned into the pET28a
1078 expression vector (Addgene #69864) to generate pET28a–*NQO2* and pET28a–
1079 *NQO2*(I129E/I195R), respectively. Recombinant wildtype and mutant QR2 proteins were
1080 expressed in *Escherichia coli* BL21 cells. Protein expression was induced with 0.5 mM isopropyl
1081 β-D-1-thiogalactopyranoside (IPTG) at 16 °C overnight in LB medium. Cells were harvested and
1082 resuspended in lysis buffer containing: 500 mM NaCl, 20 mM Tris-HCl (pH 7.5), and 10% (v/v)
1083 glycerol. Cells were lysed and clarified by centrifugation, and the supernatant was applied to a
1084 HisTrap affinity column (GE Healthcare). The column was washed with five column volumes of
1085 lysis buffer, and bound proteins were eluted with buffer containing: 150 mM NaCl, 20 mM Tris-
1086 HCl (pH 7.5), and 500 mM imidazole. Purified proteins were buffer-exchanged into storage buffer
1087 (150 mM NaCl, 20 mM Tris-HCl, pH 7.5), concentrated to approximately 10 mg mL^{-1}, aliquoted,
1088 and stored at −80 °C.
1089
1090 **Protein preparation for X-ray crystallography and ITC**
1091 Human *NQO2* was subcloned into the pTrcHis2C expression vector (Thermo Fisher Scientific) to
1092 generate a construct encoding a C-terminal hexahistidine (6×His) tag. Point mutations in *NQO2*
1093 were introduced using QuikChange site-directed mutagenesis and verified by Sanger sequencing.

1094
1095 Full-length QR2 proteins were expressed in *Escherichia coli* BL21 (DE3) cells. Protein expression
1096 was induced with 0.2 mM isopropyl β-D-1-thiogalactopyranoside (IPTG) at 16 °C overnight in LB
1097 medium. Cells were harvested by centrifugation, resuspended in buffer A (150 mM NaCl, 20 mM
1098 Tris-HCl, pH 7.5, 10 mM imidazole), and lysed using an EmulsiFlex-C3 high-pressure
1099 homogenizer (Avestin). Clarified lysates were incubated with Ni–NTA affinity resin for
1100 purification.
1101
1102 To remove bound flavin cofactors, the resin-bound protein was washed with buffer B (buffer A
1103 supplemented with 2 M KBr and 2 M urea), followed by overnight incubation in buffer A
1104 containing 10 mM flavin adenine dinucleotide (FAD) to reload the cofactor. Eluted protein was
1105 further purified by anion-exchange chromatography using a Q HP column (Cytiva) and size-
1106 exclusion chromatography on a Superdex 75 column (Cytiva). All QR2 mutant proteins were
1107 purified using the same procedure. H3 peptides were prepared as previously described[7] or
1108 synthesized commercially (Beijing SciLight Biotechnology).
1109
1110 **Isothermal titration calorimetry**
1111 Isothermal titration calorimetry (ITC) experiments were performed at 25 °C using a MicroCal
1112 PEAQ-ITC instrument (Malvern Instruments). The sample cell was loaded with 200 μL of QR2
1113 protein (100 μM), and titrated with 17 sequential injections of histone peptide or serotonin (5-HT;
1114 MedChemExpress) at a concentration of 1 mM. Titration data were analyzed using Origin 7.0
1115 software and fitted to a single-site binding model. ITC statistics are provided in **Extended Data**
1116 **Table 1**.
1117

1118 **Crystallization, data collection, and structure determination**

1119 Crystallization trials were performed using the sitting-drop vapor diffusion method at 18 °C.
1120 Purified QR2 protein (10 mg mL^{-1}) was preincubated with H3Q5ser or H3K4me3Q5ser peptides
1121 at a 1:10 molar ratio in buffer containing: 100 mM NaCl and 20 mM Tris-HCl (pH 7.5). Crystals
1122 of the QR2–H3Q5ser complex were obtained under multiple reservoir conditions, including
1123 mixtures containing polyols, imidazole/MES buffers, hexylene glycol, and polyethylene glycol
1124 (PEG) 1000 and PEG 3350 at pH 6.5. Crystals of the QR2–H3K4me3Q5ser complex were
1125 obtained under similar conditions, using alternative salt components.

1126

1127 Crystals were cryoprotected and flash-frozen in liquid nitrogen prior to data collection. X-ray
1128 diffraction data were collected at the Shanghai Synchrotron Radiation Facility. Diffraction images
1129 were indexed, integrated, and scaled using HKL2000. Structures were solved by molecular
1130 replacement using MOLREP[71] from the CCP4 suite, with the QR2 structure (PDB ID: 1QR2) as
1131 the search model. Model building and refinement were carried out using COOT[72] and PHENIX[73],
1132 respectively. Data collection and refinement statistics are provided in **Extended Data Table 2**.

1133

1134 **Generation of unmodified H3 and H3Q5ser nucleosomes**

1135 *Peptide synthesis*

1136 Synthetic peptide α-thioesters used for semisynthesis were manually synthesized on Trityl-OH
1137 resin (ChemMatrix). The resin was chlorinated in dry DCM with 12 equivalents of thionyl chloride
1138 and 24 equivalents of pyridine (2 x 2 h). Excess thionyl chloride was quenched and washed with
1139 a 10% DIPEA/DCM solution. Following the chlorination, hydrazine loading was performed in
1140 DMF using 10 equivalents of Fmoc-carbazate, and 10 equivalents of DIPEA (2 x 2 h). Unreacted
1141 trityl-chloride resin was then capped with 50 equivalents of methanol in DMF (30 min) and washed

1142 extensively. Subsequent peptide synthesis was carried out through iterative cycles of Fmoc
1143 deprotection (20% piperidine in DMF with 0.1 M HOBt; 1 x 1 min and 1 x 20 min) and amino
1144 acid coupling (5 equivalents of standard Fmoc-protected amino acid, 4.9 equivalents of HATU,
1145 and 10 equivalents of DIPEA for 2 × 30 min), with extensive DMF washes between steps. Double
1146 couplings were performed when necessary to ensure complete acylation. Serotonylated glutamine
1147 residues were introduced by incorporation of Fmoc-L-glutamic acid γ-allyl ester (Chem-Impex;
1148 Coupling condition: 2 equivalents of Fmoc-L-glutamic acid γ-allyl ester, 1.9 equivalents of HATU,
1149 and 5 equivalents of DIPEA for 2 x 2 h), followed by allyl deprotection and serotonin coupling as
1150 previously described[1]. Completed peptides were cleaved and deprotected using 92.5%
1151 trifluoroacetic acid (TFA), 2.5% ethanedithiol, 2.5% triisopropylsilane, and 2.5% water,
1152 precipitated with diethyl ether, and air-dried. Peptide hydrazides were converted to C-terminal
1153 thioesters via the peptide acyl pyrazole intermediates following established protocols[74]. Briefly,
1154 1 mM crude peptide hydrazides were dissolved in 100 mM phosphate buffer (pH = 3) with 6 M
1155 guanidinium hydrochloride and 2.5 mM acetylacetone. Excess 4-mercaptophenylacetic acid was
1156 then added to the solution, and the suspensions were vigorously shaken overnight at room
1157 temperature. The reaction mixtures were centrifuged, and the supernatant containing the products
1158 were filtered. The peptide MPAA thioesters were purified on preparative reversed-phase HPLC
1159 using a 0–30% solvent B (10% water, 90% acetonitrile with 0.1% TFA) gradient over 60 min.
1160
1161 *Preparation of recombinant histones*
1162 Recombinant human histones H2A, H2B, and H4 were expressed in *E. coli* BL21(DE3) cells and
1163 purified with minor modifications to established protocols. Cultures were grown in LB medium at
1164 37 °C to an OD_{600} of ~0.6 and induced with 1 mM IPTG for 3–4 h. Cells were harvested,

1165 resuspended in lysis buffer (20 mM Tris-HCl pH 7.5, 200 mM NaCl, 1 mM EDTA, 1 mM β-
1166 mercaptoethanol, 0.1% Triton X-100), and lysed by sonication.
1167
1168 Inclusion bodies were collected by centrifugation, washed twice in lysis buffer lacking detergent,
1169 and extracted in resuspension buffer (7 M urea, 10 mM Tris-HCl, 1 mM EDTA, 100 mM NaCl,
1170 1 mM DTT). Clarified extracts were purified by cation-exchange chromatography using a HiTrap
1171 SP FF column with a linear NaCl gradient. Histone-containing fractions were pooled and further
1172 purified by preparative reversed-phase HPLC.
1173
1174 *Preparation of truncated histone H3*
1175 N-terminally His_6–SUMO–tagged human histone H3(14–135, K14C) was expressed in *E.*
1176 *coli* BL21(DE3). Cells were lysed under denaturing conditions (6 M guanidinium hydrochloride),
1177 and the tagged protein was purified by Ni–NTA affinity chromatography. Eluted protein was
1178 stepwise dialyzed to remove denaturant and refold the protein. Ulp1 protease was added to cleave
1179 the His_6–SUMO tag. Following proteolysis, solubilized truncated histone was purified by
1180 preparative reversed-phase HPLC.
1181
1182 *Semisynthesis of modified histone H3*
1183 Full-length histone H3 was generated by native chemical ligation between peptide α-thioesters
1184 corresponding to residues 1–13 and truncated H3(14–135, K14C). Ligation reactions were
1185 performed in a well-ventilated chemical hood in 200 mM sodium phosphate buffer (pH = 7.0–7.2)
1186 containing 6 M guanidinium hydrochloride, 50 mM TCEP, and 2% v/v TFET at room temperature
1187 overnight. Completion of ligation was confirmed by HPLC and ESI–MS. The ligation product was
1188 purified by preparative reversed-phase HPLC and treated with 2-bromoethylammonium bromide
1189 to convert the non-native cysteine at position 14 into a lysine analogue following established

1190 protocols[75]. Final products were purified by semi-preparative HPLC and validated by HPLC and
1191 ESI–MS.
1192
1193 *Histone octamer refolding*
1194 Histone octamers were assembled using established protocols.[1] Individual histones were dissolved
1195 in unfolding buffer (6 M guanidinium chloride, 20 mM Tris-HCl pH 7.9, 1 mM DTT), quantified
1196 by absorbance at 280 nm, and combined at a molar ratio of H3:H4:H2A:H2B = 1:1:1.1:1.1 to a
1197 final concentration of 1 mg mL^{-1}. The mixture was dialyzed stepwise into refolding buffer (2 M
1198 NaCl, 10 mM Tris-HCl pH 7.9, 1 mM EDTA, 1 mM DTT) at 4 °C. Refolded octamers were
1199 purified by size-exclusion chromatography using a Superdex S200 Increase column. Pure fractions
1200 were pooled, adjusted to 50% glycerol, and stored at −20 °C.
1201
1202 *DNA preparation*
1203 Biotinylated Widom 601 DNA containing 15-bp overhangs was prepared for mononucleosome
1204 assembly. The target fragment was amplified by PCR with Pfu DNA polymerase. A 5′-biotinylated
1205 forward primer (5'-Biotin-TACTACGCGGCCGCCCTGG-3') and an unmodified reverse primer
1206 (5'-CTGGATCTTACATGCACAGGATGTATATATCTGACACGTGC-3') were synthesized
1207 and HPLC-purified commercially (IDT). The PCR product was purified by ethanol precipitation.
1208 Briefly, sodium acetate (0.1 volumes of 3 M solution, pH 5.3) and ethanol (2.5 volumes) were
1209 added to the reaction mixture, and the DNA product was precipitated overnight at −20 °C.
1210 Precipitated DNA was collected by centrifugation and resuspended in a minimal volume of
1211 nuclease-free water. The sample was further purified using PCR purification silica columns
1212 according to the manufacturer's instructions and eluted in nuclease-free water. DNA concentration
1213 was determined by UV absorbance using a NanoDrop spectrophotometer.

1214
1215 *Nucleosome reconstitution*

1216 Nucleosomes were assembled by salt-gradient dialysis. Histone octamers were mixed with 601
1217 DNA in octamer refolding buffer (10 mM Tris-HCl, 2 M NaCl, 0.5 mM EDTA, 1 mM DTT,
1218 pH 7.8) and dialyzed stepwise at 4 °C to decreasing the salt concentrations (from 2 M NaCl to 1.4
1219 M KCl, and then to 10 mM KCl overnight via a peristaltic pump) using a Slide-A-Lyzer MINI
1220 dialysis device (3.5-kDa cutoff, Thermo Scientific). Following overnight dialysis, the samples
1221 were incubated at 37°C for 30 minutes to promote nucleosome repositioning and subjected to two
1222 final rounds of dialysis in nucleosome assembly end buffer. Samples were clarified by
1223 centrifugation, and nucleosome concentrations were determined by absorbance at 260 nm.
1224 Nucleosome quality was assessed by native polyacrylamide gel electrophoresis and ethidium
1225 bromide staining.

1226
1227 ***in vitro* pulldown assays**

1228 *in vitro* pulldown assays were performed using either biotinylated mononucleosomes or
1229 biotinylated histone peptides as binding substrates. For each assay, 1 µg of biotinylated substrate
1230 was preincubated with 10 µL of streptavidin Dynabeads™ M-280 at 4 °C to allow immobilization.
1231 Substrate–bead complexes were then incubated with 1 µg of purified recombinant proteins in
1232 200 µL of binding buffer containing: 150 mM NaCl, 20 mM Tris-HCl (pH 7.5), and 0.1% NP-40
1233 for 1 h at 4 °C with rotation. Following incubation, beads were washed three times with wash
1234 buffer containing: 350 mM NaCl, 20 mM Tris-HCl (pH 7.5), and 1% NP-40. Bound proteins were
1235 eluted by boiling beads in 30 µL of denaturing sample buffer and analyzed by western blotting.

1236
1237 **Flag–HA–QR2 immunoprecipitation and mass spectrometry**

1238 Flag–HA mock control, Flag–HA–tagged wildtype QR2, or Flag–HA–tagged QR2 I129EI195R
1239 mutant HeLa cell lines were cultured in DMEM to confluence. Dialyzed nuclear extracts were
1240 prepared as described above.

1241
1242 Flag M2 agarose beads were prewashed with 100 mM glycine (pH 2.7) and equilibrated in binding
1243 buffer (pH 7.5). For each immunoprecipitation, 50 µL of Flag M2 agarose beads were incubated
1244 with nuclear extract for 4 h at 4 °C with rotation. Beads were washed four times with dialysis buffer
1245 followed by four washes with detergent-free dialysis buffer. Bound proteins were processed for
1246 mass spectrometry using the same protocol described above.

1247
1248 **BNAH fluorescence-based enzymatic activity assay**
1249
1250 QR2 enzymatic activity was measured using a fluorescence-based BNAH oxidation assay.
1251 Oxidation of the reduced co-substrate 1-benzyl-1,4-dihydronicotinamide (BNAH) (Santa Cruz, sc-
1252 208609) by QR2 results in a time-dependent decrease in intrinsic BNAH fluorescence. Reactions
1253 were performed in assay buffer containing: 50 mM Tris-HCl (pH 8.0) and 0.1% Triton X-100,
1254 supplemented with 100 µM Menadione (K3, Sigma, 47775) and BNAH. Reactions were initiated
1255 by addition of recombinant QR2 (100 ng per reaction). Control reactions lacking enzyme were
1256 included to account for non-enzymatic BNAH decay. Fluorescence was monitored every 2 min
1257 using a SpectraMax iD5 plate reader with excitation at 340–355 nm and emission at 440–460 nm.
1258 Enzymatic activity was calculated from the linear decrease in fluorescence intensity over time.

1259
1260 **Lentivirus packaging**
1261

1262 HEK293T cells were maintained in DMEM supplemented with 10% fetal bovine serum (FBS),
1263 100 U mL^{-1} penicillin, and 100 μg mL^{-1} streptomycin. One day prior to transfection, 10-cm culture
1264 dishes were coated with 10 mL of poly-L-ornithine, incubated at 37 °C for 1 h, and washed twice
1265 with DPBS. HEK293T cells were dissociated using 0.25% trypsin–EDTA and seeded at a density
1266 of 7×10^6 cells per dish in 6 mL of DMEM. After 24 h, the medium was replaced with fresh
1267 DMEM and cells were transfected using a polyethylenimine (PEI)-based method. For each dish, a
1268 total of 20 μg plasmid DNA (10 μg lentiviral transfer plasmid, 5 μg pMDLg/pRRE, 2.5 μg RSV-
1269 Rev, and 2.5 μg pCMV-VSV-G) was diluted in 500 μL DMEM. In parallel, 60 μL of PEI
1270 (1 mg mL^{-1}) was diluted in 500 μL DMEM. DNA and PEI solutions were combined, incubated for
1271 20 min at room temperature to allow complex formation, and added dropwise to the cultures. Six
1272 hours after transfection, cells were washed once with DPBS and fresh, prewarmed DMEM was
1273 added. Viral supernatants were collected at 30 and 46 h post-transfection, filtered through a 0.45-
1274 μm membrane, and concentrated by ultracentrifugation at 21,000 rpm for 2 h at 4 °C. Viral pellets
1275 were resuspended overnight at 4 °C in DMEM/F12 supplemented with HEPES at a volume 100-
1276 fold smaller than the original supernatant. An equal volume of 1 M sucrose in DMEM/F12 was
1277 then added, and viral stocks were aliquoted and stored at −80 °C.
1278
1279 **Knockout and rescue of QR2 expression in HeLa cells**
1280
1281 *NQO2* knockout HeLa cell lines were generated using CRISPR–Cas9–mediated genome editing.
1282 Alt-R™ S.p. HiFi Cas9 Nuclease V3 (IDT, 1081061) was complexed with an Alt-R CRISPR–
1283 Cas9 single-guide RNA (sgRNA) targeting human *NQO2* (5′-CCCACGAAGCCTACAAGCAA-
1284 3′; IDT) and delivered into HeLa cells using the SE Cell Line 4D-Nucleofector™ X Kit S (Lonza,
1285 V4XC-1032) according to the manufacturer's instructions. Following nucleofection, single-cell
1286 clones were isolated and expanded, and *NQO2* knockout was confirmed by western blot analysis.

1287 For rescue experiments, the lentiviral backbone pLV-EF1α-IRES-Puro (Addgene #85132) was
1288 used to generate expression constructs encoding either Flag–HA–tagged wild-type *NQO2* or the
1289 I129EI195R *NQO2* mutant under the control of the endogenous *NQO2* promoter. Lentiviral
1290 particles were produced as described above and used to transduce *NQO2*-knockout HeLa cells in
1291 DMEM containing 8 μg mL^{-1} polybrene. Cells were incubated at 37 °C with 5% CO_2 for 24 h, then
1292 passaged and selected in DMEM containing 2.0 μg mL^{-1} puromycin. Selection medium was
1293 replaced every 3–4 days until resistant colonies were established. Re-expression of wildtype or
1294 mutant QR2 was verified by western blot analysis.

1295

1296 **Mice**

1297 CD1 mice (Charles River 022) were housed in specific-pathogen-free (SPF) conditions and
1298 environmentally controlled animal facilities with a 12-hour light-dark cycle and were given
1299 unrestricted access to food and water. All animal protocols and experiments were approved by the
1300 Institutional Animal Care and Use Committee (IACUC) of ISMMS. All experiments were
1301 performed following strict IACUC guidelines.

1302

1303 **Cerebellar granule neuron culture and depolarization**

1304 Cerebellar granule neurons were prepared from postnatal day 7 (P7) CD-1 mouse pups as
1305 previously described[76]. Briefly, neurons were cultured *in vitro* in high-potassium medium during
1306 days in vitro (DIV) 1–2 consisting of Basal Medium Eagle supplemented with 5% HyClone bovine
1307 growth serum, 1× penicillin–streptomycin, 1× GlutaMAX and 25 mM KCl. On DIV 3, the medium
1308 was replaced with low-potassium medium containing Basal Medium Eagle supplemented with 5%
1309 HyClone bovine growth serum, 1× penicillin–streptomycin, 1× GlutaMAX, and 5 mM KCl. On
1310 DIV 5, neurons were pretreated with 1 μM TTX and 100 μM DL-AP5 for 12 h to suppress

1311 spontaneous neuronal activity. For depolarization, cultures were switched to high-potassium
1312 medium (25 mM KCl) for 1 h, after which cells were collected for downstream analyses.
1313
1314 **Mouse glial cell preparation**

1315 Primary mouse glial cultures were prepared from CD-1 pups (postnatal days P1–P3) in accordance
1316 with institutional animal care and use guidelines. Pups were anesthetized by hypothermia and
1317 humanely euthanized on ice. Cerebral cortices were dissected in ice-cold HBSS supplemented with
1318 10 mM HEPES, and meninges were carefully removed. Cortical tissue was enzymatically
1319 dissociated by incubation with papain (80 µL), activated with 0.5 µM $CaCl_2$ and 1 µM EDTA, at
1320 37 °C for 15 min. Following digestion, tissue was gently triturated and passed through a 70 µm
1321 cell strainer. Cells were pelleted by centrifugation at 500g for 5 min and resuspended in mouse
1322 embryonic fibroblast (MEF) medium consisting of 435 mL DMEM, 50 mL HyClone™ Cosmic
1323 Calf Serum, 5 mL penicillin–streptomycin, 5 mL sodium pyruvate, 5 mL non-essential amino acids
1324 (NEAA), and 4 µL 2-mercaptoethanol. Cells were plated onto 10 cm tissue culture dishes, and the
1325 medium was replaced after 24 h. After 5–6 days in culture, glial cells were detached, resuspended
1326 in Bambanker freezing medium, and cryopreserved in liquid nitrogen until use.
1327
1328 **Human iPSC maintenance**

1329 The WTC11 human pluripotent stem cell (hPSC) line (hPSCreg UCSFi001-A)[46] was obtained
1330 from Coriell Institute for Medical Research, GM25256. Cells were maintained on six-well tissue
1331 culture plates coated with Geltrex diluted in DMEM/F-12 and cultured in StemFlex medium.
1332 Cultures were maintained at 37 °C in a humidified incubator with 5% CO_2, with medium changes
1333 performed every other day. Cells were passaged at approximately 80% confluency using 0.5 mM
1334 EDTA in DPBS at room temperature. Detached cells were resuspended in StemFlex medium

1335 supplemented with 5 nM Chroman1 and reseeded at split ratios adjusted according to cell density.
1336 The following day, the medium was replaced with fresh StemFlex medium lacking Chroman1, and
1337 cultures were subsequently maintained using this routine passaging protocol.
1338
1339 **Generation of human *NQO2*, *H3F3B*, and *TGM2* knock-in iPSC lines**
1340 Homozygous single- and double-knock-in human iPSC lines were generated in the WTC11
1341 background using CRISPR–Cas9–mediated homology-directed repair (HDR). Briefly, 1×10^6
1342 WTC11 iPSCs were electroporated using a 4D-Nucleofector system (Lonza; program V4XP-
1343 3024) with preassembled ribonucleoprotein complexes containing 10 µg S. pyogenes Cas9
1344 nuclease (IDT, 1081058), 8 µg synthetic single-guide RNA (sgRNA; Synthego, CRISPRevolution
1345 sgRNA EZ Kit), and 100 pmol single-stranded oligodeoxynucleotide (ssODN) donor template
1346 (Life Technologies). Following electroporation, cells were replated on Geltrex-coated plates and
1347 cultured in mTeSR Plus medium. Five days after electroporation, cells were dissociated with
1348 Accutase and single cells were sorted into 96-well plates using a WOLF benchtop microfluidic
1349 cell sorter (Nanocellect) in mTeSR Plus supplemented with CloneR. After 13 days of clonal
1350 expansion, genomic DNA was extracted from individual clones using QuickExtract DNA
1351 Extraction Solution (Lucigen, QE090500). Correct HDR events were identified by locus-specific
1352 PCR using GoTaq DNA Polymerase (Promega) followed by Sanger sequencing.
1353
1354 For *NQO2*, HDR was first used to introduce the I195R mutation in exon 7. Clone MSE2335A was
1355 identified as a correctly edited homozygous knock-in clone, whereas clone MSE2335B served as
1356 an isogenic wild-type control. Clone MSE2335A was subsequently subjected to a second round of
1357 CRISPR–Cas9 editing to introduce the I129E mutation in exon 5, generating a homozygous
1358 double-mutant line. For *H3F3B*, HDR was used to introduce the Q5A mutation in exon 2, yielding

1359 clone MSE2421A. A separate HDR strategy targeting the same exon was used to generate the Q5N
1360 mutation, and clone MSE2422A was used for downstream experiments. For *TGM2*, HDR was
1361 used to introduce the C277A mutation in exon 6, and clone MSE2340A was identified as a
1362 correctly edited homozygous knock-in line and used for subsequent analyses. Genomic integrity
1363 and normal karyotype were confirmed for all edited clones by SNP array analysis. Sequences of
1364 sgRNAs, ssODN donor templates, and PCR primers used for CRISPR–Cas9–mediated HDR are
1365 provided in **Supplementary Data 18**.
1366
1367 **Genomic integrity of human iPSC lines**
1368 The WTC-11 donor human iPSC line was tested for genomic integrity at passage 36 using SNP-
1369 array technology (Global Diversity Array v1.0 BeadChip, Illumina). All the edited clones were
1370 also tested at passage 4 after the genome editing. No detection of CNV larger than 1.5 Mb or AOH
1371 larger than 3 Mb were detected on somatic chromosomes. The typical WTC-11 deletion of 2.9 Mb
1372 on Yp11.2 was detected in all clones. This deletion is known to be present in the donor, from
1373 whom the cell line was derived[46].
1374
1375 **Generation of PiggyBac-integrated hPSC lines**
1376 For stable transgene integration, WTC11 hPSCs were seeded at a density of 3–4 × 10^5 cells per
1377 well in six-well tissue culture plates in StemFlex medium supplemented with Chroman1 and
1378 cultured overnight. On the following day, cells were transfected with a PiggyBac transgene
1379 plasmid encoding doxycycline-inducible human NGN2 (PB-TO-hNGN2; Addgene #172115)
1380 together with Super PiggyBac transposase (System Biosciences, PB210PA-1) using
1381 Lipofectamine Stem Transfection Reagent. Transfection complexes were prepared by separately
1382 diluting 8 µL of Lipofectamine Stem Transfection Reagent in 125 µL Opti-MEM I reduced-serum

1383 medium and mixing 500 ng of transposase plasmid and 1 μg of PB-TO-hNGN2 plasmid in 125 μL
1384 Opti-MEM I. The two solutions were then combined and incubated for 10 min at room temperature
1385 to allow complex formation. A total of 250 μL of the transfection mixture was added dropwise to
1386 cells pre-equilibrated in 2 mL of warm Opti-MEM I. Following a 4 h incubation at 37 °C, 2 mL of
1387 warm StemFlex medium was added, and cells were cultured overnight. On the subsequent day, the
1388 medium was replaced with 1.5 mL of fresh StemFlex medium. Selection was initiated on day 3 by
1389 switching to StemFlex medium supplemented with 2 μg mL^{-1} puromycin and maintained for 4–6
1390 days, with medium changes every other day. To ensure uniform selection and eliminate false-
1391 positive cells, cultures were passaged once in puromycin-containing StemFlex medium prior to
1392 further expansion.
1393
1394 **One-step neuronal induction via forced NGN2 expression**
1395 Glutamatergic neurons were generated by doxycycline-inducible overexpression of the
1396 transcription factor NGN2, as previously described[77]. PiggyBac–NGN2–integrated WTC11
1397 hPSCs were dissociated using Accutase for 5 min at 37 °C and resuspended in N3 induction
1398 medium supplemented with Chroman1 and doxycycline (Dox). N3 induction medium was
1399 prepared by combining 485 mL DMEM/F-12, 5 mL N2 supplement, 5 mL non-essential amino
1400 acids, 5 mL penicillin–streptomycin, and 10 mg insulin. Cells were counted and seeded at a density
1401 of 3×10^6 cells per Geltrex-coated 10-cm dish. Approximately 16–18 h after plating (day 1), the
1402 medium was replaced with fresh N3 medium containing Dox. On day 5, the medium was replaced
1403 with N3 medium supplemented with Dox and 4 μM cytosine β-D-arabinofuranoside (Ara-C). On
1404 day 7, cells were dissociated by incubation with Accutase for 20 min at 37 °C and resuspended in
1405 Neurobasal-zero medium supplemented with Chroman1. Neurobasal-zero medium was prepared
1406 by combining 483 mL Neurobasal medium, 5 mL GlutaMAX, 10 mL B27 supplement, and 2.5 mL

1407 penicillin–streptomycin. Cells were then co-cultured with mouse glial cells in NBP medium and
1408 plated onto pre-coated six-well plates. NBP medium consisted of Neurobasal-zero supplemented
1409 with 5% fetal bovine serum (FBS), Chroman1, and Dox. On day 8, the medium was replaced with
1410 Neurobasal-zero containing 2% FBS (NB-2%). On day 14, cultures were transitioned to
1411 Neurobasal-A-zero medium containing 1% FBS (NBA-1%). Neurobasal-A-zero medium was
1412 prepared by combining 483 mL Neurobasal-A, 5 mL GlutaMAX, 10 mL B27 supplement, and
1413 2.5 mL penicillin–streptomycin. From day 14 onward, 30% of the medium was replaced twice
1414 weekly until day 35, at which time neurons were used for functional and molecular analyses.
1415
1416 **Time-course of neuronal differentiation**
1417 For time-course analyses of neuronal differentiation, samples were collected at six developmental
1418 stages: undifferentiated hPSCs (day 0), and induced neurons at days 6, 12, 20, 27, and 35 for RNA
1419 sequencing. CUT&RUN profiling was performed on undifferentiated hPSCs (day 0) and mature
1420 induced neurons at day 35.
1421
1422 **Depolarization treatment**
1423 For membrane depolarization experiments, neurons were pretreated with 1 μM TTX and 100 μM
1424 DL-AP5 for 12 h to suppress spontaneous neuronal activity. Depolarization was then induced by
1425 the addition of a high-potassium buffer (170 mM KCl, 2 mM $CaCl_2$, 1 mM $MgCl_2$, and 10 mM
1426 HEPES) to achieve a final extracellular KCl concentration of 55 mM, as previously described[78].
1427 Untreated control neurons and neurons subjected to 1 h of depolarization were harvested for RNA
1428 sequencing.
1429
1430 **Human Subjects**

1431 Postmortem human brain tissue samples were obtained from patients who had enrolled in and
1432 provided consent for the brain donation program through the Neuropathology Brain Bank &
1433 Research CoRE at Mount Sinai, RRID: SCR_027565. These samples were collected according to
1434 ethical guidelines and institutional review board (IRB) approval, ensuring the privacy and dignity
1435 of the donors while supporting ongoing neuropathological research. All specimens obtained were
1436 de-identified. Brain specimens were dissected by expert neuroanatomists into defined blocks. One
1437 hemisphere was flash-frozen and stored at −80 °C until processing. Nuclei isolation and peptide
1438 pulldown assays were conducted, as previously described.

1439 **Bulk RNA-seq and analysis**

1440 *RNA isolation, library preparation, and sequencing*

1441 RNA-seq was performed on HeLa cells and on human iPSC-derived neurons co-cultured with
1442 mouse glia across multiple experimental conditions, including genetic perturbations,
1443 differentiation stages, and depolarization treatments. All datasets were processed using the same
1444 experimental and computational pipelines unless otherwise noted. Cells were lysed in TRIzol
1445 reagent (Invitrogen, 15596026), and total RNA was extracted according as follows. Chloroform
1446 was added in a 5:1 ratio, and the aqueous phase was isolated. An equal volume of 70% ethanol
1447 was added, and the mixture was applied to RNeasy Micro spin columns (Qiagen, 74004). RNA
1448 purification was completed following the Qiagen RNeasy Micro Kit protocol, including all
1449 optional steps and on-column DNase treatment. RNA was eluted in 15 μL and quantified using a
1450 NanoDrop spectrophotometer. Only samples with A260/280 and A260/230 ratios greater than 1.8
1451 were used for downstream applications. For library preparation**,** 100 ng of total RNA was used as
1452 input for the Illumina Stranded mRNA Prep, Ligation kit (Illumina, 20040534). Libraries were
1453 amplified with 14 cycles of PCR, and amplified fragments were purified using AMPure XP beads

1454 (Beckman Coulter, A63881). Library concentration and fragment size distribution were assessed
1455 using a Qubit dsDNA HS assay (Invitrogen, Q33231) and a High Sensitivity D5000 TapeStation
1456 assay (Agilent Technologies, 5067-5592, 5067-5593). Libraries were pooled at equimolar
1457 concentrations and sequenced on an Illumina NovaSeq X+ platform at the NYU Genome
1458 Technology Center. HeLa cell libraries were sequenced to a depth of 50–60 million paired-end
1459 reads per sample, whereas libraries generated from human iPSC-derived neurons co-cultured with
1460 mouse glia were sequenced to a depth of approximately 100 million paired-end reads (150 bp) per
1461 sample to enable robust species-specific read assignment.
1462
1463 *Differential expression analysis*
1464 For HeLa cell RNA-seq datasets, raw FASTQ files were pseudoaligned and quantified using
1465 kallisto (v0.46.1)[79] against a GRCh38 (hg38) human transcriptome reference derived from
1466 Ensembl release 86. For human iPSC-derived neurons co-cultured with mouse glia, reads were
1467 pseudoaligned against a combined human–mouse transcriptome reference generated by
1468 concatenating Ensembl human (GRCh38, release 86) and mouse (GRCm38/mm10, release 79)
1469 transcriptomes, and human-mapped transcripts were retained for downstream analyses. Reads
1470 corresponding to the human transcriptome were subsequently extracted for downstream analyses.
1471 To reduce noise from lowly expressed transcripts, genes with a total read count of fewer than 15
1472 reads across all samples were excluded. Differential gene expression analysis was performed using
1473 DESeq2 (v1.38.3)[80]. Gene-level count matrices were normalized using the DESeq2 median-of-
1474 ratios method, and differential expression was assessed using the Wald test. P values were adjusted
1475 for multiple testing using the Benjamini–Hochberg procedure, with an adjusted P value < 0.05
1476 considered statistically significant.
1477

1478 *Gene expression overlap analyses*

1479 Transcriptome-wide, threshold-free gene expression overlap was visualized using Rank-Rank
1480 Hypergeometric Overlap (RRHO) heatmaps generated with the RRHO2 package (v1.0)[81]. Gene
1481 lists were ranked by signed p-values, calculated as the log10-transformed nominal p-value
1482 multiplied by the sign of the fold change, without applying differential expression thresholds.

1483

1484 **Chromatin immunoprecipitation**

1485 Untreated and depolarization mouse cultured granule neuron cells (1×10^7 cells per sample) were
1486 crosslinked with 1% formaldehyde for 10 min at room temperature and quenched with 125 mM
1487 glycine for 5 min. Cells were washed thoroughly prior to lysis and chromatin shearing by
1488 sonication, as previously described[1]. Sonicated chromatin was incubated overnight at 4 °C with
1489 rotation with antibody-conjugated Dynabeads™ M-280 (7.5 µg antibody per sample). Antibodies
1490 used included anti-H3K4me3Q5ser, anti-H3Q5ser, anti-NQO2, and anti–RNA polymerase II. The
1491 following day, immunocomplexes were washed, eluted, and reverse-crosslinked, as previously
1492 described[1]. After RNase A and proteinase K digestion, DNA fragments were purified using the
1493 QIAquick PCR Purification Kit (QIAGEN, 28104).

1494

1495 **ChIP-seq library preparation and analysis**

1496 Purified ChIP DNA was used to prepare sequencing libraries using the NEBNext® Ultra™ II DNA
1497 Library Prep Kit for Illumina (NEB, E7645L) following the manufacturer's protocol. Libraries
1498 were sequenced as paired-end reads (50 bp) on an Illumina NovaSeq X+ platform to a depth of
1499 approximately 30 million reads per sample. ChIP-seq peak calling and differential analyses were
1500 performed as previously described, with minor modifications[1]. Raw sequencing reads were aligned
1501 to the mouse reference genome (mm10) using the NGS Data Charmer pipeline with default settings

1502 (HISAT v0.1.6b)[82]. Peak calling was performed using MACS2 (v2.1.1)[83], normalized to the
1503 corresponding input controls, with a false discovery rate (FDR) threshold of < 0.01. Differential
1504 peak analysis was conducted using pairwise comparisons in the DiffBind package (v3.8.4)[84] to
1505 identify depolarization-induced changes in H3Q5ser, H3K4me3Q5ser, NQO2, and RNA
1506 polymerase II (Pol II) occupancy. Identified peaks and differentially enriched regions were
1507 annotated to nearby genes or intergenic regions using the ChIPseeker[85] package in R. Visualization
1508 of differential binding profiles was performed using internal functions of DiffBind or deepTools[86].
1509
1510 **CUT&RUN**

1511 *Cells*

1512 Hela cells or human iPSC-derived neurons co-cultured with mouse glia cells were resuspended in
1513 1 mL of nuclear extract (NE) buffer (20 mM HEPES-KOH, pH 7.9, 10 mM KCl, 0.5 mM
1514 spermidine, 0.1% Triton X-100, 20% glycerol and freshly added protease inhibitors (Roche,
1515 11836170001) and passed through a 21-gauge needle 20 times to lyse the cells. Nuclei were
1516 pelleted at 1,100*g* for 5 min at 4 °C and the supernatant was discarded. Nuclei were washed again
1517 in 1 mL NE buffer and counted. In total, 100,000 nuclei were used per biological replicate.
1518
1519 *CUT&RUN*

1520 CUT&RUN was performed as previously described, with minor modifications[42,87,88]. BioMag Plus
1521 Concanavalin A beads (Polysciences, 860573) were prepared by washing 15 µL bead slurry per
1522 reaction three times with binding buffer (20 mM HEPES-KOH, pH 7.9, 10 mM KCl, 1 mM $CaCl_2$,
1523 1 mM $MnCl_2$) and resuspending the beads in the original volume. Beads (15 µL) were aliquoted
1524 into DNA low-bind tubes, and 500 µL nuclear extraction buffer was added. A total of 100,000
1525 nuclei were added to each tube and incubated with beads by end-over-end rotation at room

1526 temperature for 10 min. Bead-bound nuclei were washed three times with 1 mL wash buffer (WB;
1527 20 mM HEPES, pH 7.5, 150 mM NaCl, 0.1% Triton X-100, 0.1% Tween-20, 0.5 mM spermidine,
1528 0.1% BSA, freshly supplemented with protease inhibitors). Nuclei were then resuspended in
1529 100 μL antibody buffer (wash buffer supplemented with 2 mM EDTA). Primary antibodies (2 μL
1530 per reaction; 1:50 dilution) against H3Q5ser, H3K4me3Q5ser, RNA polymerase II, NQO2,
1531 POU2F1, or IgG control were added, and bead-bound nuclei were incubated overnight at 4 °C with
1532 gentle horizontal rotation with tubes at a 45 degree angle. The following day, nuclei were washed
1533 twice with 1 mL cold wash buffer and resuspended in 50 μL cold wash buffer. Protein A/G–MNase
1534 (pAG-MNase; Epicypher, 15-1016; 2.5 μL per reaction) was added, and samples were incubated
1535 for 1 h at 4 °C with the same rotation. Nuclei were subsequently washed three times with 1 mL
1536 ice-cold wash buffer, followed by one wash with 1 mL low-salt rinse buffer (20 mM HEPES,
1537 pH 7.5, 0.5 mM spermidine, 0.1% Tween-20, 0.1% Triton X-100). Bead-bound nuclei were
1538 resuspended in ice-cold calcium incubation buffer (3.5 mM HEPES, pH 7.5, 10 mM $CaCl_2$, 0.1%
1539 Tween-20, 0.1% Triton X-100) and incubated on ice (0 °C) for 30 min for MNase digestion.
1540 Reactions were quenched by addition of 100 μL of 2× stop buffer (340 mM NaCl, 20 mM EDTA,
1541 5 mM EGTA, 0.1% Tween-20, 0.1% Triton X-100, 25 μg mL^{-1} RNase A (Thermo Scientific,
1542 EN0531), and 0.05 ng per 100 μL *E. coli* spike-in DNA (Epicypher, 18-1401)). Samples were
1543 incubated at 37 °C for 30 min without shaking to allow chromatin release and RNA digestion.
1544 Beads were captured using a magnetic rack, and the supernatant (200 μL) containing released DNA
1545 fragments was collected. DNA was purified using the Zymo ChIP DNA Clean & Concentrator kit
1546 (Zymo Research, D5205), eluted in 30 μL, and stored at −20 °C for library preparation.

1547
1548 *CUT&RUN-seq library preparation and sequencing*

1549 Library preparation was performed using the NEBnext Ultra II DNA library kit (E7645L) with
1550 multiplexed adapters with minor modifications. CUT&RUN DNA underwent end repair and
1551 adapter ligation according to the manufacturer's protocol (1:15 adapter dilution). DNA was
1552 amplified using 16 PCR cycles with an amended 10 s of extension time per cycle to enrich for
1553 short fragments. DNA was enriched for 150–350 bp fragments for transcription factor binding
1554 events and 150–800 bp for histone markers using Ampure XP beads cleanup. Libraries were
1555 quantified with Qubit dsDNA HS assay (Invitrogen, Q33231), and the size distribution was
1556 determined by High Sensitivity D5000 TapeStation assay (Agilent Technologies, 5067-5592,
1557 5067-5593). Libraries were pooled at an equimolar concentration and sequenced on the Illumina
1558 NovaSeq X+ sequencer by the NYU Genome Technology Center. HeLa cell libraries were
1559 sequenced to a depth of 20–30 million paired-end reads per sample**,** whereas libraries generated
1560 from human iPSC-derived neurons co-cultured with mouse glia were sequenced to a depth of
1561 approximately 50 million paired-end reads (150 bp) per sample to enable robust species-specific
1562 read assignment.

1563
1564 *CUT&RUN–seq data analysis*

1565 CUT&RUN data were analyzed as previously described, with minor modifications[88]. For human
1566 iPSC-derived neurons co-cultured with mouse glia, reads were aligned using Bowtie2 (v2.5.0)[89]
1567 to a concatenated reference genome comprising the human genome (GRCh38/hg38), the mouse
1568 genome (GRCm38/mm10), and the Escherichia coli genome used as a spike-in control. Paired-
1569 end reads were aligned using Bowtie2 (v2.5.0) with the `--very-sensitive` preset and Phred+33
1570 encoding. Insert size parameters were set to 10–2000 bp (`-I 10 -X 700`), and dovetailing read

1571 pairs were permitted (`--dovetail`). For HeLa cell samples, reads were aligned to a concatenated
1572 reference consisting of GRCh38/hg38 and the *E. coli* genome. Aligned reads were filtered using
1573 SAMtools (v1.9)[90] to retain only uniquely mapped reads with a minimum mapping quality
1574 (MAPQ) score of 30. Reads were subsequently separated by species (human, mouse, and *E. coli*)
1575 for downstream analyses. For normalization and quantitative comparisons across samples, *E. coli*
1576 spike-in DNA was used to calculate a scaling factor for each sample, defined as the median number
1577 of uniquely mapped *E. coli* reads across all samples divided by the number of *E. coli* reads in the
1578 given sample. This scaling factor was applied to normalize human-aligned read counts and genome
1579 coverage tracks. Genome coverage tracks were generated as bigWig files using the deepTools
1580 (v3.5.5)[91] bamCoverage function, and regions with consistently high background signal were
1581 excluded using the ENCODE hg38 blacklist (v2). Heatmaps were generated using deepTools
1582 (v3.5.5) computeMatrix and plotHeatmap functions in reference-point mode, centered on peak
1583 centers. Peak calling was performed using MACS2[83] with a false discovery rate (FDR) threshold
1584 of < 0.01. Differential peak analysis was conducted using DiffBind[84] by quantifying read counts
1585 across consensus peak regions and statistically testing for condition-dependent differences in
1586 chromatin occupancy. Identified peaks and differentially enriched regions were annotated, and
1587 motif enrichment analyses were performed using the ChIPseeker[85] package in R.

1588

1589 **ATAC–seq**

1590 *Nuclei preparation*

1591 Nuclei from induced neurons (iNs) were prepared using the same nuclei isolation procedure as
1592 described for CUT&RUN. For each biological replicate, 100,000 nuclei were used as input for
1593 ATAC–seq library preparation.

1594

1595 *ATAC-seq library preparation*

1596 ATAC-seq libraries were generated using the ATAC-Seq Express Kit (Active Motif, 53157)
1597 according to the manufacturer's instructions. Libraries were size-selected using SPRIselect Bead-
1598 Based Reagent (Beckman, B23318) to enrich for fragments ranging from 200 to 800 bp. Library
1599 quality and fragment size distribution were assessed using a High Sensitivity D5000 TapeStation
1600 assay (Agilent Technologies; 5067-5592, 5067-5593). Libraries were pooled at equimolar
1601 concentrations and sequenced as 150-bp paired-end reads on an Illumina NovaSeq X+ platform at
1602 the NYU Genome Technology Center, yielding approximately 60 million reads per sample.

1603

1604 *ATAC-seq data processing and analysis*

1605 Primary ATAC-seq data processing included adapter trimming, alignment to a concatenated
1606 human–mouse reference genome comprising the human genome (GRCh38/hg38) and the mouse
1607 genome (GRCm38/mm10) using Bowtie2[89], and removal of mitochondrial reads and PCR
1608 duplicates. Peak calling was performed independently for each of the three biological replicates
1609 using MACS2[83], followed by assessment of reproducibility across replicates. Normalization and
1610 differential chromatin accessibility analyses were conducted using DiffBind[84]. Transcription factor
1611 footprinting analysis was performed using TOBIAS[92], which corrects ATAC–seq signal for Tn5
1612 transposase sequence bias and local chromatin accessibility prior to footprint inference.
1613 Differential transcription factor binding activity was quantified using the BINDetect module by
1614 comparing footprint depth and flanking accessibility at motif instances, enabling condition-
1615 specific comparison of POU2F1 binding scores between wild-type and mutant samples. To assess
1616 whether loss of chromatin accessibility in mutant neurons was associated with loss of POU2F1
1617 (OCT1) binding motifs, we performed motif scanning of ATAC-seq peaks using POU2F1
1618 consensus motifs from the JASPAR database (MA0785.1 and MA0785.2). Genomic coordinates

1619 of ATAC-seq peaks were scanned for motif occurrences to classify loci as OCT1 motif–positive
1620 (OCT1^{+}) or OCT1 motif–negative (OCT1^{-}). Differential accessibility analysis was used to identify
1621 ATAC peaks showing reduced accessibility in mutant compared with wild-type hiPSC-derived
1622 neurons.
1623
1624 **Odds ratio analysis integrating RNA-seq and CUT&RUN**
1625 To quantify the association between transcriptional changes and chromatin occupancy, an odds
1626 ratio (OR) framework was used to integrate RNA-seq and CUT&RUN datasets. Differential gene
1627 expression was assessed for each mutant relative to wild-type (WT) using DESeq2[80], and
1628 differentially expressed genes (DEGs) were defined as genes with an adjusted P value < 0.05 and
1629 an absolute $\log_2$ fold-change ≥ 0.5.
1630
1631 CUT&RUN peaks were called per biological replicate using MACS2[83], and differential binding
1632 between WT and mutant conditions was assessed using DiffBind[84]. For each CUT&RUN dataset
1633 (NQO2, H3K4me3Q5ser, or RNA polymerase II), WT-enriched CUT&RUN peaks were
1634 annotated to genes using ChIPseeker[85] by assigning peaks to the nearest transcription start site
1635 (TSS), with promoter regions defined as ±3 kb around the TSS (tssRegion = −3,000 to +3,000).
1636 Annotations were performed using TxDb.Hsapiens.UCSC.hg38.knownGene together with the
1637 org.Hs.eg.db database. Genes associated with at least one WT-enriched CUT&RUN peak within
1638 this window were classified as "bound." For each mutant and each CUT&RUN dataset, enrichment
1639 was tested using a 2×2 contingency table constructed across the expressed gene universe (genes
1640 passing RNA-seq filtering), stratified by (i) DEG status (DEG vs non-DEG) and (ii) CUT&RUN
1641 association (bound vs unbound). Odds ratios, 95% confidence intervals, and two-sided P values
1642 were computed using Fisher's exact test[93]. Odds ratios greater than 1 indicate enrichment of DEGs

among genes associated with WT-enriched CUT&RUN signal. Where applicable, P values were adjusted for multiple testing as indicated.

Analysis of dendritic arborizations

Immunofluorescence imaging was performed on mature induced neurons (iNs) following sparse labeling with an hSYN-EGFP expression plasmid introduced by calcium phosphate–mediated transfection. Images were acquired using an EVOS™ M5000 Imaging System equipped with a 20× objective. For each condition, 20 EGFP-positive neurons per biological replicate were analyzed using FIJI. Quantitative morphological analyses included total neurite outgrowth, defined as the summed length of all neurites per neuron; the number of processes, defined as primary neurites emerging from the soma; neurite branch points; and cell body area.

Immunofluorescence staining

Cells were washed with DPBS and fixed with 4% paraformaldehyde (PFA) for 5 min at room temperature. Following three washes with DPBS, cells were permeabilized with 0.2% Triton X-100 for 5–10 min at room temperature. Non-specific binding was blocked for 2 h at room temperature in blocking buffer consisting of DPBS supplemented with 4% bovine serum albumin (BSA; Sigma, A9647), 1% fetal bovine serum (FBS), and 0.02% sodium azide (Sigma, 71289). For human iPSC-derived neurons, cells were incubated overnight at 4 °C with primary antibodies diluted in blocking buffer, including anti-MAP2 (1:20,000), anti-Synapsin I/II (1:500), and anti-PSD95 (1:500). For cultured mouse cerebellar granule neurons, cells were incubated overnight at 4 °C with anti-NQO2 (1:1,000) and anti-H3K4me3Q5ser (1:1,000). For mouse brain slices, tissues were incubated with anti-NQO2 under the same conditions. After three washes with DPBS, cells or tissue sections were incubated for 1 h at room temperature in the dark with species-specific

1667 secondary antibodies diluted in blocking buffer: Alexa Fluor 488–conjugated anti-chicken IgY
1668 (H+L), Alexa Fluor 555–conjugated anti-rabbit IgG (H+L), and Alexa Fluor 647–conjugated anti–
1669 guinea pig IgG (H+L) (all at 1:1,000). Samples were washed three times with DPBS, and nuclei
1670 were counterstained with DAPI (0.2 ng mL^{-1}; Thermo Fisher Scientific, 62248) during the final
1671 wash. Coverslips were mounted using ProLong Gold Antifade Mountant with DAPI (Invitrogen,
1672 P36941).
1673
1674 **Synaptic puncta density analysis**
1675 Immunofluorescence analyses were performed on mature induced neurons stained for
1676 microtubule-associated protein 2 (MAP2) to label dendrites and either Synapsin I/II (SYN1) or
1677 PSD95 to label pre- or post-synaptic puncta, respectively. Confocal images were acquired using a
1678 Leica SP8 inverted confocal microscope equipped with a 40× oil-immersion objective. Z-stack
1679 images were collected from ten randomly selected fields per condition, converted to maximum-
1680 intensity projections, and analyzed using FIJI software. Cell bodies were masked prior to analysis.
1681 Synaptic puncta number was normalized to the total MAP2-positive area to calculate puncta
1682 density, or to the mean MAP2 fluorescence intensity to calculate puncta intensity. In addition,
1683 puncta size and fluorescence intensity were quantified.
1684
1685 **Colocalization analysis**
1686 Synaptic colocalization was assessed between presynaptic SYN1 and postsynaptic density protein
1687 95 (PSD95). To minimize background and non-synaptic signal, particle size thresholds were
1688 applied in FIJI prior to analysis. SYN1-positive puncta were segmented using a size range of 0.05–
1689 3 μm^2, whereas PSD95-positive puncta were segmented using a size range of 0.05–1 μm^2.
1690 Following thresholding and size filtering, binary masks were generated for each channel, and

1691 colocalized puncta were defined as pixels positive for both SYN1 and PSD95. The degree of
1692 synaptic colocalization was quantified using Manders' overlap coefficient, calculated as the
1693 fraction of double-positive signal. Identical acquisition settings, thresholding parameters, and size
1694 filters were applied across all experimental conditions.

1695

1696 **Multielectrode array (MEA) recordings**

1697 Neuronal network activity was recorded using the Maestro Pro multielectrode array system (Axion
1698 Biosystems). Recordings were performed for 10 min per well under controlled conditions (37 °C,
1699 5% CO_2). Signals were acquired at a sampling rate of 12.5 kHz per channel and filtered using a
1700 Butterworth band-pass filter (200–3,000 Hz). Both positive- and negative-deflecting spikes were
1701 detected using an adaptive threshold set at six times the standard deviation of the baseline noise.
1702 Stimulation and pharmacological assays were primarily conducted at day 35 of neuronal
1703 differentiation. For inhibitor experiments, baseline activity was recorded prior to compound
1704 addition. Inhibitors were prepared as 10× stock solutions and rapidly added to the existing culture
1705 medium at 1/9 of the total volume to achieve the desired final concentration (10 μM). Stock
1706 solutions were prepared in DMSO, with the final DMSO concentration maintained below 0.1%.
1707 Following compound addition, neuronal activity was recorded for an additional 10 min. MEA data
1708 analysis was performed using the Neural Metrics Tool software package (Axion Biosystems).

1709

1710

1711 **ACKNOWLEDGEMENTS**

1712 We would like to thank members of the Maze lab for their helpful discussions on this study. This
1713 work was partially supported by grants from the National Institutes of Health: R01 MH116900
1714 (I.M.), F32 MH140478 (B.H.W.), F32 MH126534 (J.C.O'C.), R21 NS130319 (S.G.M.), as well
1715 as funds from the Brain and Behavior Research Foundation (J.C.C.), the Damon Runyon Cancer

1716 Research Foundation (DRG-2506-23; J.Z.), the Cindy Silvian Foundation (S.G.M.), and the
1717 Howard Hughes Medical Institute (I.M.). Additional support was provided by the National Natural
1718 Science Foundation of China (22425702 to X.D.L.; 22577080 to X. L.), the General Research
1719 Fund (GRF 17107123, 17310122, 17302524, 17102124, 17104923, and 17311025 to X.D.L.), the
1720 Large Research Equipment Fund 2022–2023 of the University of Hong Kong (X.D.L.), and the
1721 Guangdong Provincial Project (2023QN10C205 to X.D.L.). All schematics were created with
1722 Biorender.com. Experiments were supported by the Stem Cell Engineering Core
1723 (RRID:SCR_027503) at the Icahn School of Medicine at Mount Sinai. We thank R. M. Vabulas
1724 for providing plasmids for the expression of QR1 and QR2 in *E. coli*.

1725 **AUTHOR CONTRIBUTIONS**
1726
1727 M.C., C.Y., X.L., X.D.L. H.L., and I.M. conceived of the study, designed the experiments, and
1728 interpreted the data. M.C. performed most biochemical-, molecular-, epigenomic-, and cellular-
1729 based assays. X.L. performed chemical proteomics experiments. L.K. performed peptide pulldown
1730 assays from HeLa NEs and ChIP/Re-ChIP experiments in cGNs. C.Y., X.L., R.Z., and H.L.
1731 performed structural and ITC analyses, and interpreted the data. B.H.W., X.W., J.C.O'C, D.A.V.,
1732 A.R., and L.S. assisted with bioinformatics analyses. B.C. provided general experimental
1733 assistance. X.L., Q.Z., and Y.D., generated H3 peptides (modified and unmodified). J.Z, K.M.C.,
1734 J.R.S, and T.W.M. generated semisynthetic mononucleosomes (modified *vs.* unmodified). K.R.
1735 provided QR2 inhibitors. Z.L. and H.M. performed LC-MS/MS analyses. E.B., R.H., and S.G.M.
1736 assisted with hiPSC maintenance, gene editing, and differentiation. M.C., C.Y., X.L., X.D.L., H.L.,
1737 and I.M. wrote the manuscript.
1738
1739 **COMPETING INTERESTS**
1740

The authors declare no competing interests.

DATA AVAILABILITY

The genomics data generated in this study have been deposited in the National Center for Biotechnology Information Gene Expression Omnibus (GEO) database under the SuperSeries GSE324882. All mass spectrometry-based proteomics data have been deposited to the ProteomeXchange Consortium via the PRIDE partner repository with the datasets identified as PXD075254 and PXD075547. The atomic coordinates and structure factors have been deposited in the Protein Data Bank (PDB) under PDB ID codes 24PZ and 24RO. We declare that the data supporting findings for this study are available within the article and Supplementary Information. Related data including raw microscopy images are available from the corresponding author upon reasonable request. No restrictions on data availability apply.

CODE AVAILABILITY

Related code is available from the corresponding author on reasonable request.

1778 **EXTENDED DATA TABLES/FIGURES AND LEGENDS**

NO.	Proteins	Ligands	deltaH (cal/mol)	deltaS (cal/mol/deg)	Ka (M-1)	N value	Relevant Figure Panel
1	QR2	H3(1-10)	/	/	/	/	Figure 1h
2	QR2	H3(1-10)K4me3	/	/	/	/	Figure 1h
3	QR2	H3(1-10)Q5ser	-7307±47.26	0.726	3.25E5±1.60E	0.840±0.00403	Figure 1h
4	QR2	H3(1-10)K4me3Q5ser	-5831±81.06	5.71	3.35E5±2.65E	1.00±0.0074	Figure 1h
5	QR2	H3(1-15)Q5his	/	/	/	/	Figure 1i
6	QR2	H3(1-15)Q5dop	/	/	/	/	Figure 1i
7	QR2	H3(1-10)Q5ser	-6.65 ± 0.06	4.18	1.63 ± 0.16	1.04 ± 0.01	Extended Data Figure 2c
8	QR2 (apo)	H3(1-10)Q5ser	/	/	/	/	Extended Data Figure 2c
9	QR2-Q122A	H3(1-10)Q5ser	-4.31 ± 0.08	6.07	32.7 ± 1.4	0.93 ± 0.01	Extended Data Figure 4a
10	QR2-F126A	H3(1-10)Q5ser	-2.51 ± 0.11	10.4	79.4 ± 9.2	1.00 ± 0.00	Extended Data Figure 4a
11	QR2-F178A	H3(1-10)Q5ser	-3.21 ± 0.05	9.27	41.8 ± 1.5	1.03 ± 0.01	Extended Data Figure 4a
12	QR2-Q122A/F126A/F178A	H3(1-10)Q5ser	/	/	/	/	Extended Data Figure 4a
13	QR2 I129EI195R	H3(1-10)Q5ser	-1.116E4±72.20	-8.41	2.21E6±1.03E5	0.626±0.00143	Extended Data Figure 5a
14	QR2 I129EI195R	5-HT	-1.118E4±236.9	-13.5	1.73E5±8.78E3	0.233±0.00378	Extended Data Figure 5b
15	QR2 I129EI195R	H3(1-10)Q5ser	-1.216E7±1.188E10	-4.07E+04	7.93E3±2.85E3	5.73E-4±0.560	Extended Data Figure 5a
16	QR2 I129EI195R	5-HT	-1.153E4±272.5	-14.4	1.97E5±1.71E4	0.362±0.00635	Extended Data Figure 5b

1779

1780 **Extended Data Table 1: ITC statistics**

1781

Crystal	QR2-H3Q5ser	QR2-H3K4me3Q5ser
Data collection		
Wavelength(Å)	0.9792	0.9792
Space group	$P4_32_12$	$P4_32_12$
Cell dimensions		
a, b, c (Å)	119.0, 119.0, 149.8	119.9, 119.9, 150.2
α, β, γ (˚)	90, 90, 90	90, 90, 90
Resolution (Å)	50 - 2.40 (2.44 - 2.40)	50 - 2.59 (2.63 - 2.59)
No. of reflections	42961 (2094)	34824 (1749)
R_{merge} (%)	20.0 (98.3)	21.1 (120.6)
R_{pim} (%)	4.0 (20.0)	7.1 (42.7)
I/σ (I)	20.0 (3.0)	14.3 (2.6)
CC1/2 (%)	99.5 (89.4)	99.1 (77.5)
Completeness (%)	100.0 (100.0)	99.6 (100.0)
Redundancy	25.8 (24.8)	9.6 (8.4)
Refinement (F>0)		
R_{work}/R_{free} (%)	16.3/21.2	15.5/20.2
No. of non-H atoms		
Protein	7290	7285
Peptide	300	300
Water	472	315
Average B-factor ($Å^2$)		
Protein	40.1	36.5
Peptide	38.9	33.7
Water	38.7	32.8

RMSD bonds (Å)	0.003	0.005
RMSD angels (˚)	0.595	0.806
Ramachandran plot		
Favored (%)	96.01	97.13
Allowed (%)	3.99	2.87
Outliers (%)	0.00	0.00

Extended Data Table 2: X-ray crystallography data collection and refinement statistics

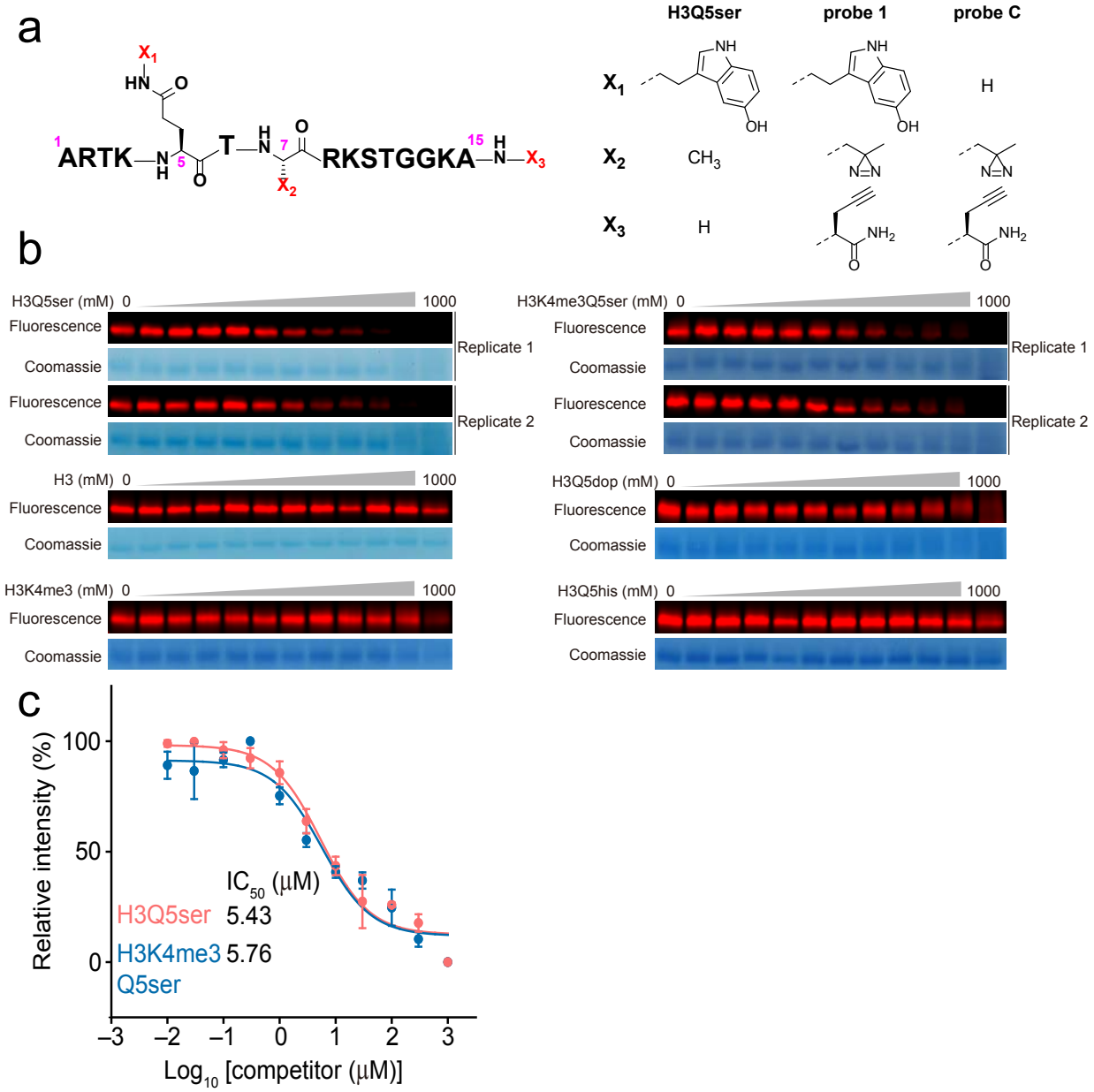

1788 **Extended Data Figure 1. QR2 selectively binds to H3Q5ser**
1789
1790 (**a**) Chemical structures of H3Q5ser, probe 1, and probe C. (**b**) In-gel fluorescence scanning results
1791 of different H3 peptides competing with probe 1-induced labeling of recombinant QR2. (**c**)
1792 Determination of IC_{50} for inhibition of probe 1-induced labeling of QR2 by H3Q5ser and
1793 H3K4me3Q5ser peptides. The fluorescence intensity of each band was quantified by ImageJ. All
1794 curves were normalized between 100 and 0% at the highest and lowest fluorescence intensities,
1795 respectively. Data are reported as mean ± SD (n = 2). All immunoblotting experiments repeated
1796 3X. See **Supplementary Figure 1** for uncropped blots.
1797
1798

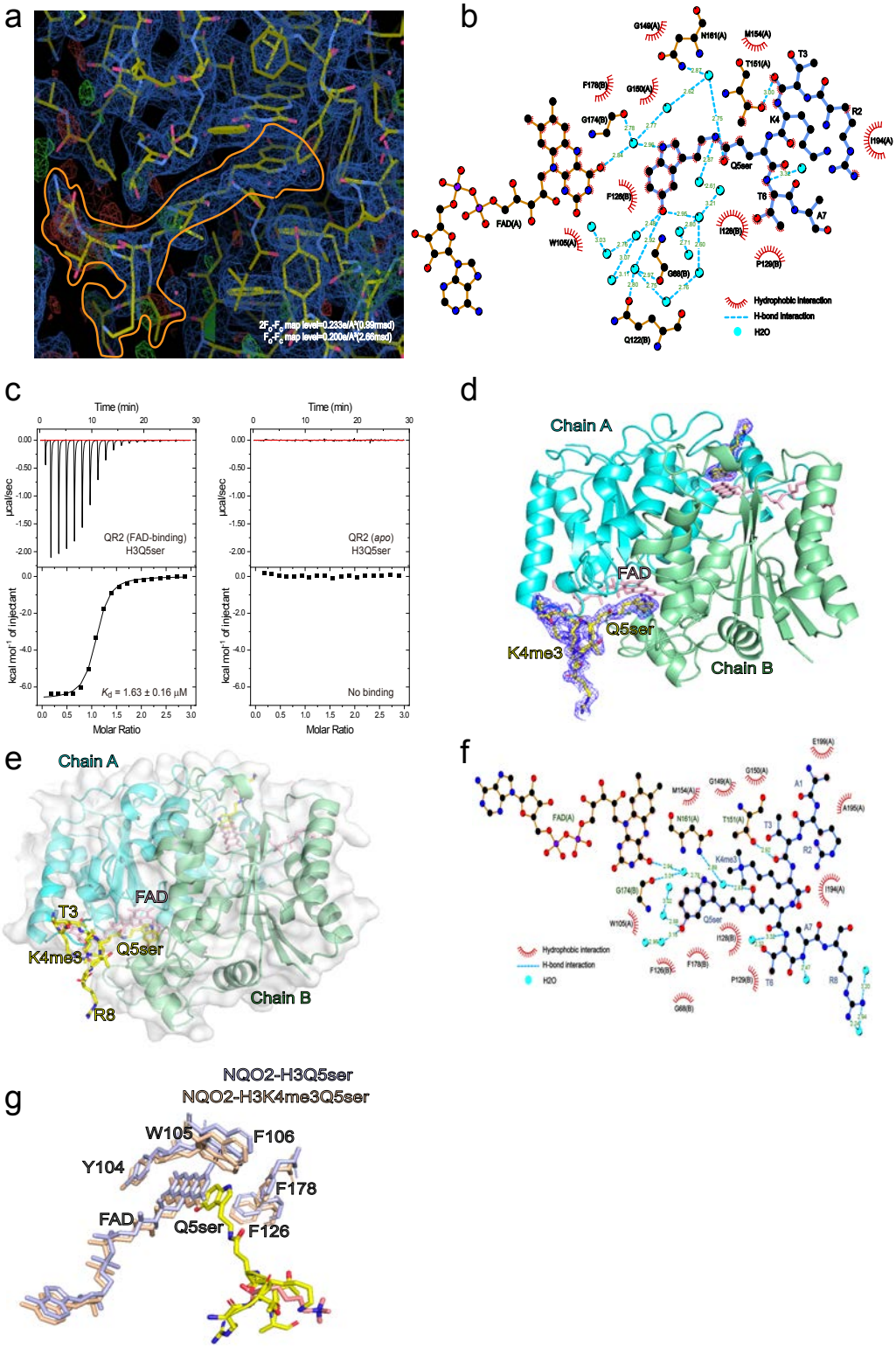
a
b
c
d
e
f
g
Time (min)
μcal/sec
kcal mol⁻¹ of injectant
QR2 (FAD-binding)
H3Q5ser
QR2 (apo)
H3Q5ser
Kd = 1.63 ± 0.16 μM
No binding
Molar Ratio
Chain A
Chain B
FAD
Q5ser
K4me3
T3
R8
Hydrophobic interaction
H-bond interaction
H2O
NQO2-H3Q5ser
NQO2-H3K4me3Q5ser
W105
F106
Y104
F178
F126

1801 **Extended Data Figure 2. Common molecular recognition of H3Q5ser and H3K4me3Q5ser**
1802 **by QR2**
1803
1804 (**a**) Corrected difference electron density map of the QR2-H3Q5ser crystal structure. The
1805 continuous density marked by the orange line corresponds to the H3Q5ser peptide, while the
1806 remaining regions represent the density of QR2. The electron density from the H3R2 to the H3A7
1807 is visible. (**b**) LIGPLOT diagram listing critical contacts between the H3Q5ser peptide and QR2.
1808 The main chain of the peptide is shown in blue, surrounded by multiple hydrophobic interactions
1809 (red arcs) and several pairs of hydrogen bond interactions (blue lines). The distances of the
1810 hydrogen bond interactions are labeled in green text. Water molecules are indicated by cyan balls,
1811 and the FAD molecule is also displayed in the diagram. The letters A and B following the amino
1812 acid residues denote Chain A and Chain B in the QR2 dimer, respectively. Numbering of residues
1813 excludes the initiating methionine of QR2. (**c**) Titration and fitting curves of peptides titrated into
1814 wildtype and *apo* (depleted of FAD) QR2. K_D values are provided. See **Extended Data Table 1**
1815 for ITC statistics. (**d**) Structure of the QR2-H3K4me3Q5ser complex. The blue mesh shows the
1816 electron density of the H3K4me3Q5ser peptide. The Q5ser residue inserts into the binding pocket
1817 of QR2, while the K4me3 residue extends out from the QR2 surface and does not participate in
1818 recognition. (**e**) The QR2-H3K4me3Q5ser co-crystal structure reveals that Q5ser inserts into the
1819 interior of the molecule, while T3 and K4me3 are oriented toward the exterior and do not
1820 participate in recognition. (**f**) LIGPLOT diagram listing critical contacts between the
1821 H3K4me3Q5ser peptide and QR2. The main chain of the peptide is shown in blue, and K4me3 is
1822 visible in the diagram. Multiple hydrophobic interactions (red arcs) surround Q5ser, which are
1823 highly consistent with those observed in the NQO2-H3Q5ser complex. Numbering of residues
1824 excludes the initiating methionine of QR2. (**g**) Comparison of the conformations of key amino
1825 acids involved in recognition between the QR2-H3K4me3Q5ser co-crystal structure (pink) and the
1826 QR2-H3Q5ser co-crystal structure (purple). Their conformations are completely identical. The
1827 unmodified K4 is shown in yellow, while the K4me3 modification is shown in red. See **Extended**
1828 **Data Table 2** for x-ray crystallography data collection and refinement statistics.
1829

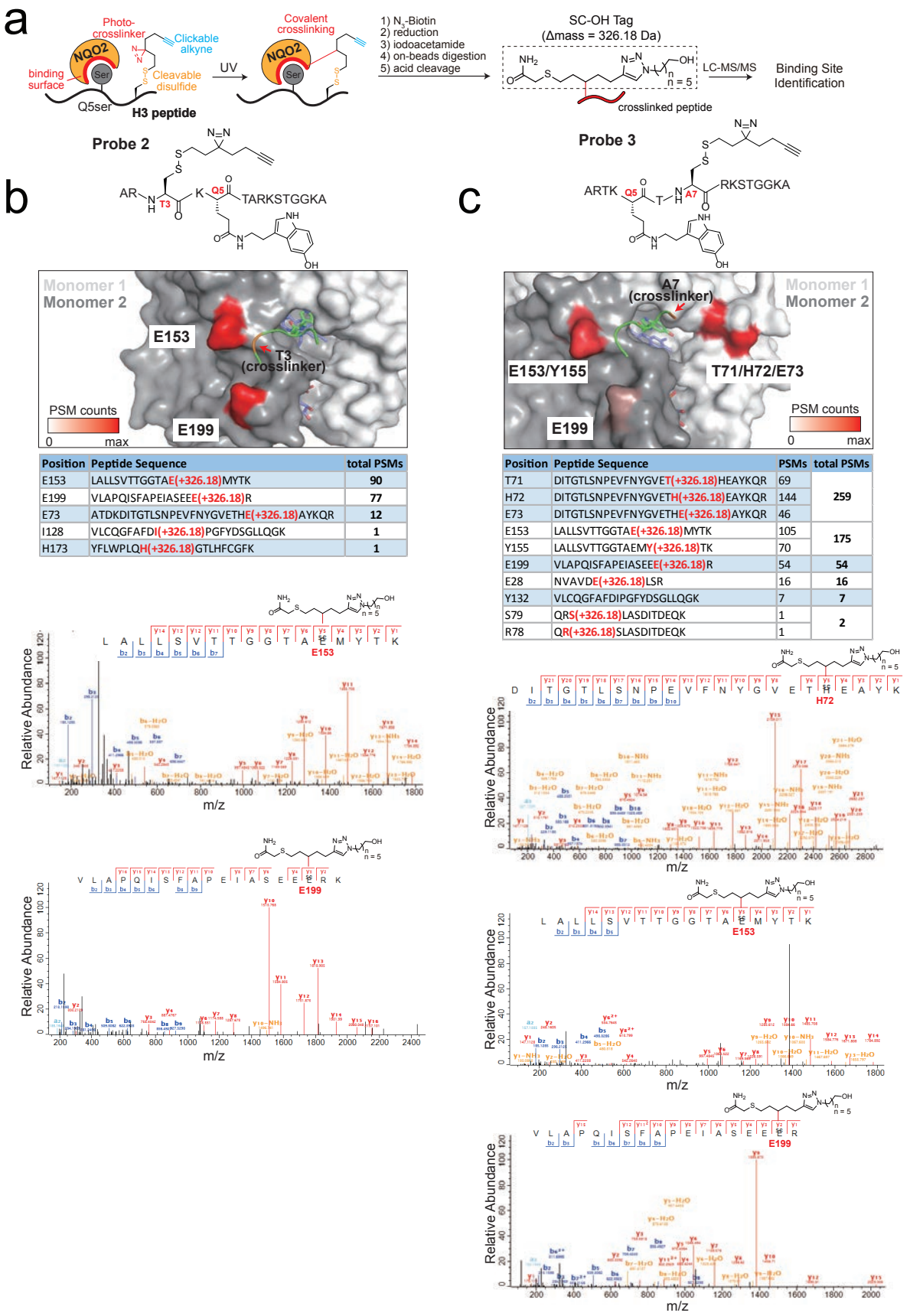

Position	Peptide Sequence	total PSMs
E153	LALLSVTTGGTAE(+326.18)MYTK	90
E199	VLAPQISFAPEIASEEE(+326.18)R	77
E73	ATDKDITGTLSNPEVFNYGVETHE(+326.18)AYKQR	12
I128	VLCQGFAFDI(+326.18)PGFYDSGLLQGK	1
H173	YFLWPLQH(+326.18)GTLHFCGFK	1

Position	Peptide Sequence	PSMs	total PSMs
T71	DITGTLSNPEVFNYGVET(+326.18)HEAYKQR	69	259
H72	DITGTLSNPEVFNYGVETH(+326.18)EAYKQR	144	
E73	DITGTLSNPEVFNYGVETHE(+326.18)AYKQR	46	
E153	LALLSVTTGGTAE(+326.18)MYTK	105	175
Y155	LALLSVTTGGTAEMY(+326.18)TK	70	
E199	VLAPQISFAPEIASEEE(+326.18)R	54	54
E28	NVAVDE(+326.18)LSR	16	16
Y132	VLCQGFAFDIPGFYDSGLLQGK	7	7
S79	QRS(+326.18)LASDITDEQK	1	2
R78	QR(+326.18)SLASDITDEQK	1	

Extended Data Figure 3. Photoaffinity probe-based mapping of the binding sites between QR2 and the H3Q5ser peptide

(**a**) Schematic workflow for binding sites mapping between recombinant QR2 and H3Q5ser peptide. QR2 was incubated with photoaffinity probes carrying serotonylation at Q5 and a tri-functional amino acid ADdis-Cys that contains a diazirine, an alkyne, and a reductively cleavable disulfide bond. Following photo-crosslinking, proteins captured by the probe will be conjugated with biotin-azide carrying an acid-labile dialkoxydiphenylsilane (DADPS) linker and then immobilized by streptavidincoated beads. After reductive cleavage, iodoacetamide-mediated thiol capping, on-bead digestion, and washing steps, the peptides remaining on the beads should be those directly cross-linked to ADdis-Cys with binding sites information. A final acid treatment released the peptides with SC-OH tags (+326.18 Da) installed at the cross-linked residues that will be identifiable by LC–MS/MS analysis. (**b**) Crosslinking sites identified with probe 2 (ADdis-Cys incorporated at T3). Upper: chemical structure of probe 2. Middle: QR2 surface representation highlighting major crosslinked residues (E153, E199) color-coded by peptide–spectrum match (PSM) counts. Lower: summary table listing crosslinked positions, corresponding peptide sequences, and total PSMs; representative MS/MS spectra for E153 and E199 with annotated b- and y-type ions and marked modification sites. (**c**) Crosslinking sites identified with probe 3 (ADdis-Cys incorporated at A7). Upper: chemical structure of Probe 3. Middle: QR2 surface representation highlighting major crosslinked residues (T71, H72, E73, E153, Y155, E199) color-coded by peptide–spectrum match (PSM) counts. Lower: summary table listing crosslinked positions, corresponding peptide sequences, and total PSMs; representative MS/MS spectra for for T71/H72/E73, E153, and E199 with annotated b- and y-type ions and marked modification sites.

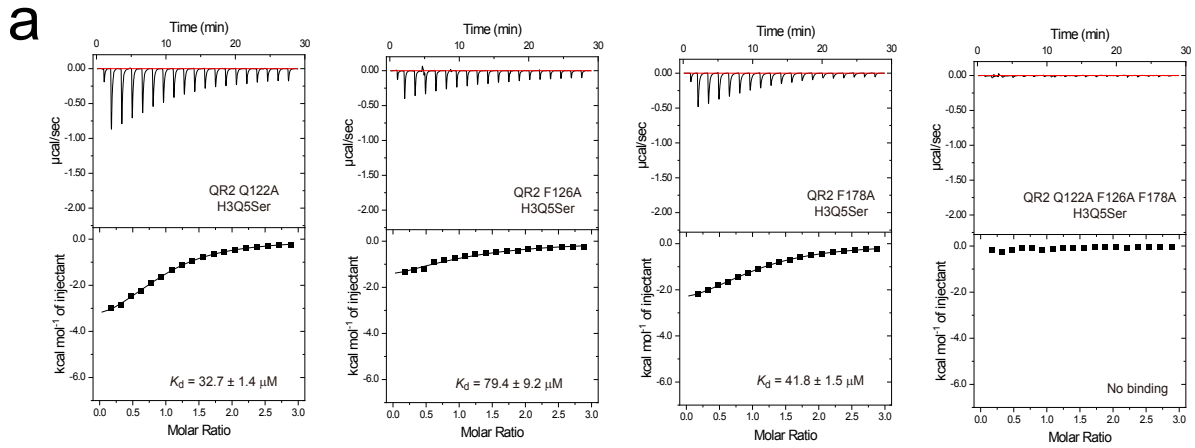

Extended Data Figure 4. Mutational ITC validations of QR2's molecular recognition of H3Q5ser

(**a**) Titration and fitting curves of peptides titrated into mutant QR2. K_D values are provided. See **Extended Data Table 1** for ITC statistics.

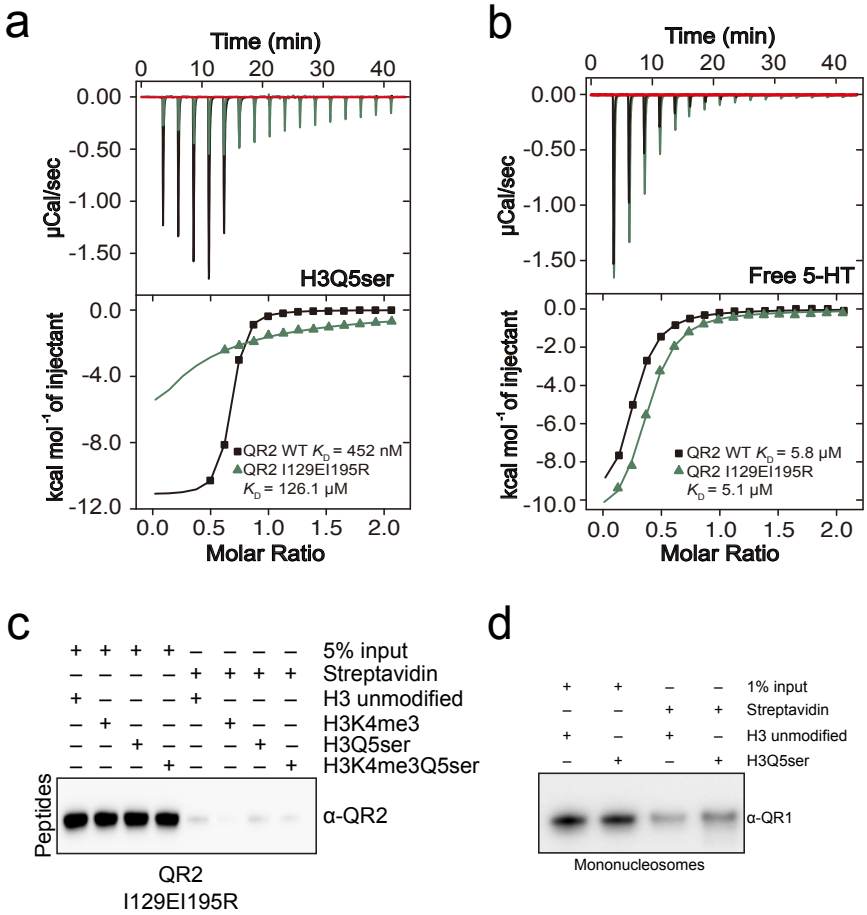

Extended Data Figure 5. Validations of disruption of H3(K4me3)Q5ser recognition by QR2 I129EI195R mutations

(**a**) Titration and fitting curves of H3Q5ser peptides titrated into QR2 WT *vs.* mutant. K_D values are provided. The mutants I129EI195R disrupts the recognition of QR2 to H3Q5ser peptides; (**b**) however, these mutations do not impact QR2's binding to free 5-HT. See **Extended Data Table 1** for ITC stats. (**c**) Peptide pulldowns with mutant recombinant QR2, followed by immunoblotting for QR2. (**d**) Mononucleosome pulldown validations of a lack of binding between QR1 and H3Q5ser. All immunoblotting experiments repeated 3X. See **Supplementary Figure 1** for uncropped blots.

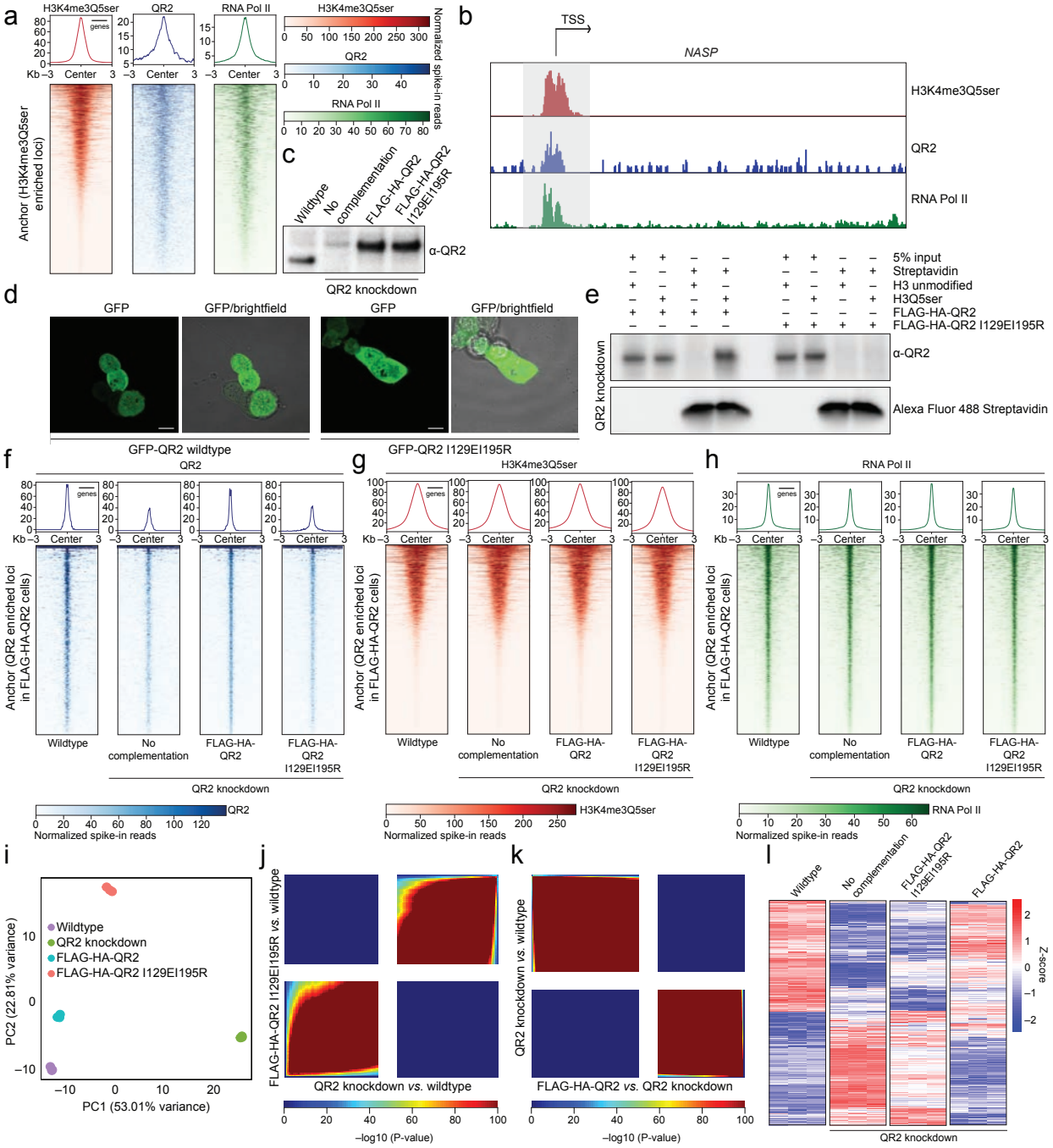

Extended Data Figure 6. QR2 and H3Q5ser genomically co-enrich in HeLa cells to regulate gene expression.

CUT&RUN-seq heatmaps of H3K4me3Q5ser, QR2, and RNA Pol II enrichment in (**a**) wildtype HeLa cells. (**b**) IGV tracks for H3K4me3Q5ser, QR2, and RNA Pol II at the *NASP* locus in wildtype HeLa cells. (**c**) Immunoblotting validation of endogenous QR2 knockdown in HeLa cells –/+ complementation with FLAG-HA-tagged wildtype *vs.* I129I195R QR2. (**d**) ICC/IF validation of QR2 subcellular localization in FLAG-HA-tagged wildtype *vs.* I129I195R QR2 complementation HeLa cells (*NQO2* knockdown background). Scale = 10 µm. (**e**) $H3_{1-18}$Q5ser *vs.*

1893 $H3_{1-18}$ unmodified peptide pulldowns from FLAG-HA-tagged wildtype *vs.* I129I195R QR2
1894 complementation HeLa cells (*NQO2* knockdown background). CUT&RUN-seq heatmaps of (**f**)
1895 QR2, (**g**) H3K4me3Q5ser, and (**h**) RNA Pol II enrichment in wildtype, QR2 knockdown (no
1896 complementation), and FLAG-HA-tagged wildtype *vs.* I129I195R QR2 complementation HeLa
1897 cells (*NQO2* knockdown background). *n* = 3 for all. (**i**) RNA-seq-based PCA analysis of wildtype,
1898 QR2 knockdown (no complementation), and FLAG-HA-tagged wildtype *vs.* I129I195R QR2
1899 complementation HeLa cells (*n* = 3 for all). RRHO analyses comparing gene expression patterns
1900 (RNA-seq) between (**j**) QR2 knockdown *vs.* wildtype and I129I195R QR2 complementation HeLa
1901 cells (*NQO2* knockdown background), as well as (**k**) QR2 knockdown *vs.* wildtype and QR2
1902 wildtype complementation HeLa cells (*NQO2* knockdown background). (**l**) Heatmap of DEGs
1903 identified in QR2 knockdown *vs.* wildtype HeLa cells (anchor) across all four HeLa cell lines. All
1904 immunoblotting experiments repeated 3X. See **Supplementary Figure 1** for uncropped blots.
1905
1906
1907
1908
1909
1910
1911
1912
1913
1914
1915
1916
1917
1918
1919
1920
1921
1922
1923
1924
1925
1926
1927
1928
1929

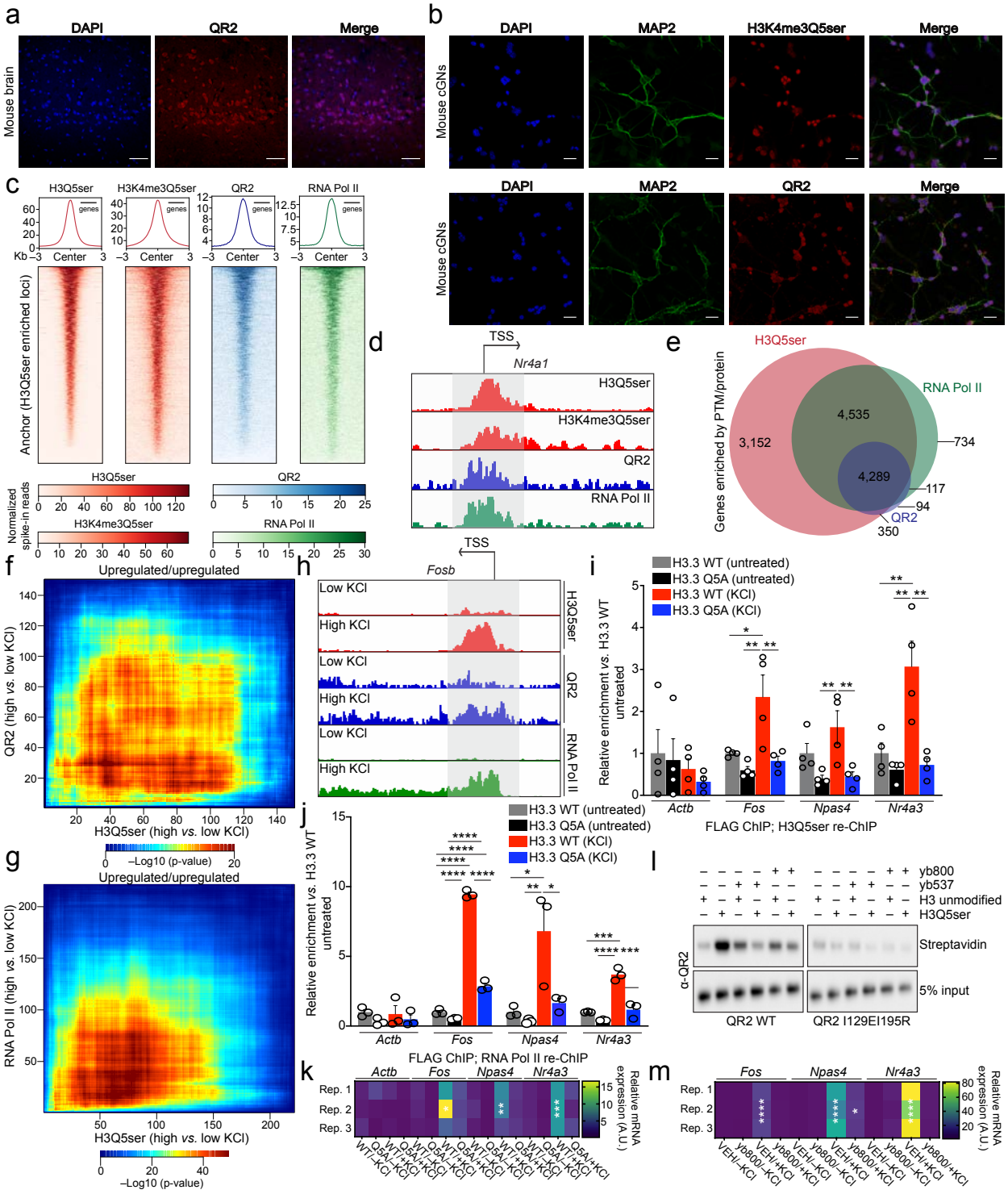

Extended Data Figure 7. QR2 and H3Q5ser genomically co-enrich in rodent neurons and correlate with genes involved in synaptic plasticity.

(**a**) IHC/IF validation of QR2 subcellular localization in wildtype mouse brain. Scale = 50 µm. (**b**) ICC/IF validation of QR2 subcellular localization in wildtype mouse cGNs. Scale = 20 µm. ChIP-

seq heatmaps of H3(K4me3)Q5ser, QR2, and RNA Pol II enrichment in (**c**) wildtype mouse cGNs. (**d**) IGV tracks for H3Q5ser, QR2, and RNA Pol II at the *Nr4a1* locus in wildtype mouse cGNs. (**e**) Venn diagram of gene displaying overlapping enrichment for H3Q5ser, QR2, and RNA Pol II in wildtype mouse cGNs. RRHO analyses comparing (**f**) H3Q5ser enrichment in wildtype mouse cGNs –/+ KCl *vs.* QR2 enrichment in wildtype mouse cGNs –/+ KCl, and (**g**) H3Q5ser enrichment in wildtype mouse cGNs –/+ KCl *vs.* RNA Pol II enrichment in wildtype mouse cGNs –/+ KCl. (**h**) IGV tracks for H3Q5ser, QR2, and RNA Pol II at the *Fosb* locus in wildtype mouse cGNs –/+ KCl. (**i**) FLAG ChIP-/H3Q5ser re-ChIP-qPCRs following transduction of wildtype mouse cGNs –/+ KCl with H3.3 WT-FLAG *vs.* H3.3Q5A-FLAG vectors (n = 4; Two-way ANOVA, P<0.05 for effect of KCl, virus, or KCl x virus; post hoc Tukey's MC tests – ** P<0.01, * P<0.05). (**j**) FLAG ChIP-/RNA Pol II re-ChIP-qPCRs following transduction of wildtype mouse cGNs –/+ KCl with H3.3 WT-FLAG *vs.* H3.3Q5A-FLAG vectors (n = 3; Two-way ANOVA, P<0.05 for effect of KCl, virus, or KCl x virus; post hoc Tukey's MC tests – **** P<0.0001, *** P<0.001, ** P<0.01, * P<0.05). (**k**) qPCRs following transduction of wildtype mouse cGNs –/+ KCl with H3.3 WT-FLAG *vs.* H3.3Q5A-FLAG vectors [n = 3; Two-way ANOVA, P<0.05 for effect of KCl, virus, or KCl x virus; post hoc Dunnett's MC tests (compared to –KCl H3.3 WT) – *** P<0.001, ** P<0.01). (**l**) $H3_{1-18}$Q5ser *vs.* $H3_{1-18}$ unmodified peptide pulldowns against recombinant QR2 in the presence or absence of QR2 inhibitors yb800 and yb537. (**m**) qPCRs following treatment of wildtype mouse cGNs –/+ KCl with vehicle *vs.* the QR2i yb800 [n = 3; Two-way ANOVA, P<0.05 for effect of KCl, QR2i, or KCl x QR2i; post hoc Uncorrected Fisher's LSD (compared to –KCl vehicle) – **** P<0.0001, * P<0.05). Data shown as mean ± SEM. All immunoblotting experiments repeated 3X. See **Supplementary Figure 1** for uncropped blots.

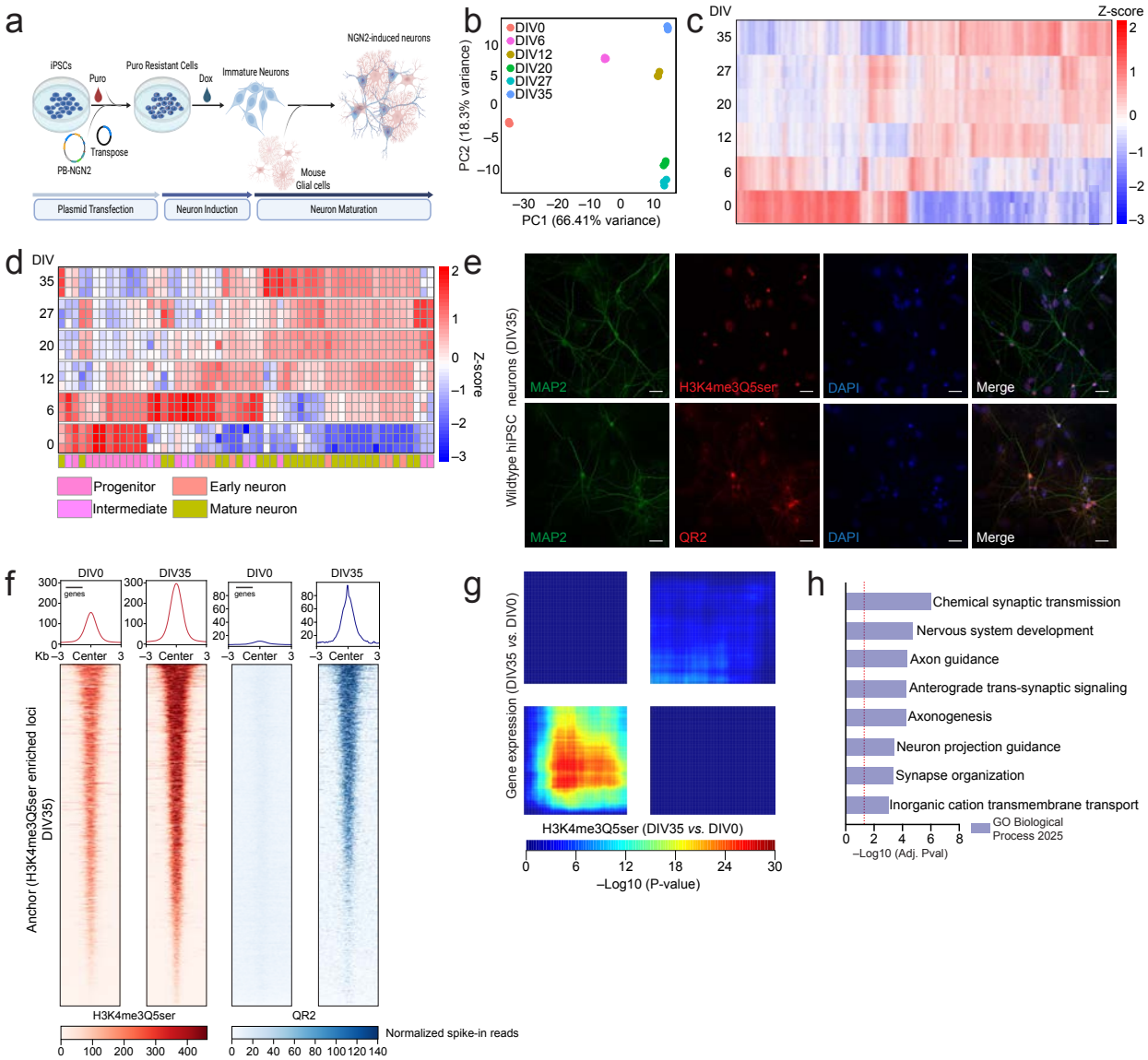

Extended Data Figure 8. QR2-H3Q5ser dynamics in response to human neuronal differentiation and maturation

(**a**) Cartoon of NGN2-mediated induction of hiPSC neurons (images generated using Biorender). (**b**) RNA-seq-based PCA analysis of hiPSC neurons during differentiation and maturation from DIV0 to DIV 35. $n = 3$ for all. (**c**) Heatmaps comparing differential gene expression (anchor DIV35 *vs.* DIV0) across hiPSC neuronal differentiation and maturation. (**d**) Heatmaps comparing differential expression of marker genes (columns) for neural progenitors, early neurons, intermediate neurons, and fully matured neurons (anchor DIV35 *vs.* DIV0) across hiPSC neuronal differentiation and maturation. (**e**) ICC/IF validation of QR2 subcellular localization in wildtype hiPSC neurons at DIV35. Scale = 50 µm. (**f**) CUT&RUN-seq heatmaps of H3K4me3Q5ser and QR2 enrichment in hiPSC neurons at DIV0 *vs.* DIV35. $n = 3$ for all. (**g**) RRHO analysis comparing DEGs at DIV35 *vs.* DIV0 to H3K4me3Q5ser enrichment at DIV35 *vs.* DIV0 in hiPSC neurons.

(**h**) Go Biological Process 2025 enrichment for genes displaying concordant induction of H3K4me3Q5ser and gene expression across hiPSC neuronal differentiation (FDR<0.05).

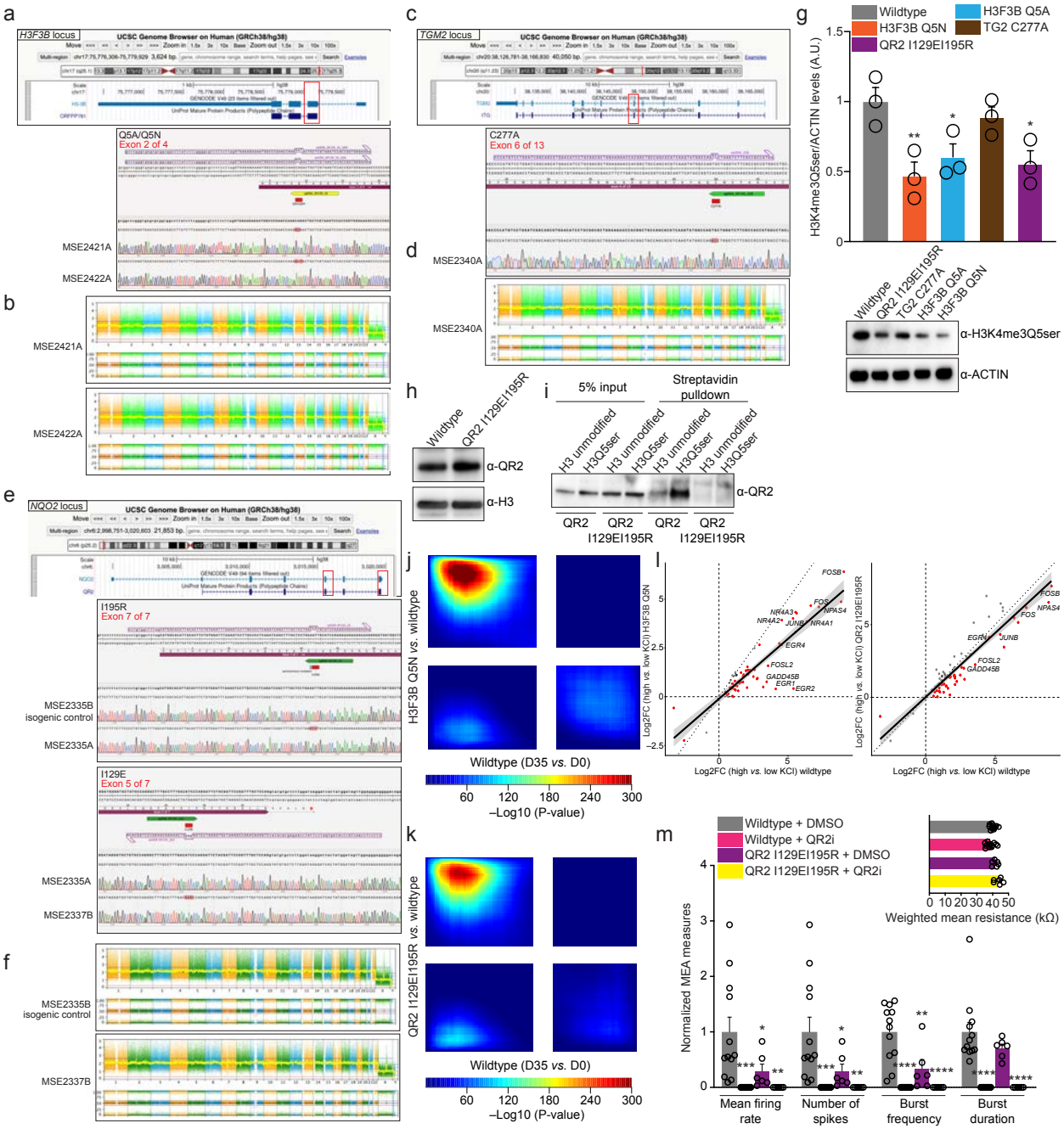

Extended Data Figure 9. Generation and validation of mutant hiPSC lines

(**a**) Overview of the *H3F3B* genomic locus and Sanger sequencing confirming precise introduction of the Q5A and Q5N missense substitutions. Sequences of the sgRNA and the ssODN used to mediate homology-directed repair (HDR) are shown. Traces from the edited lines (MSE2421A and MSE2422A) are shown together with their isogenic controls, with edited nucleotides highlighted. (**b**) Whole-genome copy-number and allele-frequency plots indicating that both knock-in lines (MSE2421A and MSE2422A) maintain normal karyotypic profiles following genome engineering. (**c**) Overview of the *TGM2* genomic locus and Sanger sequencing confirming

precise introduction of the C277A missense substitution in MSE2340A. The edited nucleotide is highlighted within the exon 6 sequence. (**d**) Whole-genome copy-number and allele-frequency plots indicating that the knock-in line (MSE2340A) maintains a normal karyotypic profile following genome engineering. (**e**) Overview of the *NQO2* genomic locus and Sanger sequencing confirming precise introduction of the I195R and I129E missense substitutions. Traces from edited lines are shown together with their isogenic controls, with edited nucleotides highlighted. (**f**) Whole-genome copy-number and allele-frequency plots indicating that both the knock-in line (MSE2337B) and its control maintain normal karyotypic profiles following genome engineering. (**g**) Immunoblotting validation of the impact of hiPSC mutations *vs.* wildtype on H3K4me3Q5ser levels in mature neurons (DIV35). n = 3/line. One-way ANOVA ($F_{4,10}$ = 6.145, p=0.0092); post hoc Dunnett's MC test – H3F3B Q5N (**P=0.0074), H3F3B Q5A (*P=0.0393), and QR2 I129EI195R (*P=0.0220). ACTIN was used as a loading control. (**h**) Immunoblotting validation that the QR2 I129EI195R mutations do not impact QR2 expression. (**i**) $H3_{1\text{-}18}$Q5ser *vs.* $H3_{1\text{-}18}$ unmodified peptide pulldowns from wildtype *vs.* QR2 I129EI195R hiPSC neurons at DIV35. RRHO analyses (RNA-seq) comparing the transcriptional impact of (**j**) H3F3B Q5N or (**k**) QR2 I129EI195R mutations in hiPSC neurons to normal patterns of gene expression during neuronal maturation from DIV0 to DIV35. (**l**) Plots of activity-dependent (KCl-induced) gene expression in wildtype hiPSC neurons (dashed line) *vs.* activity-dependent (KCl-induced) gene expression in H3F3B Q5N or QR2 I129EI195R lines, indicating attenuated responses in the mutants. (**m**) MEA-based quantification of: normalized mean firing rate [two-way ANOVA, main effect of QR2i: $F_{1,32}$ = 10.79, P=0.0025; Dunnett's MC test – *** P<0.001, ** P<0.01, * P<0.05]; normalized spike number [two-way ANOVA, main effect of QR2i: $F_{1,32}$ = 10.79, P=0.0025; post hoc: Dunnett's MC test – *** P<0.001, ** P<0.01, * P<0.05]; normalized burst frequency [two-way ANOVA, main effects of QR2i ($F_{1,32}$ = 31.01, P<0.0001), mutation ($F_{1,32}$ = 7.615, P=0.0095) and QR2i x mutation ($F_{1,32}$ = 7.615, P=0.0095); post hoc: Dunnett's MC test – **** P<0.0001, ** P<0.01]; and normalized burst duration [two-way ANOVA, main effect of QR2i: $F_{1,32}$ = 46.96, P<0.0001; post hoc: Dunnett's MC test – **** P<0.0001] in hiPSC wildtype (n = 12) or QR2 I129EI195R (n = 6) neurons –/+ the QR2i yb800. Inset: weighted mean resistance for each condition indicating no impact of genotype/treatment on neuronal viability.

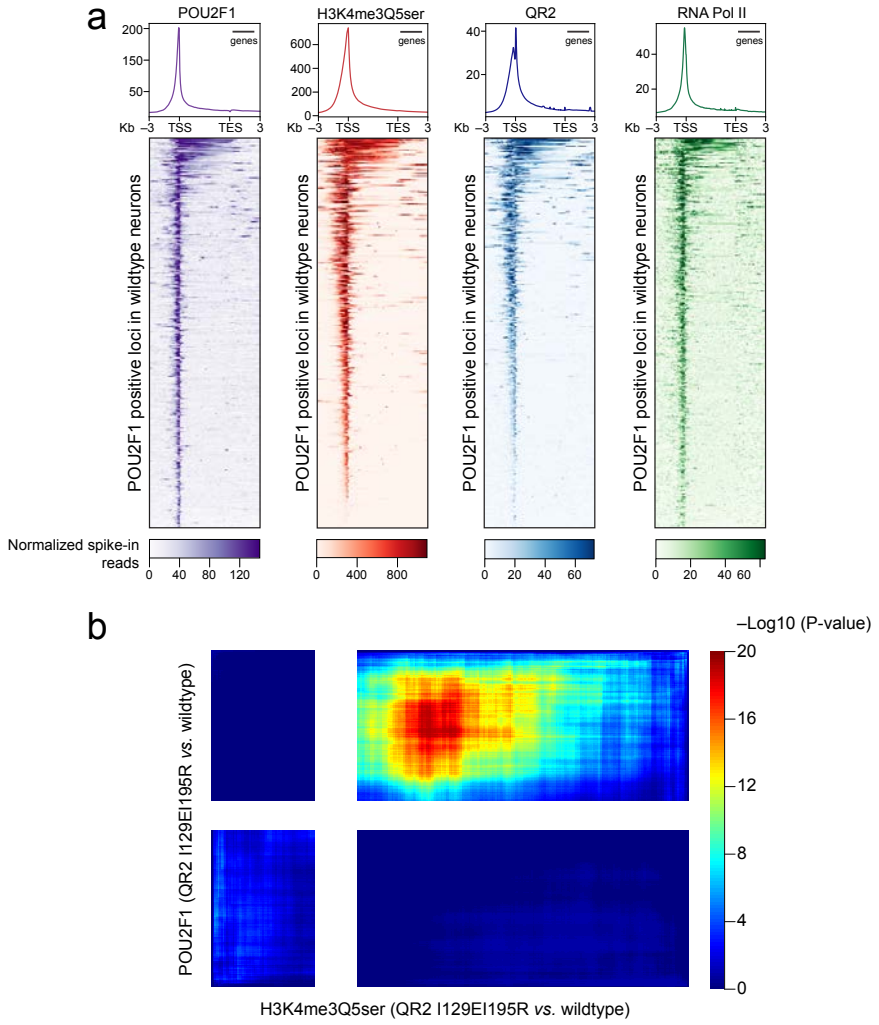

Extended Data Figure 10. POU2F1 co-enriches with H3K4me3Q5ser and QR2 in hiPSC neurons

(**a**) CUT&RUN-seq heatmaps of POU2F1, H3K4me3Q5ser, QR2, and RNA Pol II enrichment (anchored on POU2F1 enriched genes) in wildtype hiPSC neurons at DIV35. $n = 3$ for all. (**b**) RRHO analyses (CUT&RUN-seq) comparing the impact of QR2 I129EI195R mutations on POU2F1 *vs.* H3K4me3Q5ser enrichment.

SUPPLEMENTARY MATERIALS

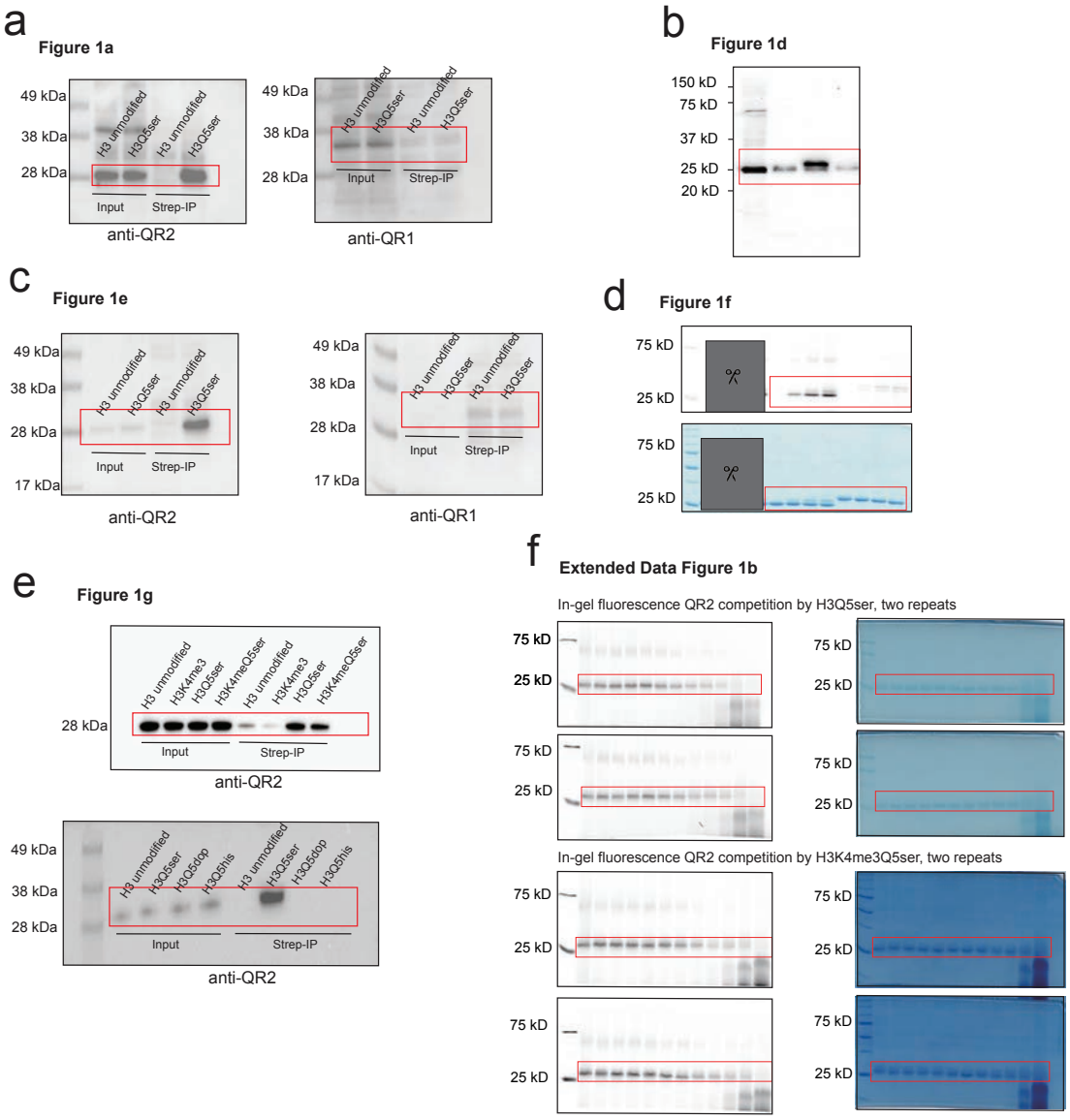

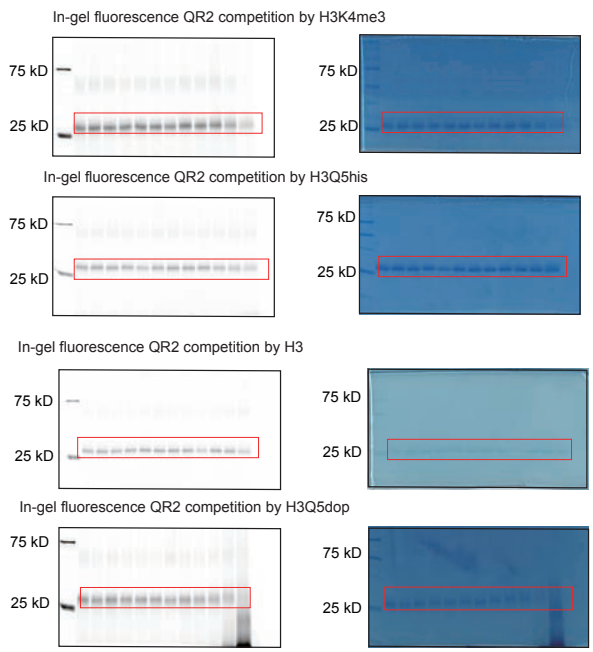
In-gel fluorescence QR2 competition by H3K4me3
75 kD
25 kD
75 kD
25 kD
In-gel fluorescence QR2 competition by H3Q5his
75 kD
25 kD
75 kD
25 kD
In-gel fluorescence QR2 competition by H3
75 kD
25 kD
75 kD
25 kD
In-gel fluorescence QR2 competition by H3Q5dop
75 kD
25 kD
75 kD
25 kD

g

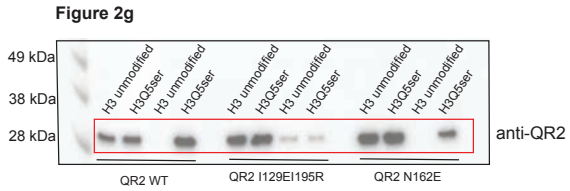
Figure 2g
49 kDa
38 kDa
28 kDa
H3 unmodified
H3Q5ser
H3 unmodified
H3Q5ser
H3 unmodified
H3Q5ser
H3 unmodified
H3Q5ser
H3 unmodified
H3Q5ser
H3 unmodified
H3Q5ser
anti-QR2
QR2 WT
QR2 I129EI195R
QR2 N162E

h

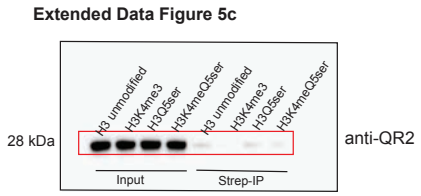
Extended Data Figure 5c
28 kDa
H3 unmodified
H3K4me3
H3Q5ser
H3K4meQ5ser
H3 unmodified
H3K4me3
H3Q5ser
H3K4meQ5ser
anti-QR2
Input
Strep-IP

i

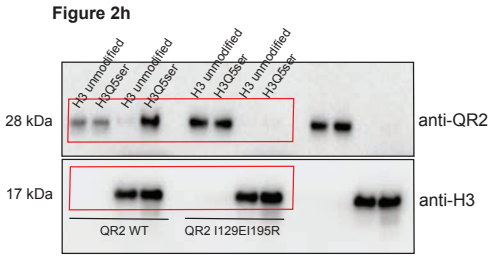
Figure 2h
H3 unmodified
H3Q5ser
H3 unmodified
H3Q5ser
H3 unmodified
H3Q5ser
H3 unmodified
H3Q5ser
28 kDa
anti-QR2
17 kDa
anti-H3
QR2 WT
QR2 I129EI195R

j

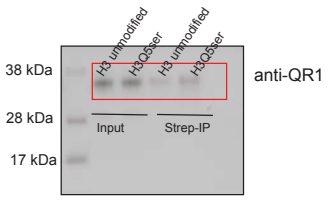
Extended Data Figure 5d
H3 unmodified
H3Q5ser
H3 unmodified
H3Q5ser
38 kDa
anti-QR1
28 kDa
Input
Strep-IP
17 kDa

2054

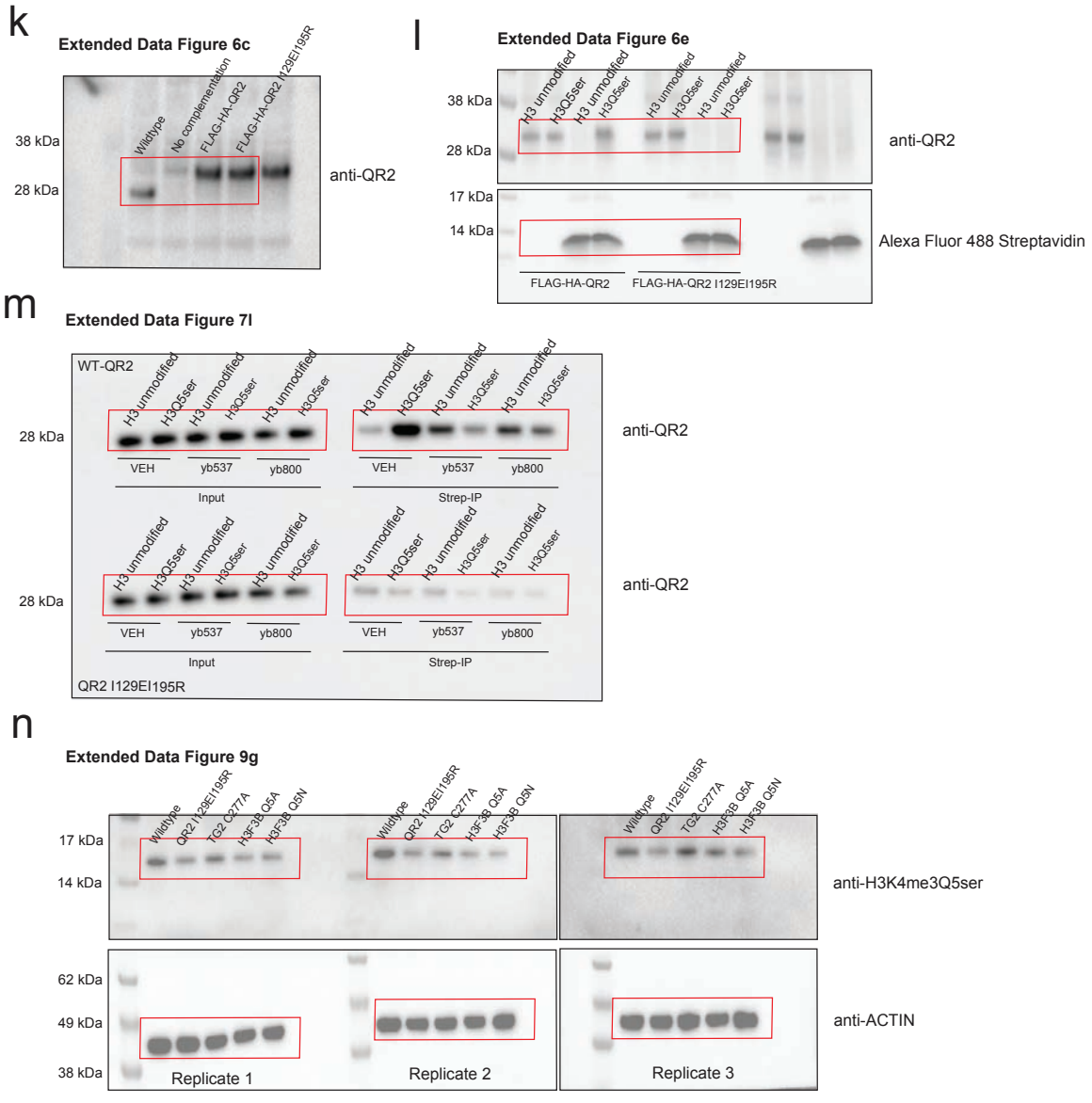
k
Extended Data Figure 6c
Wildtype
No complementation
FLAG-HA-QR2
FLAG-HA-QR2 I129EI195R
38 kDa
28 kDa
anti-QR2
l
Extended Data Figure 6e
H3 unmodified
H3Q5ser
38 kDa
28 kDa
anti-QR2
17 kDa
14 kDa
Alexa Fluor 488 Streptavidin
FLAG-HA-QR2
FLAG-HA-QR2 I129EI195R
m
Extended Data Figure 7l
WT-QR2
28 kDa
VEH
yb537
yb800
Input
Strep-IP
anti-QR2
QR2 I129EI195R
n
Extended Data Figure 9g
Wildtype
QR2 I129EI195R
TG2 C277A
H3F3B Q5A
H3F3B Q5N
17 kDa
14 kDa
anti-H3K4me3Q5ser
62 kDa
49 kDa
38 kDa
anti-ACTIN
Replicate 1
Replicate 2
Replicate 3

2055
2056

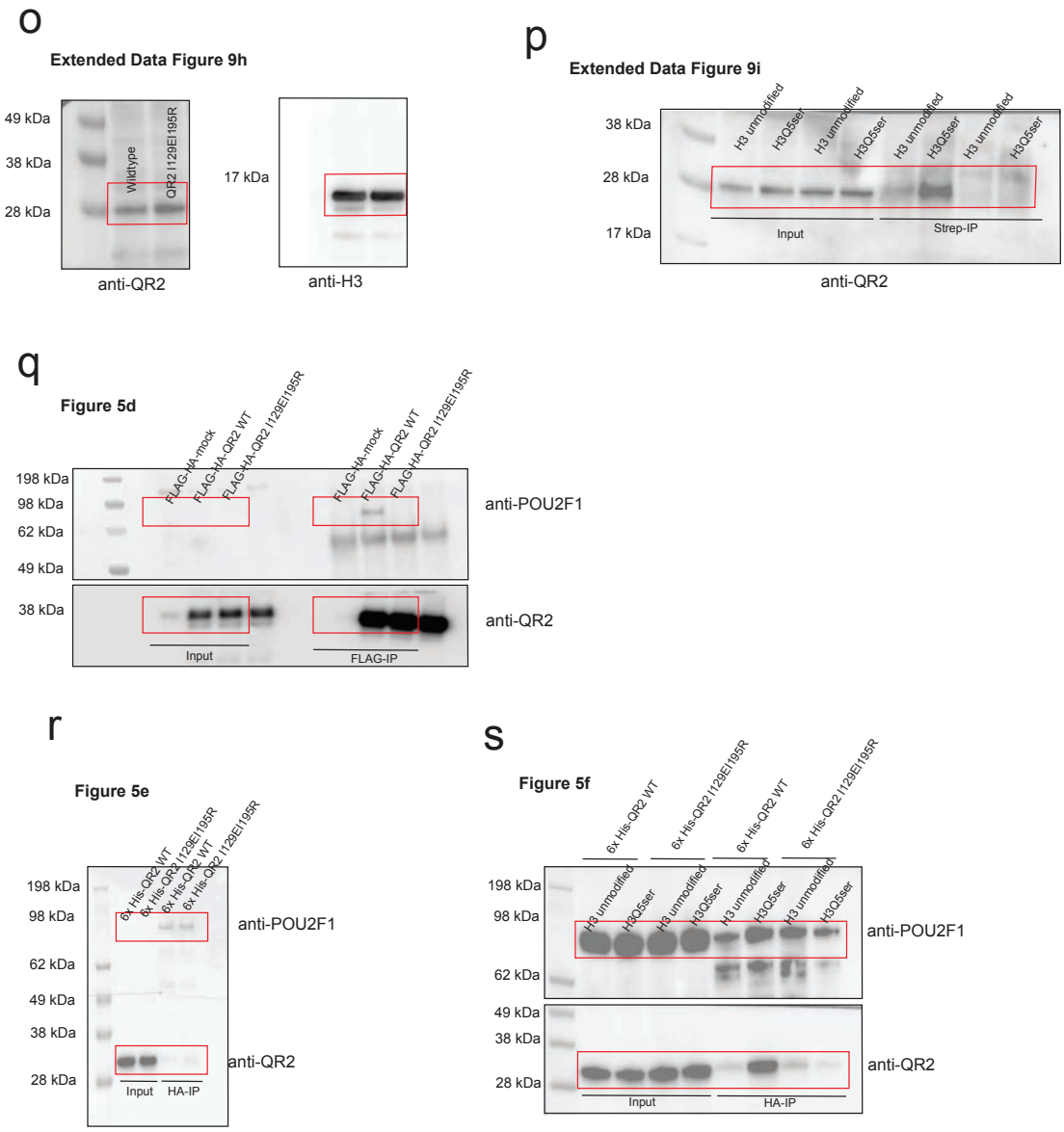

Supplementary Figure 1: Uncropped immunoblots

Uncropped immunoblots related to (**a**) Fig. 1a, (**b**) Fig. 1d, (**c**) Fig. 1e, (**d**) Fig. 1f, (**e**) Fig. 1g, (**f**) Extended Data Fig. 1b, (**g**) Fig. 2g, (**h**) Extended Data Fig. 5c, (**i**) Fig. 2h, (**j**) Extended Data Fig. 5d, (**k**) Extended Data Fig. 6c, (**l**) Extended Data Fig. 6e, (**m**) Extended Data Fig. 7l, (**n**) Extended Data Fig. 9g, (**o**) Extended Data Fig. 9h, (**p**) Extended Data Fig. 9i, (**q**) Fig. 5d, (**r**) Fig. 5e, and (**s**) Fig. 5f.

Supplementary Data 1: LC-MS/MS analysis from HeLa cell NEs.

Supplementary Data 2: LC-MS/MS analysis from SK-N-SH cell lysates.

Supplementary Data 3: CUT&RUN-seq from wildtype HeLa cells (H3K4me3Q5ser, QR2, RNA Pol II)

Supplementary Data 4: CUT&RUN-seq from wildtype *vs.* complementation HeLa cells (H3K4me3Q5ser, QR2, RNA Pol II)

Supplementary Data 5: RNA-seq from wildtype *vs.* complementation HeLa cells

Supplementary Data 6: ChIP-seq from mouse cGNs -/+ KCl (H3K4me3Q5ser, H3Q5ser, QR2, RNA PolII)

Supplementary Data 7: RNA-seq from hiPSC neurons (time course)

Supplementary Data 8: CUT&RUN-seq from hiPSC neurons (DIV0/DIV35; H3K4me3Q5ser, QR2)

Supplementary Data 9: Gene ontologies related to Extended Data Figure 8h

Supplementary Data 10: CUT&RUN-seq from wildtype *vs.* mutant hiPSC neurons (H3K4me3Q5ser, QR2, RNA Pol II)

Supplementary Data 11: RNA-seq from wildtype *vs.* mutant hiPSC neurons

Supplementary Data 12: 1,193 Overlapping genes displaying regulation in mutant *vs.* wildtype hiPSC neurons

Supplementary Data 13: Gene ontologies related to Fig. 2n

Supplementary Data 14: LC-MS/MS analysis from HeLa NEs (FLAG-HA-tagged QR2 wildtype *vs.* Flag-HA mock; FLAG-HA-tagged QR2 I129EI195R *vs.* FLAG-HA-tagged QR2 wildtype)

Supplementary Data 15: CUT&RUN-seq from wildtype *vs.* mutant hiPSC neurons (POU2F1)

Supplementary Data 16: ATAC-seq from wildtype *vs.* mutant hiPSC neurons

Supplementary Data 17: Gene ontologies related to Fig. 4j

Supplementary Data 18: Sequences of sgRNAs, ssODN donor templates, and PCR primers used for CRISPR–Cas9–mediated HDR

References

1 Farrelly, L. A. *et al.* Histone serotonylation is a permissive modification that enhances TFIID binding to H3K4me3. *Nature* **567**, 535-539 (2019). https://doi.org:10.1038/s41586-019-1024-7

2 Al-Kachak, A. & Maze, I. Post-translational modifications of histone proteins by monoamine neurotransmitters. *Current Opinion in Chemical Biology* **74**, 102302 (2023). https://doi.org:10.1016/j.cbpa.2023.102302

3 Vinson, D. A. & Maze, I. Reimagining biogenic amine signaling in the brain and beyond. *Trends Neurosci* **49**, 35-48 (2026). https://doi.org:10.1016/j.tins.2025.11.003

4 Weekley, B. H., Ahmed, N. I. & Maze, I. Elucidating neuroepigenetic mechanisms to inform targeted therapeutics for brain disorders. *iScience* **28**, 112092 (2025). https://doi.org:10.1016/j.isci.2025.112092

5 Chan, J. C. & Maze, I. Nothing Is Yet Set in (Hi)stone: Novel Post-Translational Modifications Regulating Chromatin Function. *Trends Biochem Sci* **45**, 829-844 (2020). https://doi.org:10.1016/j.tibs.2020.05.009

6 Sardar, D. *et al.* Induction of astrocytic Slc22a3 regulates sensory processing through histone serotonylation. *Science* **380**, eade0027 (2023). https://doi.org:10.1126/science.ade0027

7 Zheng, Q. *et al.* Bidirectional histone monoaminylation dynamics regulate neural rhythmicity. *Nature* **637**, 974-982 (2025). https://doi.org:10.1038/s41586-024-08371-3

8 Al-Kachak, A. *et al.* Histone serotonylation in dorsal raphe nucleus contributes to stress- and antidepressant-mediated gene expression and behavior. *Nat Commun* **15**, 5042 (2024). https://doi.org:10.1038/s41467-024-49336-4

9 Chan, J. C. *et al.* Serotonin Transporter-dependent Histone Serotonylation in Placenta Contributes to the Neurodevelopmental Transcriptome. *J Mol Biol* **436**, 168454 (2024). https://doi.org:10.1016/j.jmb.2024.168454

10 Chen, H. C. *et al.* Histone serotonylation regulates ependymoma tumorigenesis. *Nature* **632**, 903-910 (2024). https://doi.org:10.1038/s41586-024-07751-z

11 Zhang, N. *et al.* Bioorthogonal Labeling and Enrichment of Histone Monoaminylation Reveal Its Accumulation and Regulatory Function in Cancer Cell Chromatin. *J Am Chem Soc* (2024). https://doi.org:10.1021/jacs.4c04249

12 Ling, T. *et al.* Serotonylation in tumor-associated fibroblasts contributes to the tumor-promoting roles of serotonin in colorectal cancer. *Cancer Lett* **600**, 217150 (2024). https://doi.org:10.1016/j.canlet.2024.217150

13 Zhang, N. *et al.* pH-Controlled Chemoselective Rapid Azo-Coupling Reaction (CRACR) Enables Global Profiling of Serotonylation Proteome in Cancer Cells. *J Proteome Res* **23**, 4457-4466 (2024). https://doi.org:10.1021/acs.jproteome.4c00409

14 Dong, R. *et al.* TGM2-mediated histone serotonylation promotes HCC progression via MYC signalling pathway. *J Hepatol* **83**, 105-118 (2025). https://doi.org:10.1016/j.jhep.2024.12.038

15 Liu, K. *et al.* 5-HT orchestrates histone serotonylation and citrullination to drive neutrophil extracellular traps and liver metastasis. *J Clin Invest* **135** (2025). https://doi.org:10.1172/JCI183544

16 Navarro-Corcuera, A. & Martinez-Chantar, M. L. Histone serotonylation in HCC: Decoding the impact of "happy" histones on liver cancer progression. *J Hepatol* **83**, 18-20 (2025). https://doi.org:10.1016/j.jhep.2025.02.020

17 Lin, S. *et al.* Histone serotonylation promotes pancreatic cancer development via lipid metabolism remodeling. *Nat Commun* **16**, 5947 (2025). https://doi.org:10.1038/s41467-025-61197-z

18 Ji, Y. *et al.* Serotonin modulates lineage plasticity in neuroendocrine prostate cancer via epigenetic reprogramming. *Cancer Discov* (2025). https://doi.org:10.1158/2159-8290.CD-25-0974

19 Li, A. *et al.* 5-HT reuptake blockade induces pyroptosis in BRAF(V600E)-mutated melanomas via remodeling histone serotonylation. *Cell Rep Med* **7**, 102537 (2026). https://doi.org:10.1016/j.xcrm.2025.102537

20 Pulido-Cortes, L. *et al.* Molecular determinants for recognition of serotonylated chromatin. *Nucleic Acids Res* **53** (2025). https://doi.org:10.1093/nar/gkaf612

21 Zhao, S. *et al.* Histone H3Q5 serotonylation stabilizes H3K4 methylation and potentiates its readout. *Proc Natl Acad Sci U S A* **118** (2021). https://doi.org:10.1073/pnas.2016742118

22 Dincer, E., Oguz, M. & Baris, Y. Biochemical and pharmacological properties of biogenic amines. *Biogenic Amines* (2018). https://doi.org:10.5772/intechopen.81569

23 Fukumoto, T., Kema, I. P. & Levin, M. Serotonin signaling is a very early step in patterning of the left-right axis in chick and frog embryos. *Current Biology* **15**, 794-803 (2005). https://doi.org:10.1016/j.cub.2005.03.044

24 Neumann, J., Hofmann, B., Dhein, S. & Gergs, U. Cardiac roles of serotonin (5-HT) and 5-HT-receptors in health and disease. *Int J Mol Sci* **24** (2023). https://doi.org:10.3390/ijms24054765

25 Cirillo, C., Vanden Berghe, P. & Tack, J. Role of serotonin in gastrointestinal physiology and pathology. *Minerva Endocrinol* **36**, 311-324 (2011).

26 Teleanu, R. I. *et al.* Neurotransmitters-key factors in neurological and neurodegenerative disorders of the central nervous system. *Int J Mol Sci* **23** (2022). https://doi.org:10.3390/ijms23115954

27 Yang, X. *et al.* Pathophysiologic role of neurotransmitters in digestive diseases. *Front Physiol* **12**, 567650 (2021). https://doi.org:10.3389/fphys.2021.567650

28 Walther, D. J., Stahlberg, S. & Vowinckel, J. Novel roles for biogenic monoamines: from monoamines in transglutaminase-mediated post-translational protein modification to monoaminylation deregulation diseases. *FEBS J* **278**, 4740-4755 (2011). https://doi.org:10.1111/j.1742-4658.2011.08347.x

29 Walther, D. J. *et al.* Serotonylation of small GTPases is a signal transduction pathway that triggers platelet alpha-granule release. *Cell* **115**, 851-862 (2003). https://doi.org:10.1016/s0092-8674(03)01014-6

30 Lepack, A. E. *et al.* Dopaminylation of histone H3 in ventral tegmental area regulates cocaine seeking. *Science* **368**, 197-201 (2020). https://doi.org:10.1126/science.aaw8806

31 Stewart, A. F., Lepack, A. E., Fulton, S. L., Safovich, P. & Maze, I. Histone H3 dopaminylation in nucleus accumbens, but not medial prefrontal cortex, contributes to cocaine-seeking following prolonged abstinence. *Mol Cell Neurosci* **125**, 103824 (2023). https://doi.org:10.1016/j.mcn.2023.103824

32 Fulton, S. L. *et al.* Histone H3 dopaminylation in ventral tegmental area underlies heroin-induced transcriptional and behavioral plasticity in male rats. *Neuropsychopharmacology* **47**, 1776-1783 (2022). https://doi.org:10.1038/s41386-022-01279-4

33 Lukasak, B. J. *et al.* TGM2-mediated histone transglutamination is dictated by steric accessibility. *Proc Natl Acad Sci U S A* **119**, e2208672119 (2022). https://doi.org:10.1073/pnas.2208672119

34 Zhao, J. *et al.* Structural insights into the recognition of histone H3Q5 serotonylation by WDR5. *Sci Adv* **7** (2021). https://doi.org:10.1126/sciadv.abf4291

35 Vella, F., Ferry, G., Delagrange, P. & Boutin, J. A. NRH:quinone reductase 2: an enzyme of surprises and mysteries. *Biochem Pharmacol* **71**, 1-12 (2005). https://doi.org:10.1016/j.bcp.2005.09.019

36 Ferry, G. & Boutin, J. A. Measurement of NQO2 Catalytic Activity and of Its Inhibition by Melatonin. *Methods Mol Biol* **2550**, 315-321 (2022). https://doi.org:10.1007/978-1-0716-2593-4_33

37 Calamini, B., Santarsiero, B. D., Boutin, J. A. & Mesecar, A. D. Kinetic, thermodynamic and X-ray structural insights into the interaction of melatonin and analogues with quinone reductase 2. *Biochem J* **413**, 81-91 (2008). https://doi.org:10.1042/BJ20071373

38 Calamini, B., Ferry, G. & Boutin, J. A. Cloning, Expression, Purification, Crystallization, and X-Ray Structural Determination of the Human NQO2 in Complex with Melatonin. *Methods Mol Biol* **2550**, 291-304 (2022). https://doi.org:10.1007/978-1-0716-2593-4_31

39 Janda, E., Boutin, J. A., De Lorenzo, C. & Arbitrio, M. Polymorphisms and Pharmacogenomics of NQO2: The Past and the Future. *Genes (Basel)* **15** (2024). https://doi.org:10.3390/genes15010087

40 Benoit, C. E. *et al.* Loss of quinone reductase 2 function selectively facilitates learning behaviors. *J Neurosci* **30**, 12690-12700 (2010). https://doi.org:10.1523/JNEUROSCI.2808-10.2010

41 Lin, J., Bao, X. & Li, X. D. A tri-functional amino acid enables mapping of binding sites for posttranslational-modification-mediated protein-protein interactions. *Mol Cell* **81**, 2669-2681 e2669 (2021). https://doi.org:10.1016/j.molcel.2021.04.001

42 Skene, P. J. & Henikoff, S. An efficient targeted nuclease strategy for high-resolution mapping of DNA binding sites. *Elife* **6** (2017). https://doi.org:10.7554/eLife.21856

43 Maze, I. *et al.* Critical Role of Histone Turnover in Neuronal Transcription and Plasticity. *Neuron* **87**, 77-94 (2015). https://doi.org:10.1016/j.neuron.2015.06.014

44 Gould, N. L. *et al.* Specific quinone reductase 2 inhibitors reduce metabolic burden and reverse Alzheimer's disease phenotype in mice. *J Clin Invest* **133** (2023). https://doi.org:10.1172/jci162120

45 Zhang, Y. *et al.* Rapid single-step induction of functional neurons from human pluripotent stem cells. *Neuron* **78**, 785-798 (2013). https://doi.org:10.1016/j.neuron.2013.05.029

46 Kreitzer, F. R. *et al.* A robust method to derive functional neural crest cells from human pluripotent stem cells. *Am J Stem Cells* **2**, 119-131 (2013).

47 Funk, O. H., Qalieh, Y., Doyle, D. Z., Lam, M. M. & Kwan, K. Y. Postmitotic accumulation of histone variant H3.3 in new cortical neurons establishes neuronal chromatin, transcriptome, and identity. *Proc Natl Acad Sci U S A* **119**, e2116956119 (2022). https://doi.org:10.1073/pnas.2116956119

48 Domcke, S. *et al.* A human cell atlas of fetal chromatin accessibility. *Science* **370** (2020). https://doi.org:10.1126/science.aba7612

49 Kiyota, T., Kato, A., Altmann, C. R. & Kato, Y. The POU homeobox protein Oct-1 regulates radial glia formation downstream of Notch signaling. *Dev Biol* **315**, 579-592 (2008). https://doi.org:10.1016/j.ydbio.2007.12.013

50 Rada, B. & Leto, T. L. Oxidative innate immune defenses by Nox/Duox family NADPH oxidases. *Contrib Microbiol* **15**, 164-187 (2008). https://doi.org:10.1159/000136357

51 Rowe, L. A., Degtyareva, N. & Doetsch, P. W. DNA damage-induced reactive oxygen species (ROS) stress response in Saccharomyces cerevisiae. *Free Radic Biol Med* **45**, 1167-1177 (2008). https://doi.org:10.1016/j.freeradbiomed.2008.07.018

52 Shields, H. J., Traa, A. & Van Raamsdonk, J. M. Beneficial and Detrimental Effects of Reactive Oxygen Species on Lifespan: A Comprehensive Review of Comparative and Experimental Studies. *Front Cell Dev Biol* **9**, 628157 (2021). https://doi.org:10.3389/fcell.2021.628157

53 Deller, S., Macheroux, P. & Sollner, S. Flavin-dependent quinone reductases. *Cell Mol Life Sci* **65**, 141-160 (2008). https://doi.org:10.1007/s00018-007-7300-y

54 Islam, F., Leung, K. K., Walker, M. D., Al Massri, S. & Shilton, B. H. The Unusual Cosubstrate Specificity of NQO2: Conservation Throughout the Amniotes and Implications for Cellular Function. *Front Pharmacol* **13**, 838500 (2022). https://doi.org:10.3389/fphar.2022.838500

55 Gould, N. L. *et al.* Specific quinone reductase 2 inhibitors reduce metabolic burden and reverse Alzheimer's disease phenotype in mice. *J Clin Invest* **133** (2023). https://doi.org:10.1172/JCI162120

56 Islam, F., Basilone, N., Yoo, V., Ball, E. & Shilton, B. Evolutionary analysis of Quinone Reductases 1 and 2 suggests that NQO2 evolved to function as a pseudoenzyme. *Protein Sci* **33**, e5234 (2024). https://doi.org:10.1002/pro.5234

57 Brouillette, J. & Quirion, R. Transthyretin: a key gene involved in the maintenance of memory capacities during aging. *Neurobiol Aging* **29**, 1721-1732 (2008). https://doi.org:10.1016/j.neurobiolaging.2007.04.007

58 Gould, N. L., Elkobi, A., Edry, E., Daume, J. & Rosenblum, K. Muscarinic-Dependent miR-182 and QR2 Expression Regulation in the Anterior Insula Enables Novel Taste Learning. *eNeuro* **7** (2020). https://doi.org:10.1523/ENEURO.0067-20.2020

59 Hashimoto, T. & Nakai, M. Increased hippocampal quinone reductase 2 in Alzheimer's disease. *Neurosci Lett* **502**, 10-12 (2011). https://doi.org:10.1016/j.neulet.2011.07.008

60 Rappaport, A. N. *et al.* Expression of Quinone Reductase-2 in the Cortex Is a Muscarinic Acetylcholine Receptor-Dependent Memory Consolidation Constraint. *J Neurosci* **35**, 15568-15581 (2015). https://doi.org:10.1523/JNEUROSCI.1170-15.2015

61 Takeuchi, T. *et al.* Locus coeruleus and dopaminergic consolidation of everyday memory. *Nature* **537**, 357-362 (2016). https://doi.org:10.1038/nature19325

62 Cai, D. & Liu, T. Inflammatory cause of metabolic syndrome via brain stress and NF-kappaB. *Aging (Albany NY)* **4**, 98-115 (2012). https://doi.org:10.18632/aging.100431

63 Muddapu, V. R., Dharshini, S. A. P., Chakravarthy, V. S. & Gromiha, M. M. Neurodegenerative Diseases - Is Metabolic Deficiency the Root Cause? *Front Neurosci* **14**, 213 (2020). https://doi.org:10.3389/fnins.2020.00213

64 Vogel, S. & Schwabe, L. Learning and memory under stress: implications for the classroom. *NPJ Sci Learn* **1**, 16011 (2016). https://doi.org:10.1038/npjscilearn.2016.11

65 Gould, N. L. *et al.* Dopamine-Dependent QR2 Pathway Activation in CA1 Interneurons Enhances Novel Memory Formation. *J Neurosci* **40**, 8698-8714 (2020). https://doi.org:10.1523/JNEUROSCI.1243-20.2020

66 Gould, N. L., Kolatt Chandran, S., Kayyal, H., Edry, E. & Rosenblum, K. Somatostatin Interneurons of the Insula Mediate QR2-Dependent Novel Taste Memory Enhancement. *eNeuro* **8** (2021). https://doi.org:10.1523/ENEURO.0152-21.2021

67 Iskander, K. & Jaiswal, A. K. Quinone oxidoreductases in protection against myelogenous hyperplasia and benzene toxicity. *Chem Biol Interact* **153-154**, 147-157 (2005). https://doi.org:10.1016/j.cbi.2005.03.019

68 Long, D. J., 2nd *et al.* Disruption of dihydronicotinamide riboside:quinone oxidoreductase 2 (NQO2) leads to myeloid hyperplasia of bone marrow and decreased sensitivity to menadione toxicity. *J Biol Chem* **277**, 46131-46139 (2002). https://doi.org:10.1074/jbc.M208675200

69 Celli, C. M., Tran, N., Knox, R. & Jaiswal, A. K. NRH:quinone oxidoreductase 2 (NQO2) catalyzes metabolic activation of quinones and anti-tumor drugs. *Biochem Pharmacol* **72**, 366-376 (2006). https://doi.org:10.1016/j.bcp.2006.04.029

70 Tyanova, S., Temu, T. & Cox, J. The MaxQuant computational platform for mass spectrometry-based shotgun proteomics. *Nat Protoc* **11**, 2301-2319 (2016). https://doi.org:10.1038/nprot.2016.136

71 Vagin, A. & Teplyakov, A. Molecular replacement with MOLREP. *Acta Crystallogr D Biol Crystallogr* **66**, 22-25 (2010). https://doi.org:10.1107/S0907444909042589

72 Emsley, P. & Cowtan, K. Coot: model-building tools for molecular graphics. *Acta Crystallogr D Biol Crystallogr* **60**, 2126-2132 (2004). https://doi.org:10.1107/S0907444904019158

73 Adams, P. D. *et al.* PHENIX: a comprehensive Python-based system for macromolecular structure solution. *Acta Crystallogr D Biol Crystallogr* **66**, 213-221 (2010). https://doi.org:10.1107/S0907444909052925

74 Flood, D. T. *et al.* Leveraging the Knorr Pyrazole Synthesis for the Facile Generation of Thioester Surrogates for use in Native Chemical Ligation. *Angew Chem Int Ed Engl* **57**, 11634-11639 (2018). https://doi.org:10.1002/anie.201805191

75 Simon, M. D. *et al.* The site-specific installation of methyl-lysine analogs into recombinant histones. *Cell* **128**, 1003-1012 (2007). https://doi.org:10.1016/j.cell.2006.12.041

76 Bilimoria, P. M. & Bonni, A. Cultures of cerebellar granule neurons. *CSH Protoc* **2008**, pdb.prot5107 (2008). https://doi.org:10.1101/pdb.prot5107

77 Zhang, Y. *et al.* Rapid single-step induction of functional neurons from human pluripotent stem cells. *Neuron* **78**, 785-798 (2013). https://doi.org:10.1016/j.neuron.2013.05.029

78 Malik, A. N. *et al.* Genome-wide identification and characterization of functional neuronal activity-dependent enhancers. *Nat Neurosci* **17**, 1330-1339 (2014). https://doi.org:10.1038/nn.3808

79 Bray, N. L., Pimentel, H., Melsted, P. & Pachter, L. Near-optimal probabilistic RNA-seq quantification. *Nature Biotechnology* **34**, 525-527 (2016). https://doi.org:10.1038/nbt.3519

80 Love, M. I., Huber, W. & Anders, S. Moderated estimation of fold change and dispersion for RNA-seq data with DESeq2. *Genome Biol* **15**, 550 (2014). https://doi.org:10.1186/s13059-014-0550-8

81 Cahill, K. M., Huo, Z., Tseng, G. C., Logan, R. W. & Seney, M. L. Improved identification of concordant and discordant gene expression signatures using an updated rank-rank

hypergeometric overlap approach. *Scientific Reports* **8**, 9588 (2018). https://doi.org:10.1038/s41598-018-27903-2

82 Kim, D., Langmead, B. & Salzberg, S. L. HISAT: a fast spliced aligner with low memory requirements. *Nature Methods* **12**, 357-360 (2015). https://doi.org:10.1038/nmeth.3317

83 Zhang, Y. *et al.* Model-based Analysis of ChIP-Seq (MACS). *Genome Biology* **9**, R137 (2008). https://doi.org:10.1186/gb-2008-9-9-r137

84 Stark, R. & Brown, G. DiffBind: differential binding analysis of ChIP-Seq peak data. *R package version* **100**, 2-21 (2011).

85 Yu, G., Wang, L.-G. & He, Q.-Y. ChIPseeker: an R/Bioconductor package for ChIP peak annotation, comparison and visualization. *Bioinformatics* **31**, 2382-2383 (2015). https://doi.org:10.1093/bioinformatics/btv145

86 Ramírez, F., Dündar, F., Diehl, S., Grüning, B. A. & Manke, T. deepTools: a flexible platform for exploring deep-sequencing data. *Nucleic acids research* **42**, W187-W191 (2014).

87 Skene, P. J., Henikoff, J. G. & Henikoff, S. Targeted in situ genome-wide profiling with high efficiency for low cell numbers. *Nat Protoc* **13**, 1006-1019 (2018). https://doi.org:10.1038/nprot.2018.015

88 Meers, M. P., Bryson, T. D., Henikoff, J. G. & Henikoff, S. Improved CUT&RUN chromatin profiling tools. *Elife* **8** (2019). https://doi.org:10.7554/eLife.46314

89 Langmead, B. & Salzberg, S. L. Fast gapped-read alignment with Bowtie 2. *Nat Methods* **9**, 357-359 (2012). https://doi.org:10.1038/nmeth.1923

90 Li, H. *et al.* The Sequence Alignment/Map format and SAMtools. *Bioinformatics* **25**, 2078-2079 (2009). https://doi.org:10.1093/bioinformatics/btp352

91 Ramírez, F., Dündar, F., Diehl, S., Grüning, B. A. & Manke, T. deepTools: a flexible platform for exploring deep-sequencing data. *Nucleic Acids Res* **42**, W187-191 (2014). https://doi.org:10.1093/nar/gku365

92 Bentsen, M. *et al.* ATAC-seq footprinting unravels kinetics of transcription factor binding during zygotic genome activation. *Nature Communications* **11**, 4267 (2020). https://doi.org:10.1038/s41467-020-18035-1

93 Fisher, R. A. On the Interpretation of χ² from Contingency Tables, and the Calculation of P. *Journal of the Royal Statistical Society* **85**, 87-94 (1922). https://doi.org:10.2307/2340521